Dissertation

Macro- and Microscopic Properties of Gradient Ultra High Strength Thermo-Mechanically Rolled Seamless Steel Tubes

Dipl.-Ing. Gerald WINTER

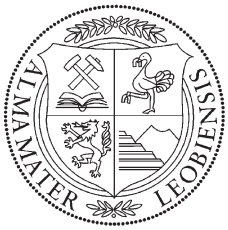

University of Leoben

Department Product Engineering

Chair of Metal Forming

July 2015

Schladnitzgraben 25
8700 Leoben
Austria

Affidavit

I declare in lieu of oath, that I wrote this thesis and performed the associated research myself, using only literature cited in this volume.

Leoben, July 2015

Acknowledgements

This work would not have been possible without the great support of supervisors, co-workers, colleagues and my family. In particular I would like to express my gratitude to the following persons:

Univ.-Prof. Dipl.-Ing. Dr.mont. Bruno Buchmayr, my first supervisor as well as to **Assoz. Prof. Dr. Jozef Keckes**, my second supervisor, for their guidance through the complex topic of material behaviour and characterization methods of seamless gradient steel tubes. I am grateful for their advices, support and the always open door.

voestalpine Tubulars GmbH & Co KG - CEO **Dipl.-Ing. Wolfgang Rainer** as well as R&D department manager **Dipl.-Ing. Dr.mont. Juergen Klarner** for the possibility to perform this work, the financial project support and the confidence in me to handle this huge project and the all-time support in any issue and requirement.

All involved colleagues and departments for their amazing TEAMWORK, cooperativeness, successful attended tube rolling sessions including pre- and post-processing as well as endless discussions and further to **Nina Breinhoelder**, **Albert Hornhofer** and **Manuel Oberer** as well as **Mario Zwansleitner** and **Gottfried Schrittwieser** for uncountable samples machining, testing and documentation.

Dr. Norbert Schell, **Dr. Peter Staron** and **Dr. Torben Fischer**, staff at high energy material beamline HEMS P07, PETRA III, DESY, Hamburg, for providing synchrotron source with ideal experimental conditions and for their support during the experiments and afterwards.

My wife **Doris** and son **Sebastian** for their love, support and all-time sympathetic sacrifice.

Abstract

*U*ltra *h*igh *s*trength *t*hermo-*m*echanical *r*olled *t*ubes (UHSTMRT) used as structural and design elements in various engineering applications are expected to withstand precedent service conditions including cyclic loading and extreme thermal as well as chemical loads. The further development of UHSTMRT can be based only on a detailed understanding of structure-property gradients across the tube wall and on employing those gradients to adjust the tube overall functional properties. The applied water cooling at the tube surface directly after the last production step results in the formation of complex microstructural, residual stress and phase gradients across the wall. In order to reveal complex structure-function-relationships, advanced multi-scale and multi-method investigations must be applied in order to understand how the cooling intensity influences the variation of the properties across the wall and then scales with macroscopic tube toughness, ultimate tensile strength and resistance to fatigue. In this thesis, advanced analytical techniques are used to investigate structural and mechanical property relationships in UHSTMRT produced under well-controlled thermal conditions by characterizing the overall properties of tubes as well as by analysing the local mechanical, microstructural and phase gradients.

Laboratory and synchrotron X-ray diffraction techniques are used to analyse two new weldable, low carbon alloying concepts fabricated using different *t*hermo-*m*echanical (TM) treatments. The overall macroscopic properties were determined by testing tubes as full wall sections specimens and secondly as micro-sized samples. The micro-sized samples for tension and impact testing are machined from individual tube regions across the wall. Complementary, residual stresses and the microstructure across the tube wall were characterized using X-ray diffraction, *M*oessbauer *s*pectroscopy (MS) and *t*ransmission *e*lectron *m*icroscopy (TEM) as well as light optical microscopy. Using this multi-method and multi-scale approach gave the possibility to determine a whole set of parameters like phases, grain morphology, dislocation densities, residual stress profiles, tensile strength, fracture strains as well as toughness and hardness profiles across the tube wall. Finally the data were correlated with the conditions applied during tube production in order to understand the formation of gradients as well as their influence on mechanical qualities. The process of the (surface) spray water cooling after the stretch reducing was modelled by finite element (FEM) software DEFORM^{HT}. In the model, experimental data were used to validate and improve the prediction quality for new steel grades.

Kurzfassung

Höchstfeste thermomechanisch gewalzte nahtlose Stahlrohre (UHSTMRT) werden als Struktur- und Designelemente in den unterschiedlichsten technischen Anwendungen eingesetzt und müssen den vorliegenden statischen, dynamischen, thermischen und chemischen Belastungen standhalten. Künftige Entwicklungen von UHSTMRT können nur auf Basis von Expertise über die Auswirkung der eingebrachten und sich über die Rohrwand veränderten Strukturgradienten, dessen Entstehung sowie deren gezielte Generierung im Produktionsprozess als auch die eingestellten Funktionseigenschaften des Rohres erfolgen. Die Beaufschlagung der Rohroberfläche mit Wasser unmittelbar nach dem letzten Umformaggregat zum Entziehen der Prozesswärme führt in Abhängigkeit der Intensität zur Ausbildung von komplexen Mikrostrukturen, Eigenspannungen und Phasengradienten. Um diese komplexen Struktur- und Funktionseigenschaften betrachten zu können, sind umfangreiche und präzise Untersuchungsmethoden auf mehreren Größen-Skalen erforderlich. Diese Untersuchungen dienen zur Erfassung des Einflusses der Kühlintensität und der resultierenden lokalen Eigenschaften wie Zähigkeit, Streckgrenze, Zugfestigkeit und Dauerfestigkeit des Rohres. In dieser Arbeit wurden hochauflösende und aufwendige Untersuchungsmethoden angewendet, um die makroskopischen Eigenschaften der gewalzten Rohre und der lokal vorliegenden Eigenschaften und deren Wechselwirkungen innerhalb der Gradienten zu ermitteln.

Labor- und hochenergetische Strahlungstechniken wie Synchrotron-Strahlung wurden zur Charakterisierung der Eigenschaften von thermomechanisch gewalzten Rohren aus zwei neu entwickelten schweißbaren Legierungskonzepten angewendet. Um die globalen und lokalen Eigenschaften der Rohre zu ermitteln, wurden Proben aus kompletten Rohrsegmenten sowie Kleinstproben angefertigt und geprüft. Die Kleinstproben zur Bestimmung der lokalen mechanischen Eigenschaften mittels Zug- und Kerbschlagversuch wurden aus bestimmten Lagen der Rohrwand gefertigt. Ergänzend zu den mechanischen Eigenschaften wurden unter Verwendung von Röntgenbeugung, Moessbauer Spektroskopie, Transmissionselektronenmikroskopie und Lichtmikroskopie auch die Eigenspannungen und die Mikrostruktur über die Rohrwand ermittelt. Durch den Einsatz dieser Multi-Methoden und Multi-Skalen Untersuchungen war es möglich einen umfangreichen Pool an Parametern zu generieren, bestehend aus den Phasen, Gefügemorphologien, Versetzungsdichten, Eigenspannungsprofile, Zugfestigkeiten, Streckgrenzen, Zähigkeit und Härteprofile in Abhängigkeit der Position entlang der Rohrwand. Nach dem Vorliegen der Untersuchungs-

daten wurden diese mit den Produktionsbedingungen und den Kühlgradienten zusammengeführt, um die Entstehung der Gradienten und deren Auswirkung auf die mechanischen Eigenschaften des Rohres zu bewerten. Der Rohrkühlprozess nach dem Streckreduzierwalzen wurde parallel zu den Untersuchungen mit der Finiten Elemente Software DEFORM^{HT} simuliert. Das Modell zur Berechnung neuer Legierungen wurde mit den ermittelten Untersuchungsergebnissen laufend validiert und optimiert.

Contents

Nomenclature

A0	initial cross section
A	effective cross section
ACR	accelerated cooling rate
ASTM	American society for testing and materials
AT	austenitization temperature
Bcc	body-centered cubic lattice
BST	bainite start temperature
CC	carbon content
CCT	continuous cooling transformation
CEW	carbon equivalent for weldability
CFD	computational fluid dynamics
cp	specific heat
EBSD	electron back scattering diffraction
Fcc	face-centered cubic lattice
FEM	finite elements method
F	compression force
FS	fracture strain
FST	ferrite start temperature
FT	fracture toughness
h0	initial heigth
HAADF	high angle annular dark field
HAZ	heat affected zone

h	effective heigth
IC	intermediate cooling
kf	flowstress
LEXT	laser scanning digital microscope
M3C	carbide type M3C e.g. cementite
MAG	metal active gas welding
MS	Moessbauer spectroscopy
MST	martensite start temperature
OD	tube outer diameter
PA	welding in flat position
PC	welding in horizontal position
PFM	pole figure measurement
phi	deformation degree
PST	perlite start temperature
QaT	quenched and tempered
REM	scanning electron microscopy
rho	density
RT	room temperature
SEM	scanning electron microscopy
TAC	total alloying content
TAD	dilatometer device from TA Instruments
TEM	transmission electron microscopy
theta	temperature increase
TH	test heat

TIG	tungsten inert gas welding
TM	thermo-mechanical
TMTS	thermo-mechanical treatment simulator
UHSTMRT	ultra high strength thermo-mechanical rolled tube
UTS	ultimate tensile strength
V	transformed volume
WT	tube wall thickness

1

Introduction

The increasing demand for production of light-weight, high-strength and high- performance tubes requires an optimization of intrinsic material properties [8] like UTS, FS and FT. Tube manufacturing [13, 55] includes a series of main-processes like billet heating, piercing, push-bench processing, intermediate-cooling, reheating, stretch reducing and (surface) spray water cooling. During production, the variety of applied thermo-mechanical treatments results in formation of complex residual stress fields across the tube wall which further correlate with a complex gradual steel microstructure induced by the [39, 67] cooling intensities. Tubes with high strength as well as high toughness produced at well-defined cooling rates are investigated in order to reveal complex production conditions-structure-function relationships [70].

For the characterization of gradient tube wall properties, advanced approaches with spatial resolution ranging from centimeter down to nanometer scale are used to determine overall and local properties like phases, grain sizes, residual stress state, texture, morphology and stacking fault energy as well as precipitate distribution. Specifically very unique non-destructive residual stress characterization in steel tubes at large penetration depths was performed by using high-energy synchrotron X - ray diffraction [20]. Synchrotron X - rays, with energies in the range of 50-300 keV, enabled fast experimental characterization of three-dimensional strain fields. Further residual stress fields across whole tube wall cross-sections are evaluated in order to analyse the influence of cooling rate intensity on the stress level as well as stress distributions in plastically deformed tubes.

An important aim of the thesis is to characterize the complex structure-function-relationship in tubes produced using two new alloying concepts. The advanced characterization approaches used for tube gradient examinations, listed in the sub-chapters and briefly introduced as well as discussed in appended publications.

1.1. Ultra high strength thermo-mechanically rolled tubes

Seamless steels tubes with fine grained microstructure induced mainly by intermediate phase transition during and spray water cooling after the rolling process yield excellent mechanical properties, especially high strength and toughness. Therefore (i) a state of the art tube rolling process, (ii) fundamentals of temperature controlled tube rolling and (iii) designed alloying concepts will be discussed. The main aims of the thesis are (i) to evaluate two novel alloying concepts and (ii) to analyze the influence of thermo-mechanical tube rolling, especially the role of cooling intensity, on the mechanical performance.

1.1.1. State of the art tube rolling

Seamless steel tubes are produced in a few main-processes, chronological represented in figure 1.1 and table 1.1.

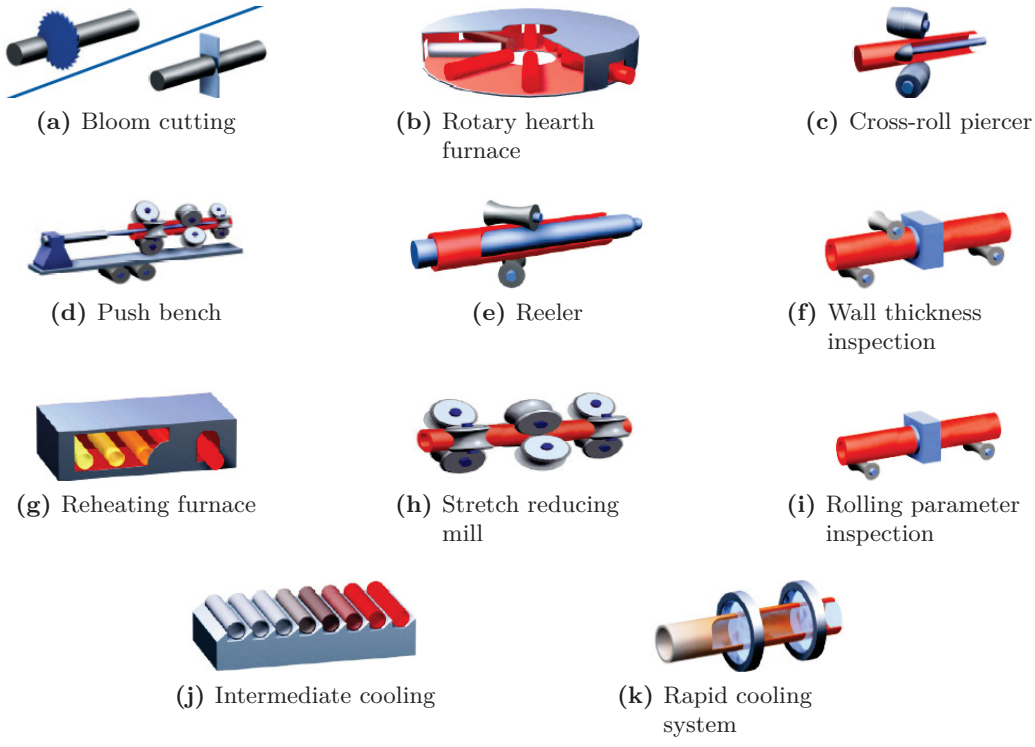

(a) Bloom cutting

(b) Rotary hearth furnace

(c) Cross-roll piercer

(d) Push bench

(e) Reeler

(f) Wall thickness inspection

(g) Reheating furnace

(h) Stretch reducing mill

(i) Rolling parameter inspection

(j) Intermediate cooling

(k) Rapid cooling system

Figure 1.1.: Seamless tube production layout, (a) to (i) main processing steps in chronological order, (j) and (k) optional TM processing steps.

Main Processing Step	Description according to figure 1.1
(a) Bloom cutting	Continuous casted blooms with a diameter of 230 mm and a length of about 12 m, depending on the bloom weight, are used as raw material. Blooms are sawed in case of alloyed, and sheared in case of unalloyed chemical composition to billets. Required billet-processing-weight was pre-calculated from desired final tube geometry as well as inspection requirements.
(b) Rotary hearth furnace	According processing-weight-billets are heated in the rotary hearth furnace to a forming temperature of about 1300 °C depending on the alloying concept.
(c) Cross-roll piercer	A piercing mill [54] is used to subject solid round billets to rolling process. Heated billets are milled against an inner plug, referred to Mannesmann principle [55], and so shaped to hollows with a specific wall thickness and diameter.
(d) Push bench	The pierced hollow is attached to the end of a mandrel bar and fixed by a crimping press. The received material-tool hybrid is lifted to the push bench and pushed through non-driven stands of three-roll cages. The cross section decreases from stand to stand [5] and elongates the shell [17] on the tool to a maximum length of 22.9 m.
(e) Reeler	After elongation the mandrel bars are released by a reeler.
(f) Wall thickness inspection	After tool rejection the shell geometry is inspected along the whole length and transmitted to the online control system for setting further forming operation parameters.
(j) *Optional TM-Stage I (table 1.2)*	
(g) Reheating furnace	In the reheating furnace, tube shells are heated to required temperature, depending on the amount of total alloying content from 860 to 1050°C for stretch reducing.
(h) Stretch reducing mill	Reheated and descaled shells are formed in the stretch reducing mill with maximum 28 driven roller-stands to desired final diameter and wall thickness. By the transmitted input geometry [6] data the speed level of the roller stand is regulated to achieve homogeneous tube geometry.
(k) *Optional TM-Stage II (table 1.2)*	
(i) Rolling parameter inspection	Final tube inspection along the entire length reflects the quality of applied settings. The finished rolled tubes are cooled down subsequently at free air on a rake type cooling bed.

Table 1.1.: Main-process steps of seamless tube rolling.

Steps (j) and (k) (fig. 1.1) are optional processing steps and used to optimize the tube's structural as well as mechanical response, further denoted as TM-Stage I and II, table 1.2 describes the purpose.

Optional processing step	**Description according to figure 1.1**
(j) Optional TM-Stage I Intermediate cooling	To adjust the grain refinement as a result of the phase transition from austenitic γ to ferritic α phase, the cooling time of the elongated shell must be controlled-temperature dissipated [51]. Grain refinement [14] is essential for the strengthening mechanism, because it simultaneously enhances both toughness and strength. Fine grained [63] tubes with special designed micro-alloying concepts are strengthened primarily by grain refinement at intermediate cooling stage. Due to this fact, tubes have a great potential to avoid additional alloying elements owing to lower required carbon contents and contribute to an increase of weldability.
(k) Optional TM-Stage *II* Rapid cooling system	In this stage, also known as accelerated cooling, [39] the hot forming temperatures are dissipated from the final tubes by (surface) water spraying. The cooling interval from 1000 °C down to maximum 200 °C can be achieved. By applied water cooling, both improved mechanical properties and better surface qualities are achievable. Additionally, accelerated cooling also supports α -grain refinement and improves tube strength as well as toughness. With a selective temperature loss during spray water cooling, microstructural gradients can be adjusted. This treatment, denoted as cross-section layer design, formed by accelerated cooling [19], ensures a tube wall gradient with martensite followed by bainite and ferrite/perlite layers. Furthermore with this advanced treatment option, it is possible to design tubes with extraordinary good mechanical properties compared to single phase tubes.

Table 1.2.: Optional process steps of seamless tube rolling. $\Longrightarrow$ TM Stage I and II.

1.1.2. Thermomechanically tube rolling

Thermo-mechanical processing is designed [67] to achieve improved mechanical properties like ultimate tensile stress, fracture strain and toughness by controlling hot rolling deformation process conditions. Shape production of tubes is the original task of this process, but nowadays also required material properties can be adjusted by demanded process conditions. The aim of thermo-mechanically rolling is to improve functional properties of high strength seamless steel tubes. The demands [23] are focused on adaptation of novel alloying concepts with micro alloying elements for precipitation hardening mechanisms, as well as the accelerated water quenching to define a gradient microstructure. To produce thermo-mechanically rolled seamless steel tubes, the applied temperatures during the whole manufacturing process require to be controlled. The TM-processing [43] is divided into two stages, (i) phase transition from austenitic γ to ferritic α phase for grain refinement [62] before the tube enters the reheating furnace and (ii) fixing the adjusted microstructure directly after stretch reducing.

Due to the high material temperatures, the billet piercing results in a recrystallized γ- grained microstructure. The grain size decreases rapidly with an increase of the amount of rolling reduction to its limit value according to the alloying concept. Progressive refinement [77] of austenite can be achieved through dynamic and static recrystallization during large strain deformation at temperatures above the recrystallization temperature [63].

The mandrel bar reduces the shell's temperature to a value under the recrystallization temperature range. In consequence of this non-recrystallizing deformation, both the tube and grains experience an elongation. The degree of deformation substantially increases the α nucleation rate and further the base for grain refinement at the intermediate transition step. In general [65] phase transitions for low carbon steels, under the critical cooling rate for martensitic formation, induce that austenitic $\gamma-$ grains are divided into several ferritic and perlitic $\alpha-$ grains. The 24 orientation relations between γ- and α-phases, described by equation 1.1, enable some adjacent, polygonal, similar orientated $\alpha-$nucleates at the $\gamma-$grain boundaries to coalescent into one grain [21].

$$< 111 >_{\gamma} \,//\, < 011 >_{\alpha}, \left[\bar{1}01\right]_{\gamma} \,//\, \left[\bar{1}1\bar{1}\right]_{\alpha} \tag{1.1}$$

Based on the optionally added process stage I, the intermediate cooling supports this grain refinement transition. Stretch reducing for reheated, fine grained tube

shells, at 930°C effects microstructure with elongated and deformed grains [27]. Due to perfect processing conditions it is possible to adjust latent dynamic recrystallisation to eliminate texture and grain deformations. Bcc ferrite [63] has a high stacking fault energy which results in rapid recovery and insufficient accumulation [25] of stored deformation energy to promote dynamic recrystallization [14].

The last stage of TM processing to achieve macroscopic ultra high strength and excellent toughness properties is the (surface) spray water cooling (fig. 1.2) which secures the extreme fine grain microstructure. The deformation by stretch reducing in the two phase region in combination with the latent recrystallized (α+γ) microstructure results (i) in γ work-hardened and (ii) in deformation of α form substructures with high dislocation densities. The deformation schedules (strain/strain rate/temperature) predefine the balance [9] between (i) dynamic transformation from austenite into ferrite and (ii) the dynamic recovery as well as (iii) dynamic recrystallization of ferrite effected through control of the processing parameters and cooling [53]. Low carbon steels have a relatively small inter-critical regime and recrystallization of deformed ferrite [38], which can proceed rapidly but is terminated upon rapid cooling. Very fine [33] ferrite grain size could be produced from a steel having a large prior austenite grain size. Intra-granular nucleation of ferrite contributes to additional grain refinement [58]. This can be observed when a dynamic strain-induced transformation occurs [15], and is encouraged by large austenite grain sizes and accelerated cooling, both suppresses the formation of grain boundary per-eutectoid ferrite. The heat transfer coefficient of spray water cooling and the thickness of the tube cross-section primarily influence the microstructural layer design. In the case of processed tubes with large wall thickness, the applied cooling results in martensitic followed by bainitic and ferritic/perlitic phase-layers.

1.1.3. UHSTMRT test-heats

The primarily formulated development target at the beginning of the thesis was to achieve a weldable ultra high strength steel alloying concept with an UTS of 1200 MPa and fracture strain of 15 %. In respect to the weldability of new UHSTMRT-grades, TH's were limited to TAC of 6 %, CC to 0.9 [-] and CEW to 0.45 [-]. The CC calculated after equation 1.2 according to the standard of the international institute of welding [1] as well as CEW calculated after equation 1.3 according to the technical rule of SEW 088 [71].

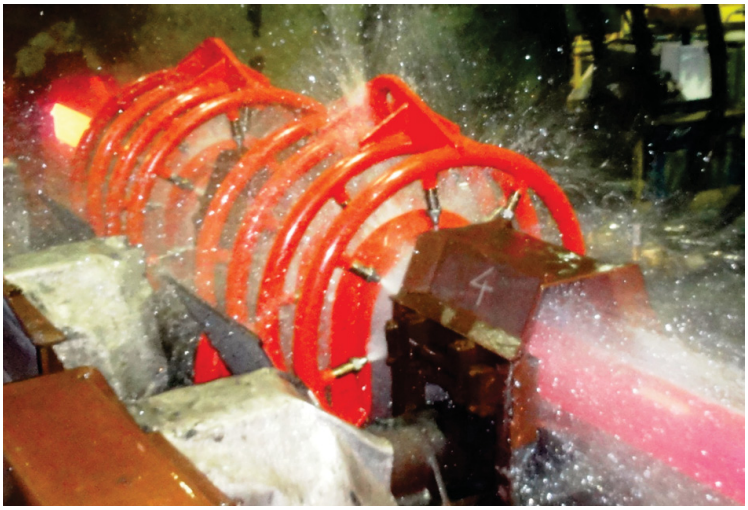

Figure 1.2.: Cooling devices for accelerated tube surface cooling.

$$CC = C + \frac{Mn}{6} + \frac{(Cr + Mo + V)}{5} + \frac{(Cu + Ni)}{15} \tag{1.2}$$

$$CEW = C + \frac{(Mn + Mo)}{10} + \frac{(Cr + Cu)}{20} + \frac{Ni}{40} \tag{1.3}$$

Developed alloying concepts are shown in table 1.3 and further denoted as TH02 and TH04. Table 1.4 shows the calculated values for CEW, CC and the TAC.

	C	**Mn**	**P**	**S**	**Cr**	**Ni**	**Ti**	**Cu**	**V**	**N**
TH 02	0.20	1.20	0.01	0.005	1.00	1.00	0.20	0.015	0.00	0.04
TH 04	0.20	1.20	0.01	0.005	1.50	1.00	0.20	0.020	0.10	0.01

Table 1.3.: Alloying concept for UHSTMRT TH 02 and 04 (contents in weight %).

	TAC	**CC**	**CEW**
TH 02	**4.78**	**0.73**	**0.42**
TH 04	**5.41**	**0.85**	**0.45**
△	**0.63**	**0.12**	**0.03**

Table 1.4.: (i) total alloying content, (ii) carbon content and (iii) carbon equivalent for UHSTMRT TH02 and TH04.

TH02 and TH04 differ by increased chromium and vanadium as well as decreased nitrogen content. The copper content varies due to processed scrap at steel making. Additional micro-alloying elements are used to improve work hardening mechanism and shift areas of phase-transition to temperature ranges optimized for applied thermo-mechanical [48, 49] tube rolling process conditions. An overview of the principle of operation at selected alloying elements and their major purposes are illustrated in table 1.5 after [46, 24].

Element	Purpose
Vanadium	Leads to precipitation strengthening VN precipitates predominant ferrite strengtheners
Nitrogen	TiN restricts austenite grain growth and improves toughness
Boron	Improves quench hardenability with Nb and Mo Promotes forming lower bainite and lath martensite
Molybdenum	Improves hardenability and strength Promotes formation of lower bainite Suppresses austenite recrystallisation and grain growth
Niobium	Promotes refined ferrite Promotes large volume fraction of acicular ferrite Retards recrystallization and inhibit austenite grain growth Reduce temperature range of recrystallization
Nickel	Increases bainitic fraction Increases low temperature toughness
Chromium	Improves strength and quench hardenability Lowers carbon activity in ferrite
Manganese	Promotes fine-grained lower bainite microstructure Delays austenite transformation during accelerated cooling

Table 1.5.: Major purpose of selected alloying elements, focused on grain refinement and phase transition [46].

The quenched and tempered Steel grade S890 QL_1, according to the technical rule [72], represents the reference for further validation of UHSTMRT performance. Actual standardization limit for high strength, low alloyed seamless steel tubes, mirrored by grade S890 QL_1exhibit minimum specifications for yield stress $Rp_{0.2} = 890$ MPa, tensile stress Rm = 960 MPa and elongation A = 14 % in respect to tube-wall thicknesses up to 12.0 mm.

1.1.4. UHSTMRT specimen declaration

In table 1.6 an overview of further handled specimens displayed in respect to material grade, dimension, and process conditions and are visualized in figure 1.3.

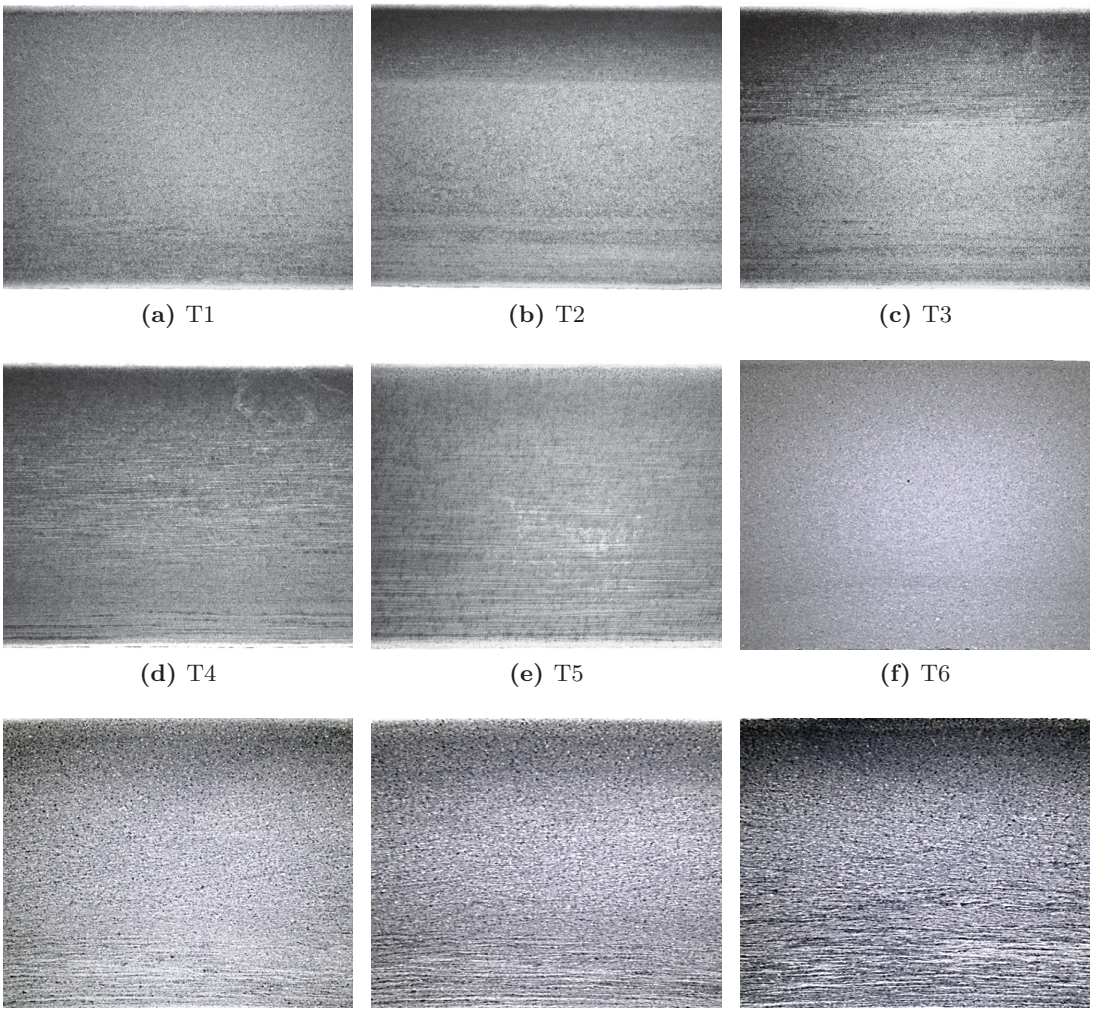

(a) T1 **(b)** T2 **(c)** T3

(d) T4 **(e)** T5 **(f)** T6

(g) T7 **(h)** T8 **(i)** T9

Figure 1.3.: Microstructure of 10 mm tube cross-section for (a) T1 to (i) T9 whereby upside is outer tube surface.

Specimen	Grade	OD [mm]	WT [mm]	IC	ACR [°C/sec]	QaT
T 1	TH 02	168.3	10.0	☑	☒	☒
T 2	TH 02	168.3	10.0	☑	15	☒
T 3	TH 02	168.3	10.0	☑	25	☒
T 4	TH 02	168.3	10.0	☑	30	☒
T 5	S890 QL_1	168.3	10.0	☒	☒	☑
T 6	TH 04	168.3	10.0	☑	☒	☒
T 7	TH 04	168.3	10.0	☑	15	☒
T 8	TH 04	168.3	10.0	☑	25	☒
T 9	TH 04	168.3	10.0	☑	30	☒

Table 1.6.: Specimen declaration, ☑applied, ☒ not applied.

1.2. Multi-scale mechanical property characterisation

The austenite [36] phase in low carbon steels can transform to bainite with various microstructures such as granular bainite, acicular ferrite and bainitic ferrite as a result of continuous cooling process. The characterization of the local and overall mechanical properties in respect to the applied ACR on the tube surface is discussed further [37, 77, 45, 41, 61, 21, 63].

1.2.1. Charpy impact testing

The impact characterization was undertaken with Charpy V - notch tests of TH02 and TH04 in the temperature range of -80 °C to room temperature, as well as (fig. 1.7) on 7.0 mm x 10 mm x 55 mm and 3 mm x 4 mm x 27 mm micro sized specimens, illustrated in fig. 1.4. The aim of this study is to provide a wide experimental database and microstructural observations to supply, calibrate and validate the FEM. Effects of impact velocity on ductile–brittle transition curve and the fracture surfaces are presented and discussed [66, 56, 68, 50]. An overview of fractured macro sized specimens for T1 to T9 at RT are shown in figs. 1.5 and 1.6, the according values are listed in table 1.7 and the description of interpretation is documented in appendix E.

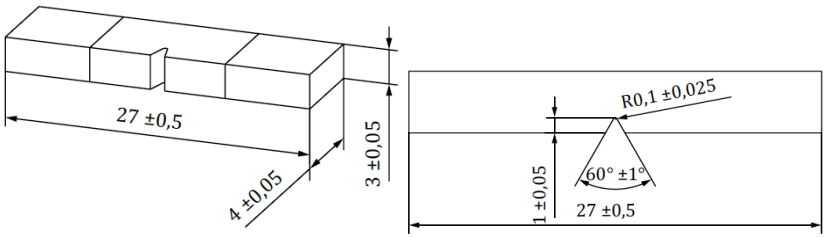

Figure 1.4.: Charpy V-notched micro sized specimen.

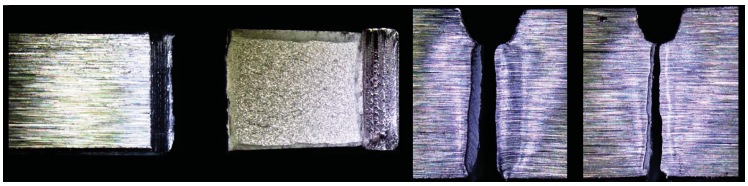

(a) T1

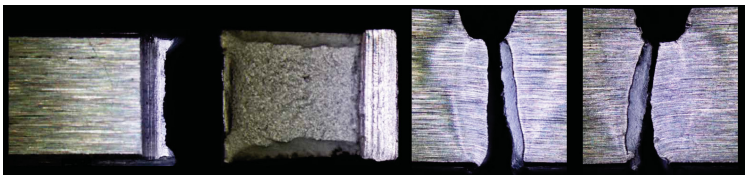

(b) T2

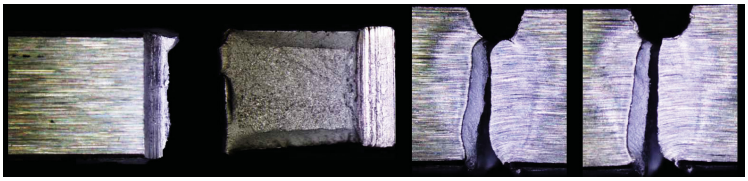

(c) T3

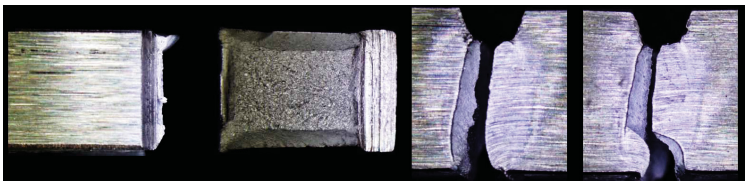

(d) T4

Figure 1.5.: Macro Charpy impact testing, fractured V-notched specimen T1 to T4 at RT.

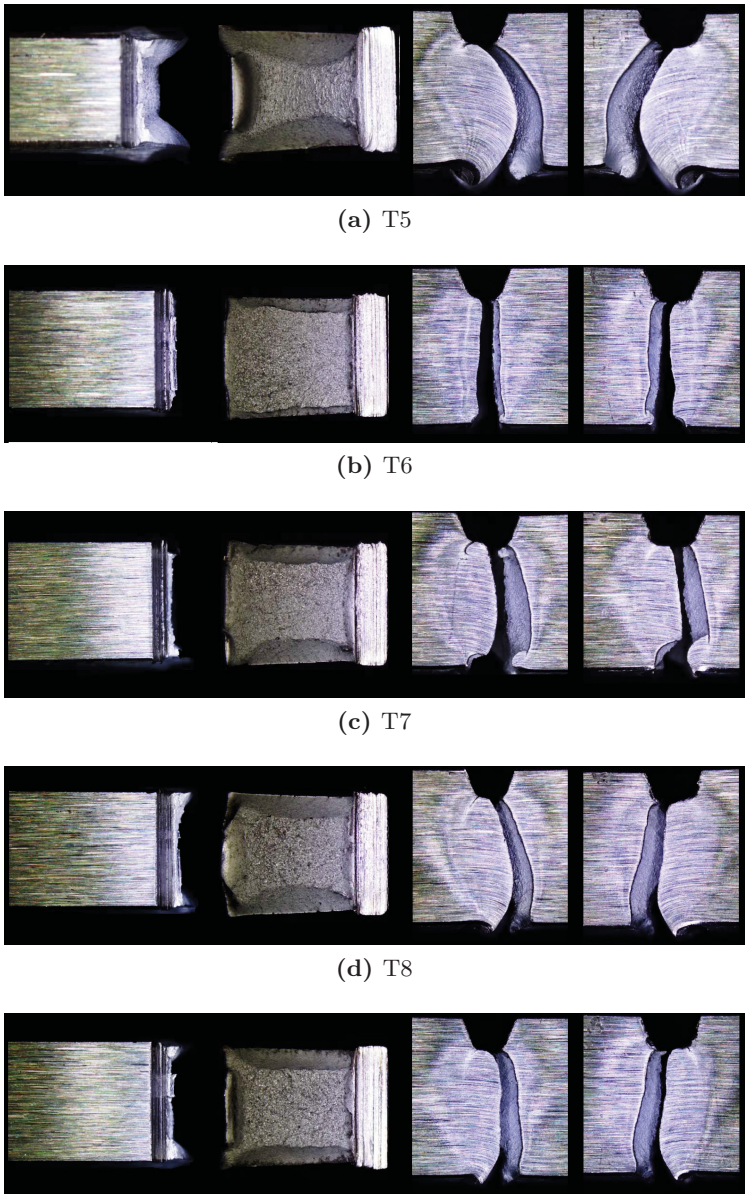

(a) T5

(b) T6

(c) T7

(d) T8

(e) T9

Figure 1.6.: Macro Charpy impact testing, fractured V-notched specimen T5 to T9 at RT.

T1	T2	T3	T4	T5	T6	T7	T8	T9
35.8	51.7	57.9	63.6	61.3	35.7	56.9	58.7	64.3

Table 1.7.: Absorbed energy in Joule documented from macro Charpy V-notched specimens at RT for T1 to T9.

The micro sized samples was tested with a PW 5 Otto Wolpert - Werke 50 Joule pendulum impact testing machine assembled with a 15 Joule hammer. The macro sized specimens was test on a Zwick RKP 450 Z pendulum impact testing machine.

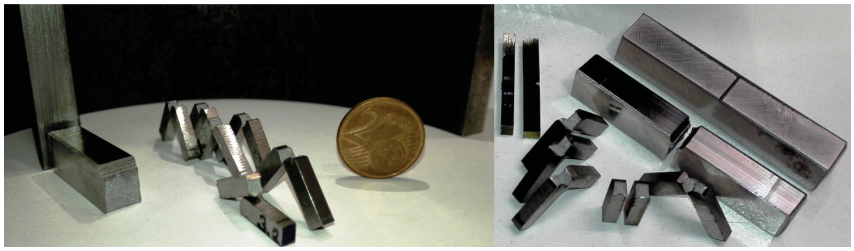

Figure 1.7.: Macro and micro Charpy impact testing specimen overview.

The investigated position resolved (apppendix E) values are listed in table 1.8 as well as an overview of fractured micro sized specimens for T6 to T9 at RT are shown in figs. 1.8 and 1.9 and the description of interpretation is documented in appendix E.

Sample position	T6	T7	T8	T9
1	3.8	4.9	5.1	5.8
2	3.1	5.3	5.5	5.5
3	2.9	5.4	5.2	5.9
4	3.5	4.9	5.1	5.2
5	4.0	5.1	5.6	5.5
6	5.4	5.4	5.6	5.8
7	4.5	5.9	5.3	5.8
Average	**3.9**	**5.3**	**5.3**	**5.6**

Table 1.8.: Absorbed energy in Joule documented from micro Charpy V-notched specimens at RT for T6 to T9.

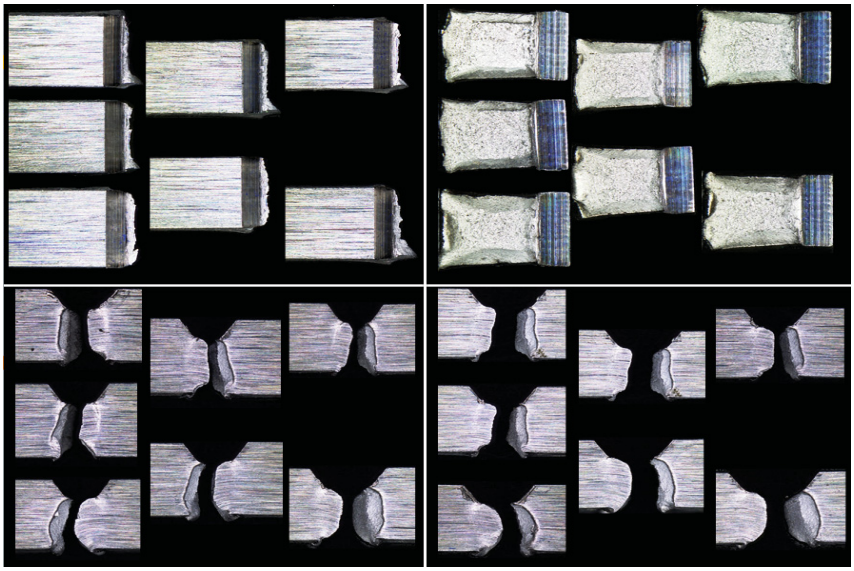

(a) T6

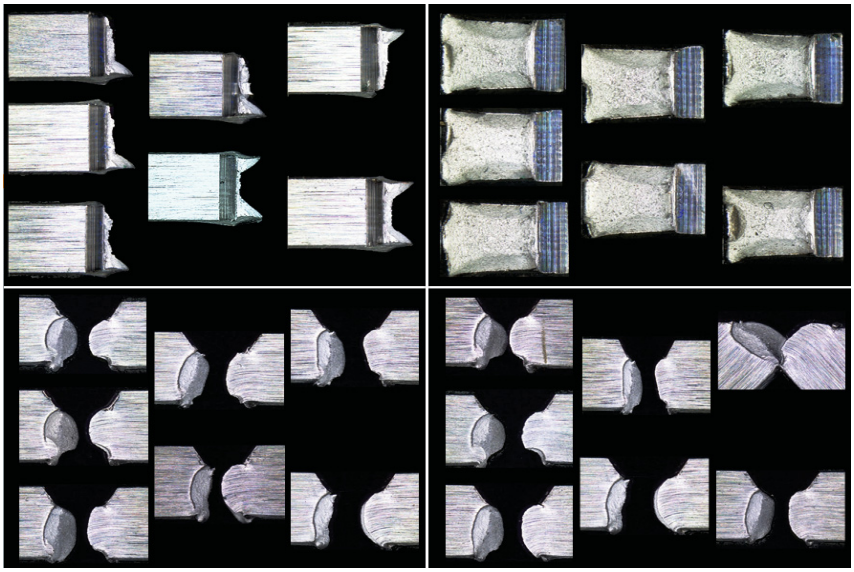

(b) T7

Figure 1.8.: Micro Charpy impact testing, fractured V-notched specimen (a) T6 to (b) T7 at RT.

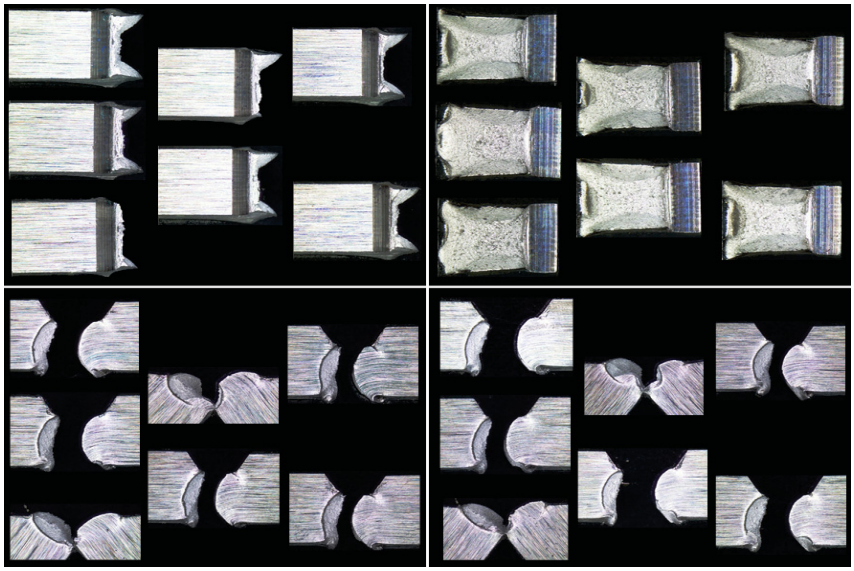

(a) T8

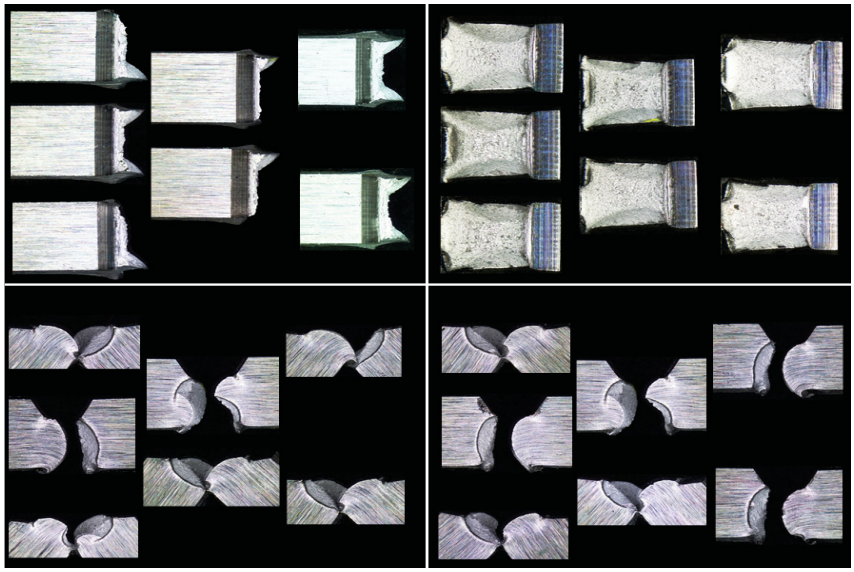

(b) T9

Figure 1.9.: Micro Charpy impact testing, fractured V-notched specimen (a) T8 to (b) T9 at RT.

1.2.2. Tension testing

Strained-controlled macro tensile tests on samples (fig. 1.11) with length of 320.0 mm, width of 25.0 mm and thickness of 10.0 mm, machined from tube wall sections were performed using ZWICK material testing machine BPC - F1200HN.F11. Micro

tensile tests on samples (fig. 1.10) with length of 22.0 mm, width of 1.0 mm and thickness of 1.0 mm, machined from different positions across tube wall were performed by using Kammrath & Weiss system equipped with 5 kN load sensor in strain-controlled mode [7, 47].

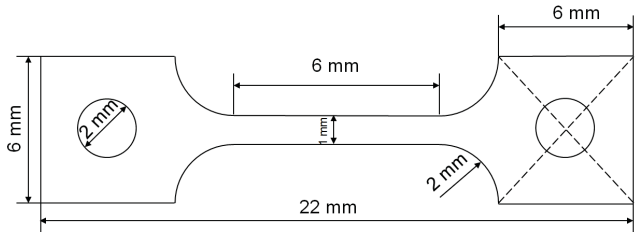

Figure 1.10.: Micro tension specimen geometry.

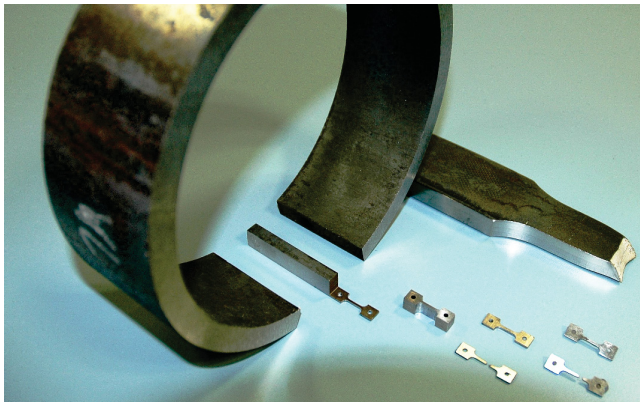

Figure 1.11.: Macro and micro tension specimen overview.

The fractured macro sized specimens for T1 to T9 are shown in fig. 1.12, the according values are listed in table 1.9, the stress strain diagrams are visualized in fig. 1.13 and the description of interpretation is documented in appendix D.

The fractured micro sized specimens for T1 to T9 are shown in fig. 1.14, the stress strain diagrams are visualized in fig. 1.15 and the description of interpretation is documented in appendix D.

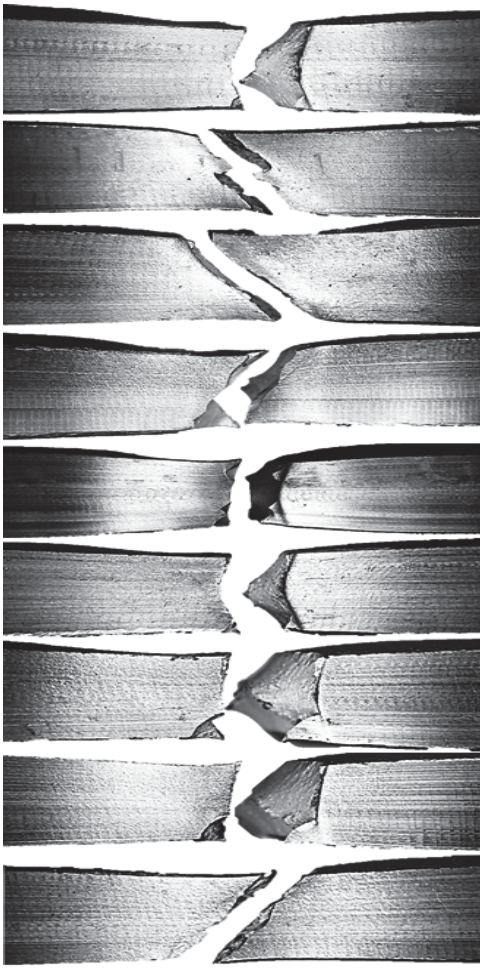

Figure 1.12.: Macro tension testing - fracture surfaces for tube T1 to T9.

	$\mathbf{Rp_{0.2}}$ **[MPa]**	**Rm [MPa]**	**A [%]**
T1	767.0	1220.2	13.5
T2	805.9	1236.7	14.7
T3	865.3	1231.0	13.6
T4	914.1	1231.4	12.4
T5	969.0	1018.8	12.6
T6	765.3	1241.4	12.4
T7	849.0	1265.8	12.0
T8	911.9	1275.2	13.1
T9	984.2	1302.9	12.2

Table 1.9.: Macro tension testing for T1 to T9.

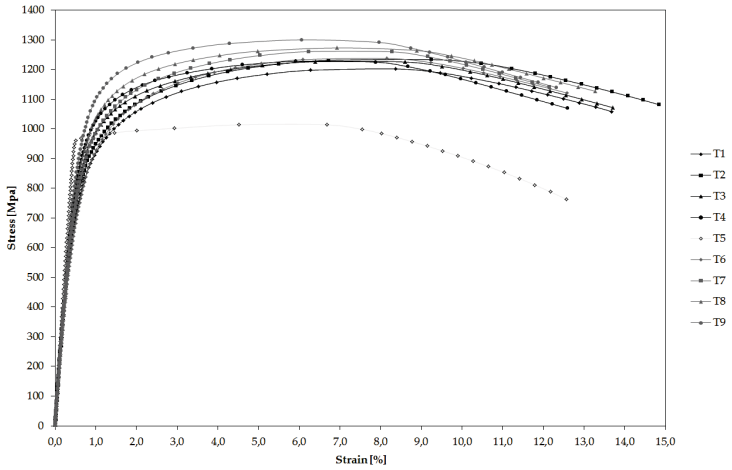

Figure 1.13.: Macro tension testing - stress strain diagram for tube T1 to T9.

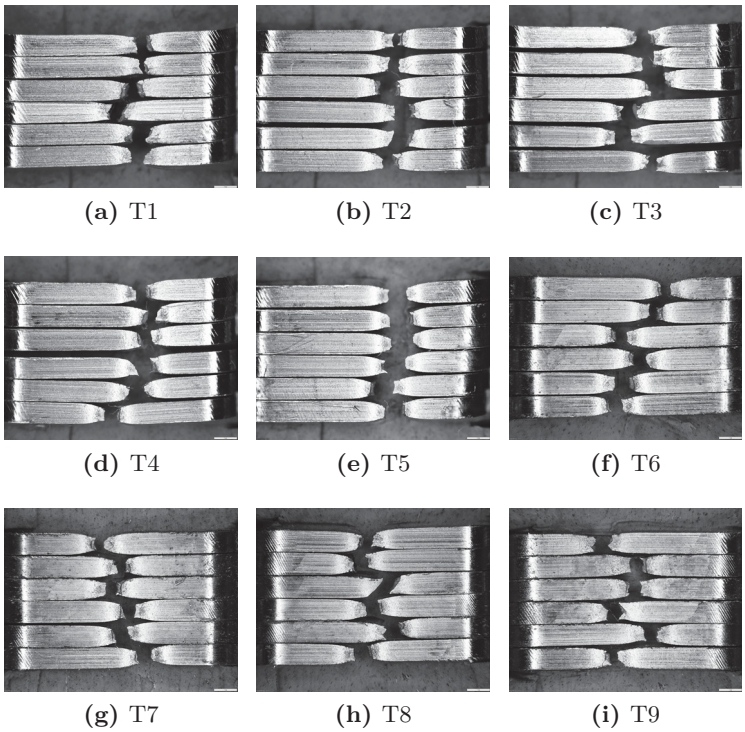

(a) T1 **(b)** T2 **(c)** T3

(d) T4 **(e)** T5 **(f)** T6

(g) T7 **(h)** T8 **(i)** T9

Figure 1.14.: Fracture surfaces of (a) T1 to (i) T9 whereby upside is outer tube surface.

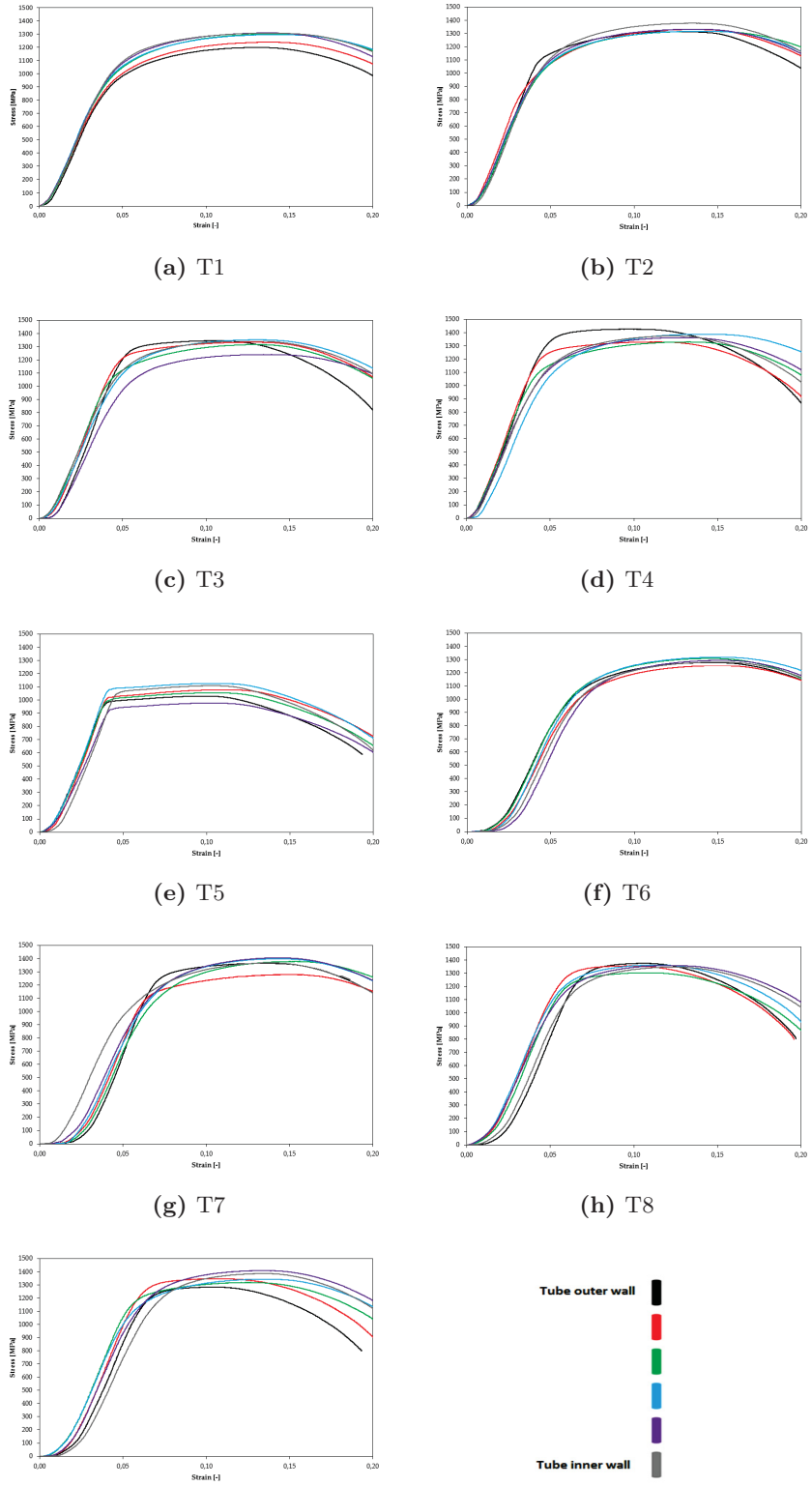

(a) T1 **(b)** T2

(c) T3 **(d)** T4

(e) T5 **(f)** T6

(g) T7 **(h)** T8

(i) T9 **(j)** Position scale

Figure 1.15.: Stress strain diagram of (a) T1 to (i) T9, (j) colour position scale.

1.2.3. Hardness testing

Vickers hardness HV 0.5 across the tube wall was determined by using Buehler Micromet 5104 system [29, 57]. The results of the measurements are listed in table 1.10, the diagram in fig. 1.16 shows the linear fitted HV 0.5 hardness of the tubes T1 to T9 and the description of interpretation is documented in appendix D.

	T1	**T2**	**T3**	**T4**	**T5**	**T6**	**T7**	**T8**	**T9**
0.5	405	411	431	421	322	397	431	406	437
1.0	398	412	427	427	348	400	425	421	440
1.5	386	405	416	425	364	404	440	439	447
2.0	402	396	411	424	363	415	425	431	433
2.5	396	389	405	440	366	396	428	433	440
3.0	390	388	405	422	368	412	442	431	447
3.5	388	386	412	431	379	425	421	445	431
4.0	400	404	412	443	355	415	437	419	428
4.5	402	393	416	413	361	413	419	422	421
5.0	390	396	405	433	366	422	425	412	428
5.5	413	402	421	422	364	425	411	421	433
6.0	384	400	428	427	361	421	411	418	428
6.5	393	386	425	416	363	436	425	424	436
7.0	416	415	408	416	367	422	428	425	445
7.5	396	409	418	433	364	418	427	415	434
8.0	405	406	415	443	384	428	427	450	440
8.5	402	425	416	434	354	425	439	456	456
9.0	409	392	431	439	361	409	430	451	455
9.5	400	406	412	440	369	409	443	451	451

Table 1.10.: Hardness measurement HV 0.5 for T1 to T9, position 0 is inner- and 10 is outer tube surface.

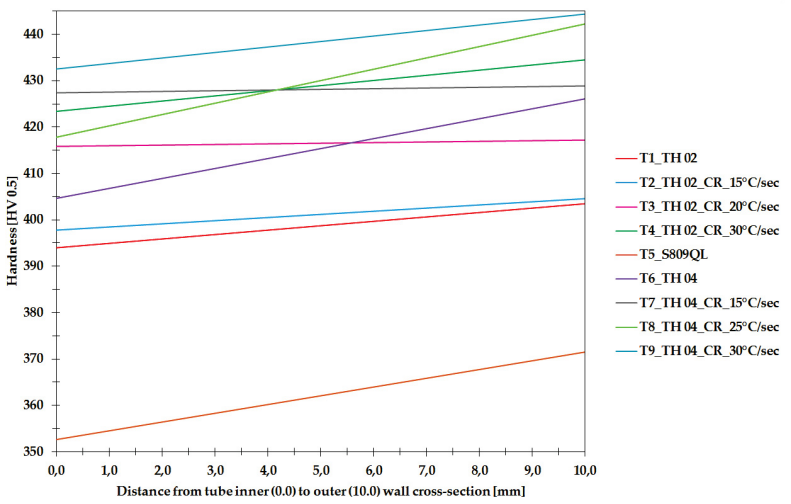

Figure 1.16.: Tube cross-section hardness measurements for T1 to T9.

1.3. X - ray Diffraction Analysis of Seamless Steel Tubes

X - rays discovered in 1895 by Wilhelm C. Roentgen and X - ray diffraction introduced by Max von Laue as well as by William Lawrence and William Henry Braggs in 1912 are currently routinely used in physics, materials science and chemistry to characterize properties of crystalline materials [11]. The approach is based on constructive interference of X - rays with the wavelength of about 1 Ångstroem which interact with electrons in material and are scattered in all directions. Since in a crystal lattice, distances between regularly distributed atoms are in the same range as the X - ray wavelength λ, diffraction maxima can be observed at Bragg's angles θ according the Bragg's law [10]:

$$2b\ sin\theta = n\lambda \tag{1.4}$$

where b is the distance between planes of atoms (fig. 1.17).

Diffraction experiment can be described by the vectors of primary and diffracted X - ray beams $\bar{k_0}$ and $\bar{k_1}$ which are used to define the diffraction vector $\bar{Q}$ as shown in fig. 1.18 [22].

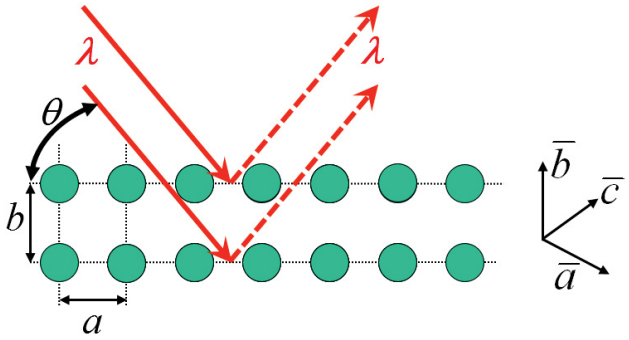

Figure 1.17.: A schematic description of the Bragg's law. X - rays with the wavelength λ interact elastically with regularly distributed atoms and constructive interference can be observed at an angle θ. The vectors $\bar{a}$, $\bar{b}$ and $\bar{c}$, represent the unit cell vectors with the length a, b and c, respectively.

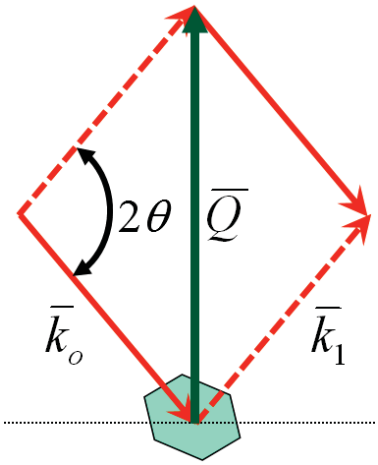

Figure 1.18.: Vectors of primary and secondary beams $\bar{k_0}$ and $\bar{k_1}$with lengths of $\frac{2\pi}{\lambda}$ can be used to construct diffraction vector $\bar{Q}$ with the length of $\frac{4\pi sin\theta}{\lambda}$which represents the property of the diffraction experiment.

For the crystal lattice, one can define a reciprocal lattice (fig. 1.19) using the translation vectors $\bar{a}^*$, $\bar{b}^*$and $\bar{c}^*$ as follows [69]:

$$\bar{a}^* = 2\pi \frac{\bar{b}^* \times \bar{c}^*}{\bar{a}^* \cdot (\bar{b}^* \times \bar{c}^*)} \tag{1.5}$$

$$\bar{b}^* = 2\pi \frac{\bar{c}^* \times \bar{a}^*}{\bar{a}^* \cdot (\bar{b}^* \times \bar{c}^*)} \tag{1.6}$$

$$\bar{c}^* = 2\pi \frac{\bar{a}^* \times \bar{b}^*}{\bar{a}^* \cdot (\bar{b}^* \times \bar{c}^*)} \tag{1.7}$$

The vectors $\bar{a}^*$, $\bar{b}^*$and $\bar{c}^*$ are used to construct the reciprocal space vector

$$\bar{H}_{hkl} = h\bar{a}^* + k\bar{b}^* + l\bar{c}^* \tag{1.8}$$

where hkl represent Miller indices of crystallographic plane. The $\bar{H_{hkl}}$ length is inversely proportional to the lattice spacing of (hkl) crystallographic plane and the vector is normal on the plane.

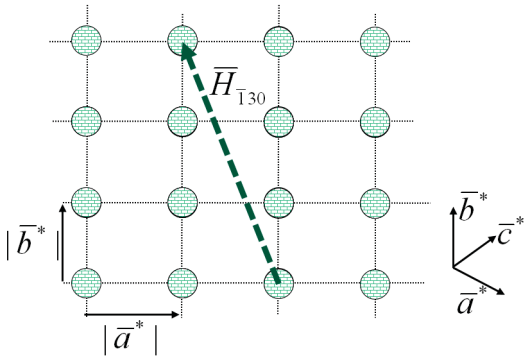

Figure 1.19.: The reciprocal lattice is defined by vectors $\bar{a}^*$, $\bar{b}^*$and $\bar{c}^*$. Length of the unit cell vectors a, b and c are inversely proportional to the length of the reciprocal vectors a^*, $b^*$and c^*, respectively. $\bar{H}_{hkl} = h\bar{a}^* + k\bar{b}^* + l\bar{c}^*$ represents the reciprocal lattice vector and hkl are Miller indices of crystallographic plane.

In a diffraction experiment, a constructive interference will be recorded by a detector only for the case [69]

$$\bar{H}_{hkl} = \bar{Q} \tag{1.9}$$

This means that not only the Bragg's angle hast be adjusted to the lattice spacing b (cf. fig. 1.17), but also the normal on the crystallographic plane (hkl) represented by the vector $\bar{H}_{hkl}$ must be parallel to the diffraction vector $\bar{Q}$. This specific feature of the X - ray diffraction experiment allows for direction-dependent characterization of material properties, in contrast to X - ray fluorescence, Raman and other spectroscopy techniques.

In the case of powder diffraction experiment performed using monochromatic X - ray beam (fig. 1.20), the diffraction results in the formation of Debye-Scherrer ring on the detector. Azimuthal and radial distributions of the intensity, $I(\delta)$ and $I(\theta)$, allow to evaluate phase, crystallographic texture, crystallite size and residual stresses in the sample [28].

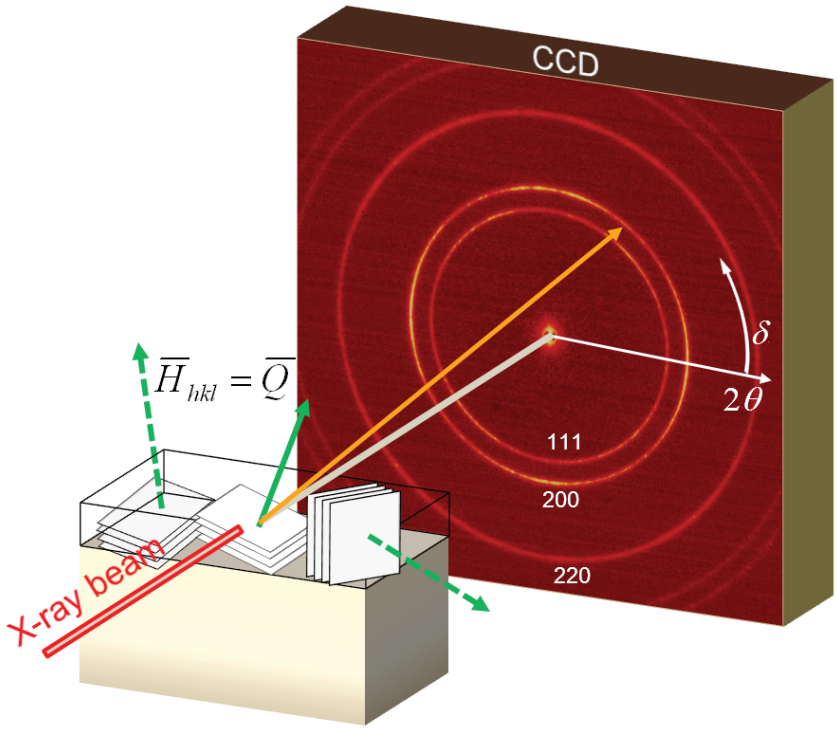

Figure 1.20.: A schematic set-up of a powder diffraction experiment. Diffraction of the X - ray beam results in the formation of hkl Debye-Scherrer rings on a two dimensional detector (CCD). During one exposure, crystallographic planes with various orientations of reciprocal space vectors $\bar{H}_{hkl}$ contribute to the diffraction along the rings at specific δ angles [28].

1.3.1. Laboratory XRD Analysis

Seamless steel tubes analyzed in this work were characterized using laboratory 5-axis X - ray diffractometer SmartLab from Rigaku Co. (Japan) in reflection geometry at the Department of Materials Physics of University of Leoben. The device is equipped with Cu-Kα radiation, a parabolic multilayer mirror in the primary beam and a secondary graphite monochromator (fig. 1.20).

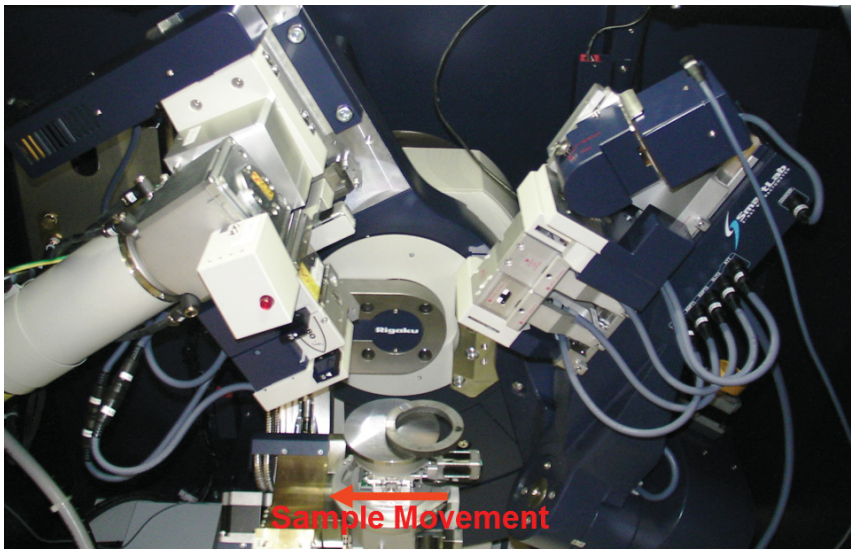

Figure 1.21.: An optical image of a position resolved XRD experiment on a cross-section of a steel tube (a steel ring in the goniometer centre) performed using Rigaku SmartLab system. During the experiment, diffraction data are collected as a function of Bragg's angle for different sample positions. The sample is moved along the arrow with a step of 0.8 mm.

For the position-resolved analysis, a line beam profile with a size of 0.8 x 5 mm^2 was usually used whereby the tubes were scanned across the tube wall applying a sample movement step of 0.8 mm. In this way it was possible to characterize structural properties of the samples across the wall cross-section and analyze the influence of water spray cooling on gradients of microstructure, phases, residual stresses and crystallographic texture. In fig. 1.21, representative XRD data document the variation of intensity and phases across the cross-section of an intensively cooled tube. In fig. 1.23 the obtained results of the XRD investigations for the tubes T1 to T4 are illustrated and the description of interpretation is documented in appendix E.

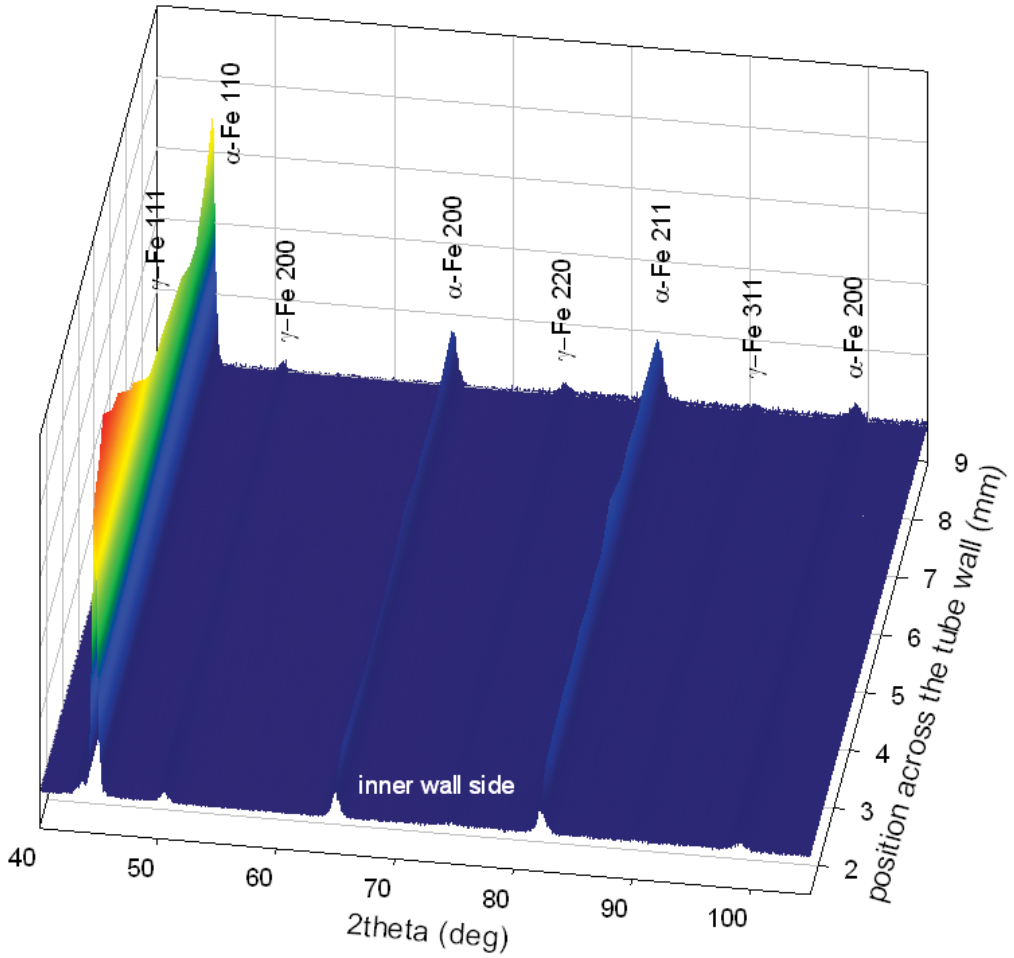

(a)

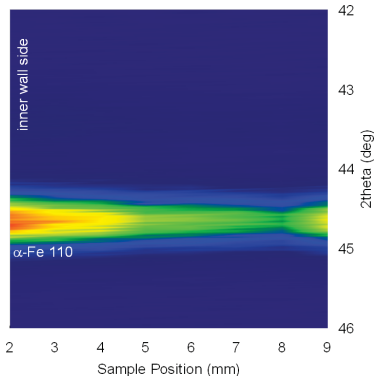

(b)

Figure 1.22.: Representative XRD data collected with a step of 0.8mm across the wall of a steel tube document the variation of diffraction intensity and phases (α-Fe and γ-Fe) at the cross-section (a). In (b), a variation of the intensity of α-Fe 110 reflection across the tube cross-section is a result of a very intensive water cooling at the tube outer wall side.

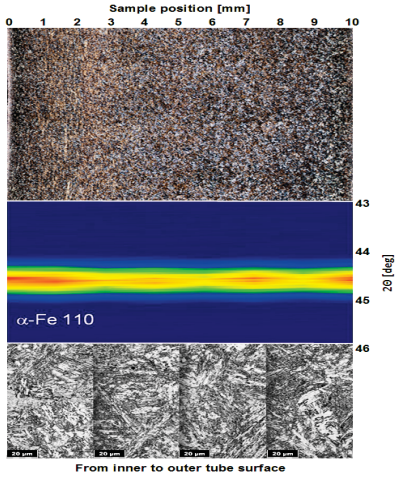

(a) T1

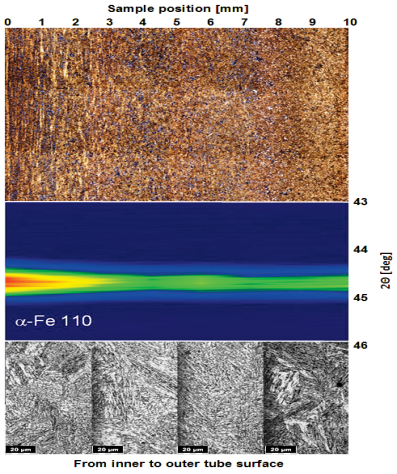

(b) T2

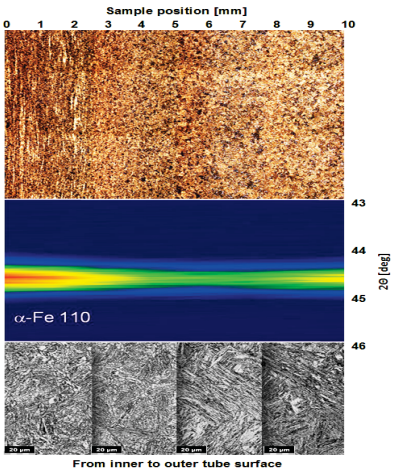

(c) T3

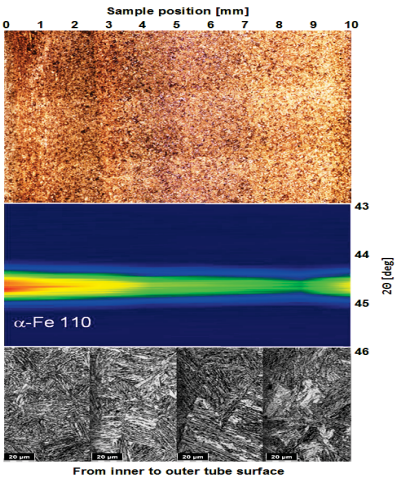

(d) T4

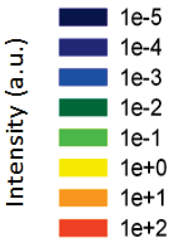

(e) XRD scale for tube T1 to T4

Figure 1.23.: XRD data and micrographs for tube (a) T1 to (d) T4 and (e) XRD scale.

1.3.2. Synchrotron XRD Analysis

Synchrotron characterization of seamless steel tubes was performed at High Energy Materials Science (HEMS) beamline P07 of PETRA III synchrotron source in Hamburg. For the experiments carried out in years 2012 - 2013, high energetic X - rays with the energy up to 100 keV were used.

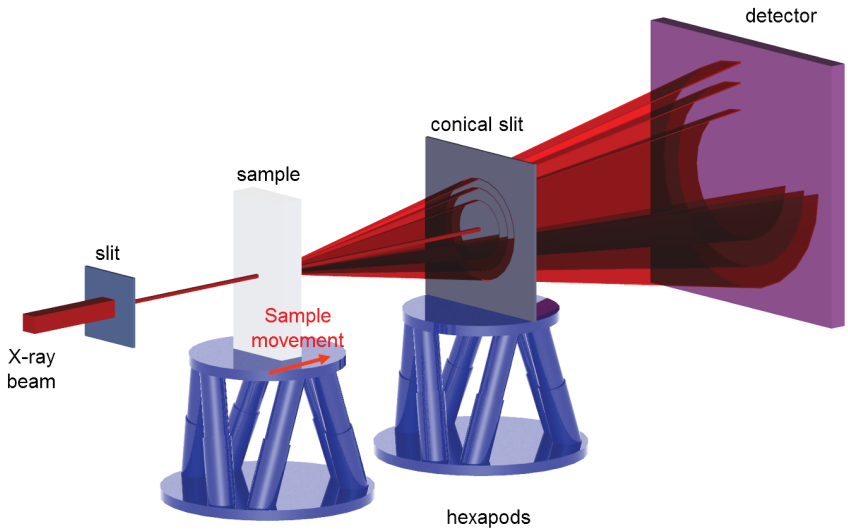

Figure 1.24.: A schematic setup of the conical system used to assess X - ray elastic strains in the sample. By moving the sample along the arrow, it was possible to move the gauge volume across tube wall cross-section [64].

The aim of the experiments was to characterize residual stress gradients (i) in tubes produced under various cooling conditions [75] and (ii) in a bent tube [74]. For the characterization, X - ray beam with the cross section of about 50 µm × 50 µm was used hereby the spatial resolution was about 0.8 mm. In order to perform the depth resolved characterization, a conical slit system was applied (fig. 1.22). The technique is based on an application of a dedicated conical slit, which is placed between sample and two dimensional detector. The slits with a thickness of a few tens microns allows to select only a small portion of diffracted X - ray photons which are then collected by the detector. In this way the gauge volume is defined. By moving the sample in the beam direction, it is possible to characterize various sample regions and evaluate thus strain distribution position-resolved.

1.3.3. Stress Evaluation from Synchrotron Data

In order to evaluate triaxial stresses in seamless steel tubes, X - ray elastic strains were characterized in two sample configurations. At first the X - ray beam was oriented perpendicular to the tube axis and the tube wall was moved across the focus of the conical slits (figs. 1.25a and 1.25b) in x direction with a step of 0.5 mm.

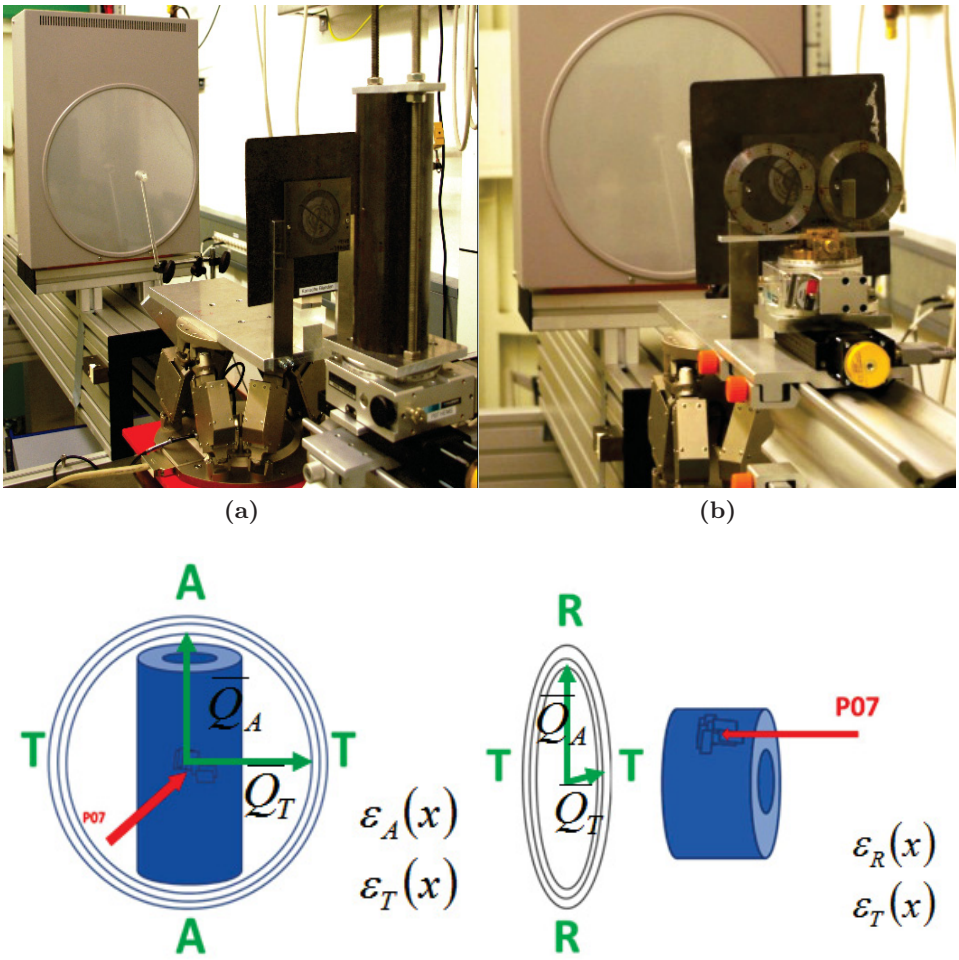

Figure 1.25.: Experimental set-up at HEMS beamline (P07) used to characterize axial and tangential (a,c) as well as radial and tangential (b,d) stresses by using conical slit system. In the first case, the beam is oriented perpendicular (a,c) and parallel (b,d) to the tube axis. The deformation of Debye-Scherrer rings is used to evaluate axial (A), tangential (T) and radial (R) strains ε along the directions of the diffraction vectors $\bar{Q}_A$, $\bar{Q}_T$ and $\bar{Q}_R$.

Simultaneously Debye-Scherrer rings were collected using the 2 D detector. In the next step, the beam was directed parallel to the tube axis and rings cut from tubes (with a thickness of 15 mm) were scanned along the x axis (figs. 1.25c and 1.25d).

At the end the unstressed lattice parameter d_0^{hkl} was determined by scanning small pieces of the tube material [20].

Axial, tangential and radial strains components were calculated according

$$\varepsilon^{hkl}(x) = \frac{d^{hkl}(x) - d_0^{hkl}}{d_0^{hkl}} \tag{1.10}$$

where d_0^{hkl} represents lattice parameter determined using the Bragg's law for axial, tangential and radial orientations of diffractions vectors $\bar{Q_A}$, $\bar{Q}_T$ and $\bar{Q_R}$ (figs. 1.25c and 1.25d).

As a second next, experimentally determined X - ray elastic strains were used to evaluate spatial distribution of triaxial residual stresses using [40]

$$\sigma_i(x,y,z) = \frac{E^{hkl}}{1+\upsilon^{hkl}} \left(\varepsilon_i^{hkl}(x,y,z) + \frac{\upsilon^{hkl}}{1-2\upsilon^{hkl}} \left(\varepsilon_A^{hkl} + \varepsilon_R^{hkl} + \varepsilon_T^{hkl} \right) \right) \tag{1.11}$$

The X - ray elastic constants (XEC) E^{hkl} and υ^{hkl} in equation 1.11 represent in this case the elastic properties of the material and are dependent on the single crystal elastic constants of crystallites, crystallographic texture and grain interaction model. In the present case, XEC constants were calculated using Hill model which represents an arithmetic average of Reuss and Voigt grain interaction models [52].

1.4. Moessbauer Spectroscopy

Radioactive 57Co with 270 days half-life, which may be generated in a cyclotron and diffused into a noble metal like rhodium, serves as the gamma radiation source for 57Fe Moessbauer spectroscopy. 57Co decays by electron capture (EC from K-shell, thereby reducing the proton number, from 27 to 26 corresponding to 57Fe) and initially populates the 136 keV nuclear level of 57Fe with nuclear spin quantum number I = 5/2. This excited state decays after ca. 10 ns and populates, with 85 % probability the 14.4 keV level by emitting 122 keV gamma quanta, with 15 % probability the 136 keV level decays directly to the ground state of 57Fe. The

14.4 keV nuclear state has a half-life of ca. 100 ns, as shown in fig. 1.26. Both the half-life and the emitted gamma quanta of 14.4 keV energy are ideally suited for 57Fe Moessbauer spectroscopy [26].

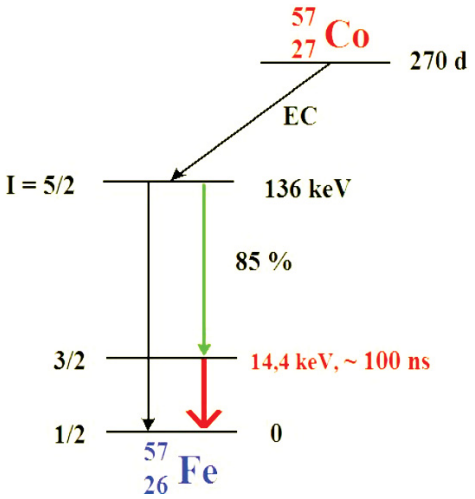

Figure 1.26.: Nuclear decay scheme for 57Fe Moessbauer resonance [26].

Figure 1.27 shows the sampling position of the Moessbauer spectroscopy and transmission electron microscopy. Three material states from differently thermo-mechanical treated tubes were investigated. These investigations were performed at the early stages of the project only on TH01. For TH02 and TH04, the investigations are in progress.

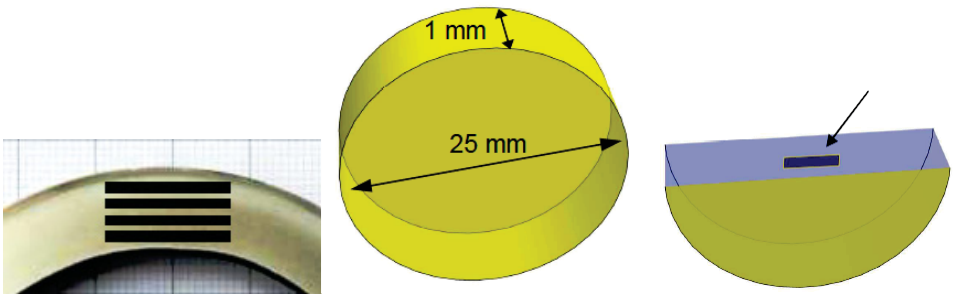

Figure 1.27.: Definition of MS and TEM specimens. Sample positions at the tube wall cross-section (a), sample geometry for MS (b) and TEM sample position made out of MS samples (c) [2].

For each of the three material states, four cylindrical disks were cut out at different positions at the tube wall cross-sections as shown in fig. 1.27. The twelve samples were investigated using MS and TEM techniques. Apparently, the individual discs sampled the material state from the outer down to the inner tube surface. Discs for MS had dimensions 25 mm in diameter and 1 mm in thickness. After MS measurement, disks were cut in half and TEM lamellae were prepared using micro-machining focused ion beam (FIB) method.

57Fe Moessbauer [73, 30, 34, 12] spectra were measured in scattering geometry using a standard Moessbauer spectrometer in a constant acceleration mode with a 57Co(Rh) radioactive source. A pure α-Fe disc was used as a calibration standard for the velocity scale. The spectra were measured at room temperature. The relative contents of individual Fe-bearing phases were monitored through the corresponding spectral areas [31, 32]. In the Moessbauer spectra only body centred phases (α or α') were detected. It is represented by three six line patterns (exemplarily shown in fig. 1.28) corresponding to nearest neighbourhoods of iron atoms which are occupied by different numbers of alloying elements. The low detection limit for austenite in low carbon steels by Moessbauer phase analysis is about 0.5 wt.%. No signal from γ phase was observed. The micro-grain size varies largely between a fraction of micrometer up to about 10 μm.

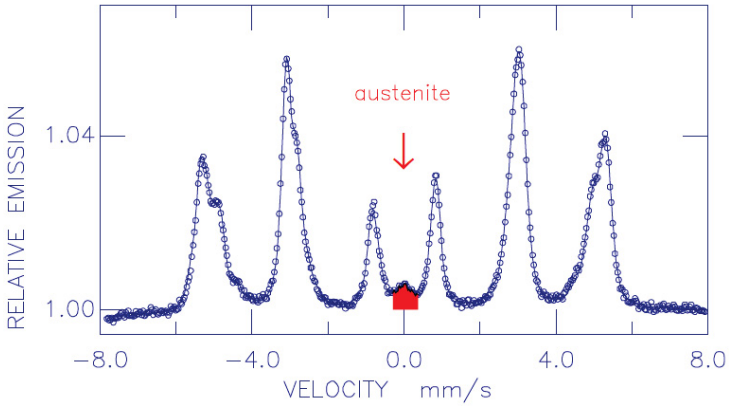

Figure 1.28.: An example of a Moessbauer spectrum obtained from plain steel which contained a small volume fraction of the retained austenite [2]. The position of the austenite component in the spectrum is highlighted.

1.5. DEFORM^{HT}

The DEFORM^{HT} heat treating simulation software was used to calculate and predict the microstructure, mechanical properties as well as residual stresses states as a function of applied cooling rates. The built model visualized in fig. 1.29 shows (i) the meshed tube and (ii) the cooling device.

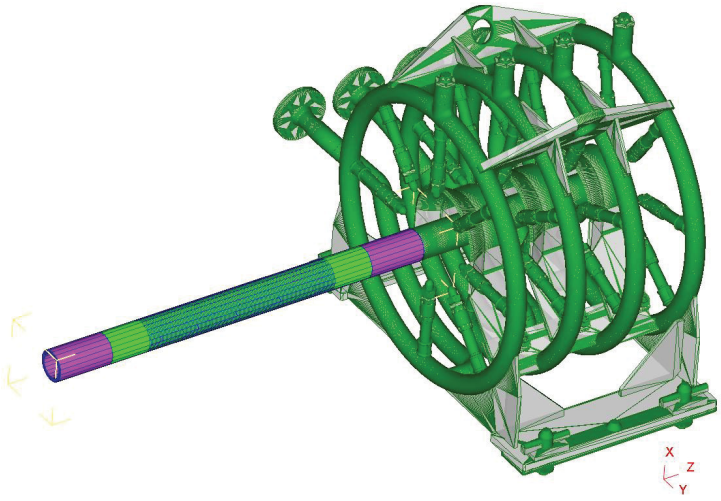

Figure 1.29.: A representative sketch of the cooling device in the Deform model.

The green high lighted surface areas of the tube display the cooling zone. The magenta coloured area represents the uncooled surface area in agreement with the real configuration. The absence of the cooling on the tube edges fig. 1.29 should prevent the tube filling with the cooling water. The (surface) spray water cooling process in the real production includes ten pieces of the cooling device assembled in a production chain (fig. 1.29). Also in the FEM model, the impact of ten devices, implemented as environment windows, was considered.

The initial material database was pre-calculated with the software JMAT-Pro. The calculated material data didn't follow the measured phase transformation behaviour exactly due to too high values of the latent heat utilized in the model. The transition between bcc phases as well as from fcc to bcc phases shown in fig. 1.30 displays this behaviour and differed up to 25 phase volume fraction. A significant achievement in the model accuracy compared to the real process conditions was done by applying a user routine to distinguish between upper and lower bainitic phases.

The model was further feed with experimentally recorded (i) hot flow curves, (ii) heat-transfer-coefficients (as function of water amount and pressure) as well as (iii) air-flow-data of the rake type cooling bed. In respect to the discussed optimizations, the FEM-model was positive validated.

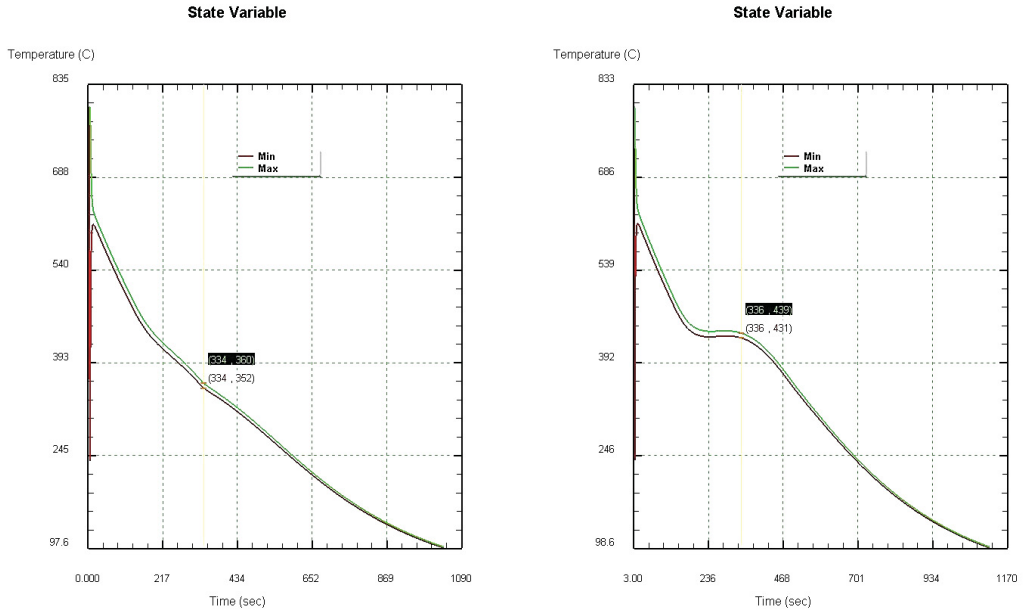

Figure 1.30.: Deform model latent heat problem, (a) JMAT-Pro data and (b) real data.

1.6. Alloying concept studies

1.6.1. Continuous cooling transformation - JMAT-Pro

The cooling rate transformation behaviour as well as the mechanical properties of TH02 (shown in figure 1.31) and TH04 (shown in figure 1.32) are pre-calculated with the software package JMAT-Pro [59, 60]. The alloying concepts (shown in table 1.3) are designed incrementally by single alloy additions. In accordance to alloyed elements, the transition behaviour as well as the improved mechanical behaviour are validated. Currently, the package does not provide data on the toughness behaviour. In order to quantify the toughness, novel test heats of 60 tons each have been ordered and mechanical testing will be necessary to reveal this behaviour.

The corresponding [76] CCT diagrams are constructed (figs. 1.31 and 1.32), which involved the formation curves of martensite, bainitic ferrite, ferrite and pearlite,

depending on cooling rate and transformation temperature [35].

A rapid cooling rate depressed the formation of pearlite and quasi-polygonal ferrite, which resulted in higher hardness. Hot deformation strongly promoted the acicular ferrite formation which did not form under non-deformation conditions. Small boron addition effectively reduced the formation of pearlite and ferrite and broadened the cooling rate region for bainitic ferrite and martensite. The evaluation of UHSTMRT properties was based on the analysis of the transition kinetic and the cooling rates. All pre-calculated results provide a fine grained microstructure as well as the expected mechanical properties. At transformation temperatures in the area of bainitic microstructure, excellent high strength and Charpy-V-toughness are expected. The effect of thermo-mechanical [3] control during processing are investigated by focusing on the influence of the intermediate cooling stage.

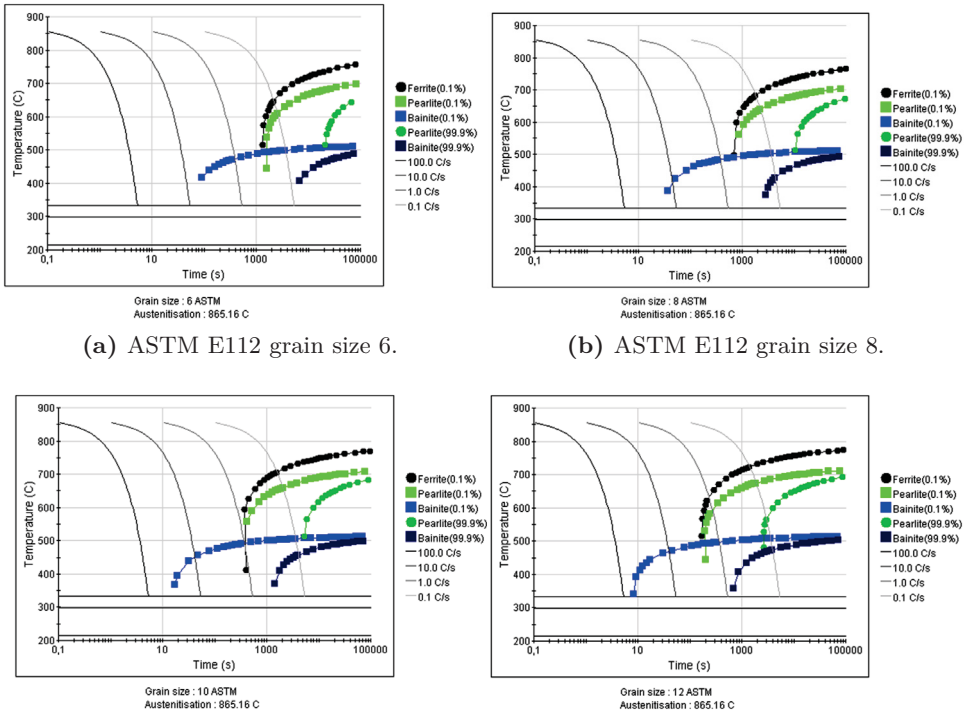

(a) ASTM E112 grain size 6.

(b) ASTM E112 grain size 8.

(c) ASTM E112 grain size 10.

(d) ASTM E112 grain size 12.

Figure 1.31.: CCT TH02, for ASTM E112 grain size (a) 6, (b) 8, (c) 10 and (d) 12.

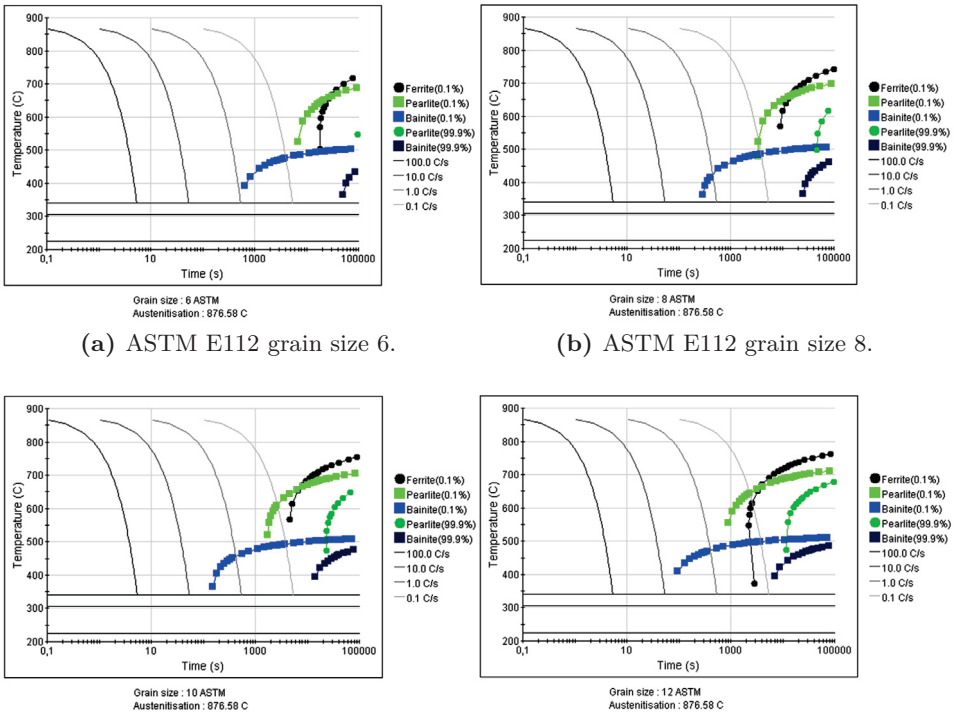

(a) ASTM E112 grain size 6. **(b)** ASTM E112 grain size 8.

(c) ASTM E112 grain size 10. **(d)** ASTM E112 grain size 12.

Figure 1.32.: CCT TH04, for ASTM E112 grain size (a) 6, (b) 8, (c) 10 and (d) 12.

1.6.2. Continuous cooling transformation - Gleeble 3800 simulator

The dilatometric curves of TH02 and TH04 at different cooling rates were investigated on Gleeble-3800 thermo-mechanical simulator [44]. The CCT curves of hot deformation were determined using thermal dilation measurement and referenced by microstructure observation. The validation of the pre-calculated CCTs by JMAT - Pro as well as a set of data was required to optimize the accuracy of the FEM microstructure-evolution-model. The machined specimens presented in fig. 1.33, are taken from an intermediate cooled, as rolled tube OD of 168,3 mm and WD 20.0 mm, to feed the unit. The specimens were directly taken out from the centre of the tube cross-section. Metallographic examinations confirmed the appointed grain size 10 according to the ASTM standard E 112. The samples are heated up above austenitization temperature to 930 °C with 5 K/sec. This temperature was applied for 300 sec to achieve homogeneous conditions over the whole specimen volume. The specimen geometry was chosen to perform tests with high cooling rates

achieved by argon flushing. The tested cooling rates: $\lambda_{t85} = 180$ (18000 sec from 800 °C to 500 °C), $\lambda_{t85} = 45$ (4500 sec), $\lambda_{t85} = 12$ (1200 sec), $\lambda_{t85} = 3$ (300 sec), $\lambda_{t85} = 0.5$ (50 sec), $\lambda_{t85} = 0.1$ (10 sec), $\lambda_{t85} = 0.03$ (3 sec). Complementarily to this main testing matrix, other ASTM grain sizes from 8 to 14 were tested to reveal a microstructure depending relationship [4], if any [42]. The (accelerated) cooling rate influence was studied, as well as the microstructure and further mechanical properties of TH02 and TH04. The revealed ACR's from this investigations are providing reference parameters for TM tube manufacturing. The experimentally obtained results correlate well with the functional properties of the products. The investigated CCT and the micrographs for TH02 are given in figures 1.34 and 1.35.

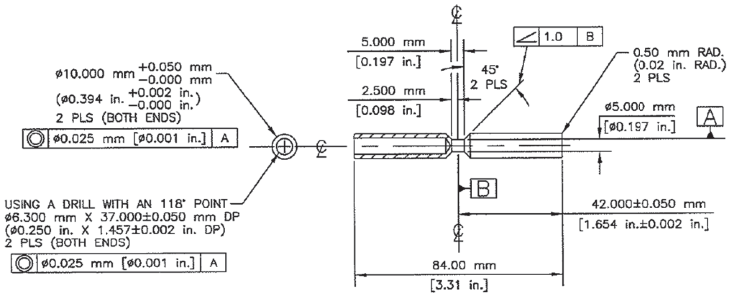

Figure 1.33.: CCT specimen geometry for Gleeble 3800 simulator.

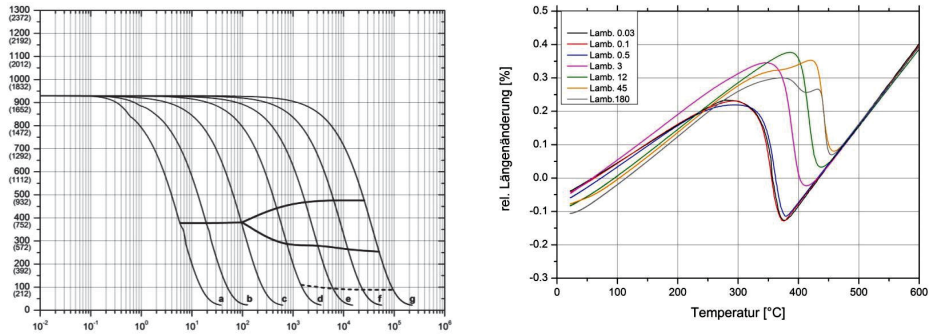

Figure 1.34.: TH02 CCT phase diagram and observed dilatometric curves (a) $\lambda_{t85} = 0.03$, (b) $\lambda_{t85} = 0.1$, (c) $\lambda_{t85} = 0.5$, (d) $\lambda_{t85} = 3.0$, (e) $\lambda_{t85} = 12$, (f) $\lambda_{t85} = 45$, (g) $\lambda_{t85} = 180$.

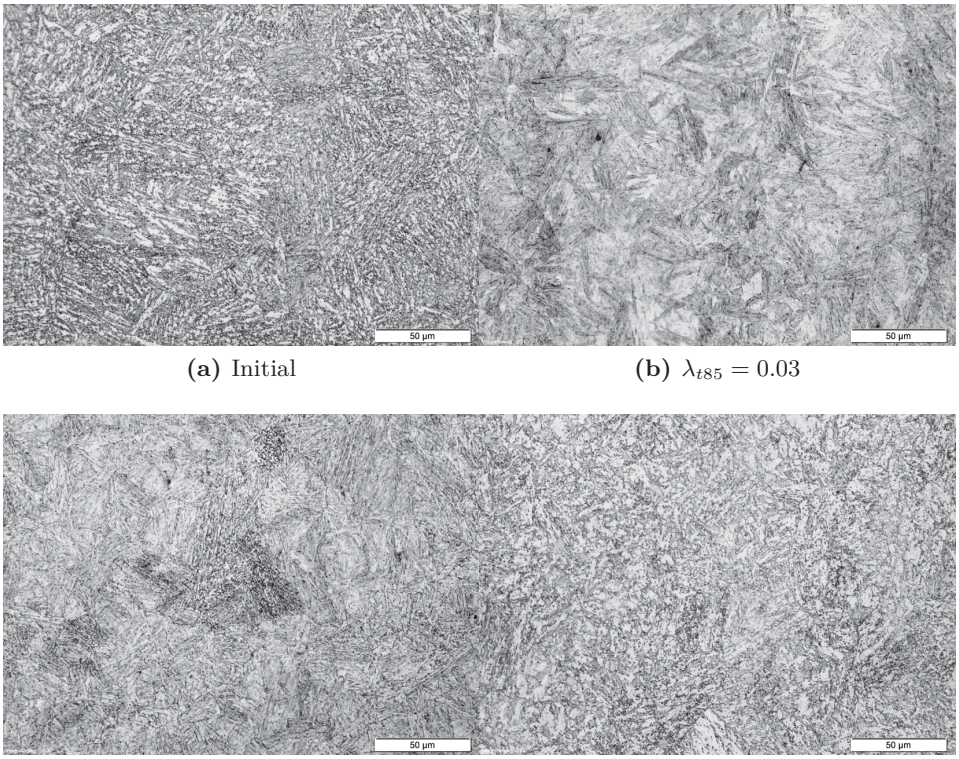

(a) Initial **(b)** $\lambda_{t85} = 0.03$

(c) $\lambda_{t85} = 3.0$ **(d)** $\lambda_{t85} = 180$

Figure 1.35.: Micrograph of CCT specimens - magnification 500x
(a) Initial (b) $\lambda_{t85} = 0.03$, (c) $\lambda_{t85} = 3$, (d) $\lambda_{t85} = 180$.

1.6.3. Servotest - hot flow curve detection

Hot flow curves were investigated to determine flow stresses at the temperatures equal to the processing route [18]. This analyses was performed on a servotest TMTS device, the specimen (rastagaev) geometry is shown in figure 1.36. The specimen geometry in TMTS tests was optimized to reduce the friction coefficient during the deformation. On the specimen face, a hole to mount a thermocouple for temperature control during the analysis was drilled in. A temperature profile during the processing is presented schematically in fig. 1.37. The processing stages (a) to (h) are explained in table 1.11.

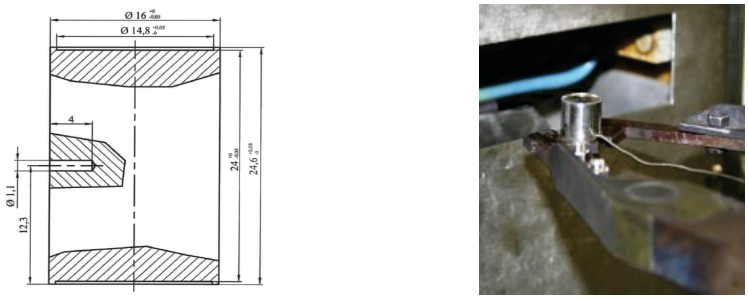

Figure 1.36.: (a) Rastagaev specimen, (b) mounted specimen in TMTS-device.

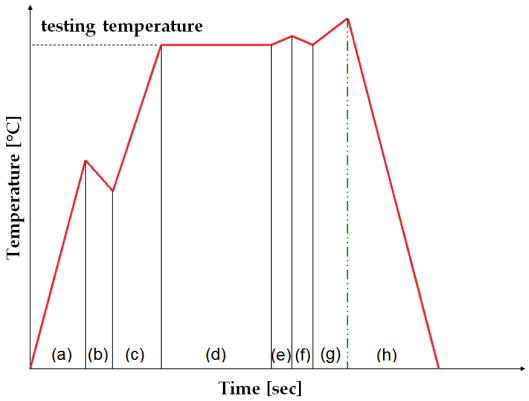

Figure 1.37.: A schematic dependence of the specimen temperature during hot-flow curve detection test.

Stage	Stage description
(a)	Inductive specimen preheating at device furnace with 15 K/sec to 650 °C.
(b)	Specimen recesses are dipped with glass powder.
(c)	Inductive specimen heating with 15 K/sec to 930 °C.
(d)	Temperature hold for 120 sec at 930 °C for homogeneous forming conditions.
(e)	Specimen heated to 945 °C to maintain testing temperature after manipulation.
(f)	Specimen manipulation to the forming device.
(g)	Specimen compressed according to testing matrix shown in table 1.12.
(h)	Specimen quenched in water-bath.

Table 1.11.: Servotest temperature curve stages (a) to (h) explanation according to fig. 1.37.

The testing matrix with the strain rates and temperatures is shown in table 1.12. The applied glass powder at stage (b) minimized the friction coefficient between material an dies. So the specimen shape was constant during forming and not convexly or concavely shaped.

Testing matrix	**Strain rate**			
	0.1/sec	**0.5/sec**	**1/sec**	**5/sec**
Temperature	☑	☑	☑	☑
800 °C	☑	☑	☑	☑
900 °C	☑	☑	☑	☑
1000 °C	☑	☑	☑	☑
1100 °C	☑	☑	☑	☑
1200 °C	☑	☑	☑	☑

Table 1.12.: Parameter matrix used for servotest on TH02 and TH04.

The flow strain calculation out of the measured [16] force-path data is valid under the assumption of the uni-axial stress condition and constant volume, as shown in equation 1.12 and 1.13.

$$k_f = \frac{F}{A} = \frac{F \cdot h}{A_0 \cdot h_0} = \frac{F}{A_0} \cdot e^{\varphi} \tag{1.12}$$

$$\varphi = ln\frac{h}{h_0} \tag{1.13}$$

Due to the fact that the sample is heated by the deformation itself, the measured flow strains are lower than the real values. This non-isothermal flow curves are converted to isothermal flow curves, according to known data of specific heat and density of the equivalent deformation temperature. In the following sections the isothermal and the non-isothermal flow curves are described. The calculation for the isothermal flow curve is shown in equation 1.14 as well as the temperature increase due to the deformation heat in equation 1.15.

$$k_f \cdot \varphi \cdot V = c_p \cdot \rho \cdot V \cdot \Delta\vartheta \tag{1.14}$$

$$\Delta\vartheta = \frac{k_f \cdot \varphi}{c_p \cdot \rho} \tag{1.15}$$

The hot flow curves for TH02 are displayed in figures 1.38 and 1.39 as well as for TH04 in figures 1.40 and 1.41.

Figure 1.38.: Colour scale for investigated hot flow curves, shown in fig. 1.39, dashed lines for measured curves and full lines for isothermal corrected curves.

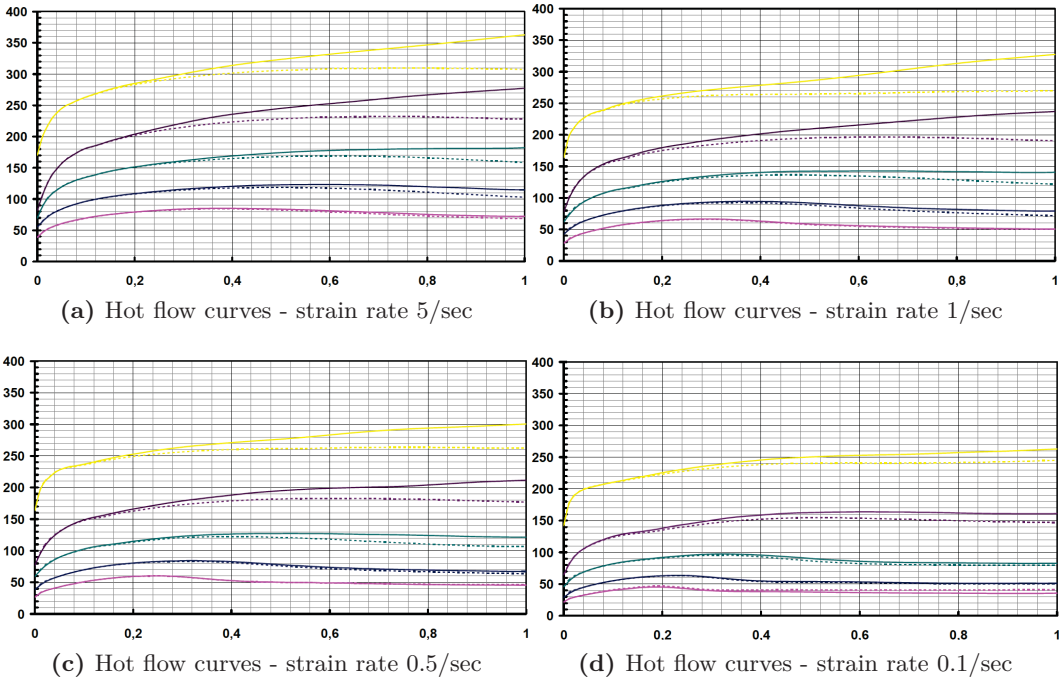

(a) Hot flow curves - strain rate 5/sec

(b) Hot flow curves - strain rate 1/sec

(c) Hot flow curves - strain rate 0.5/sec

(d) Hot flow curves - strain rate 0.1/sec

Figure 1.39.: Hot flow curves (k_f over $\dot{\varphi}$) for TH 02, investigated with servotest TMTS, strain rate (a) 5/sec, (b) 1/sec, (c) 0.5/sec and (d) 0.1/sec.

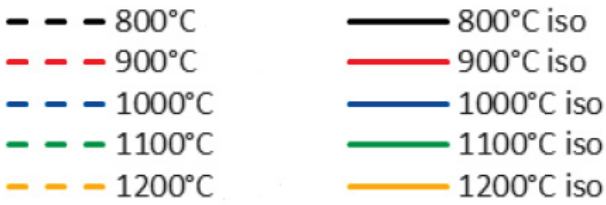

Figure 1.40.: Colour scale for investigated hot flow curves, shown in fig. 1.41, dashed lines for measured curves and full lines for isothermal corrected curves.

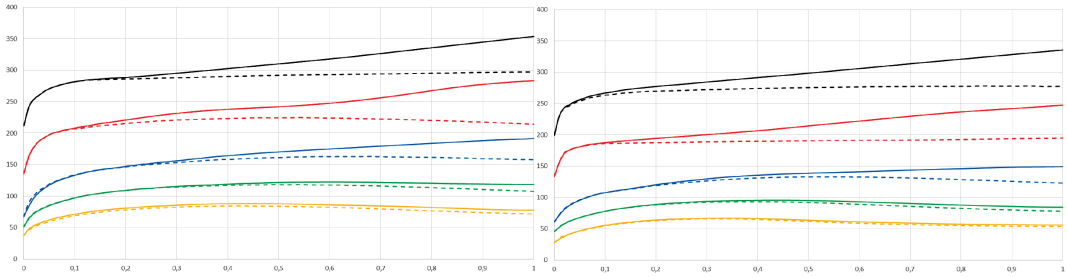

(a) Hot flow curves - strain rate 5/sec

(b) Hot flow curves - strain rate 1/sec

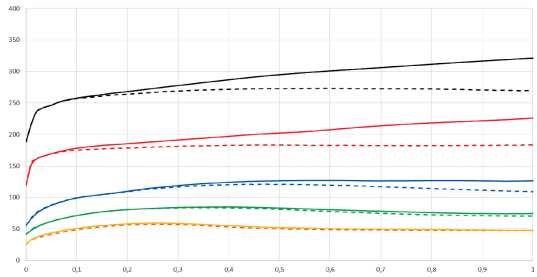

(c) Hot flow curves - strain rate 0.5/sec

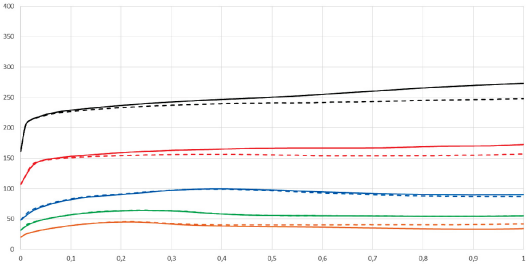

(d) Hot flow curves - strain rate 0.1/sec

Figure 1.41.: Hot flow curves (k_f over $\dot{\varphi}$) for TH 04, investigated with servotest TMTS, strain rate (a) 5/sec, (b) 1/sec, (c) 0.5/sec and (d) 0.1/sec.

[1] International institute of welding. Note on the carbon equivalent. Vol6 No2, 1968.

[2] Dlouhy Antonin. Report hs 7020-14 - moessbauer spectroscopy and tem of steel samples. Technical report, IPM (CZ), 2014.

[3] Toru Araki, Masato Enomoto, and Koji Shibata. Microstructural aspects of bainitic and bainite-like ferritic structures of continuously cooled low carbon hsla steels. *Materials Transactions, JIM*, 32(8):729–736, 1991.

[4] S. S. Babu and H. K. D. H. Bhadeshia. Mechanism of the transition from bainite to acicular ferrite. *Materials Transactions, JIM*, 32(8):679–688, 1991.

[5] K Baines. Lead as a model material to simulate mandrel rolling of hot steel tube. *Journal of Materials Processing Technology*, 118(13):422 – 428, 2001.

[6] Laila S. Bayoumi. Analysis of flow and stresses in a tube stretch-reducing hot rolling schedule. *International Journal of Mechanical Sciences*, 45(3):553 – 565, 2003.

[7] Emin Bayraktar, Dominique Kaplan, and Marc Grumbach. Application of impact tensile testing to spot welded sheets. *Journal of Materials Processing Technology*, 153(0):80 – 86, 2004. Proceedings of the International Conference in Advances in Materials and Processing Technologies.

[8] W. Bleck. Advanced high strength steels for the automotive industry. *Stahl und Eisen 134, Nr.7, page 25-34*, 2014.

[9] A. Bodin, J. Sietsman, and S. Van Der Zwaag. Texture and microstructure development during intercritical rolling of low-carbon steels. *Metallurgical and Materials Transactions A*, 33(6):1589–1603, 2002.

[10] William Bragg. *Die Welt des Lichtes: The Universe of Light*. Vieweg and Teubner Verlag, 1935.

[11] William Bragg. *Concerning the nature of things*. Courier Corporation, 1925.

[12] P. Bruna, I. Mejia, J. Cabrera, and T. Pradell. Rare earth additions in a ferritic steel a moessbauersbauer study. In MichaelF. Thomas, JohnM. Williams, and TerenceC. Gibb, editors, *Hyperfine Interactions*, pages 523–527. Springer Netherlands, 2002.

[13] B. Buchmayr and J. Klarner. Optimierung von prozessketten fuer rohrfoermige endprodukte. *Aachener Stahlkolloquium*, 28, 2013. cited By (since 1996)1.

[14] Marion Calcagnotto, Yoshitaka Adachi, Dirk Ponge, and Dierk Raabe. Deformation and fracture mechanisms in fine- and ultrafine-grained ferrite/martensite dual-phase steels and the effect of aging. *Acta Materialia*, 59(2):658–670, 2011.

[15] Marion Calcagnotto, Dirk Ponge, and Dierk Raabe. Effect of grain refinement on strength and toughness of dual-phase steels. *Materials Science and Engineering: A*, 527(29 and 30):7832–7840, 2010.

[16] Stoeckl Christian. Untersuchungsbericht zur bestimmung von fliesskurven - versuchsschmelze 02. Technical report, University of Leoben - Department Product Engineering, Chair of Metal Forming, 2014.

[17] W. Dobrucki and P. Sobkowiak. Laboratory investigation of the continuous seamless-tube rolling process (mandrel mill process) using models. *Journal of Mechanical Working Technology*, 19(3):285 – 294, 1989.

[18] E. Doege, H. Meyer-Nolkemper, and I. Saeed. *Fliesskurvenatlas metallischer Werkstoffe: mit Fliesskurven fuer 73 Werkstoffe und einer grundlegenden Einfuehrung*. Hanser, 1986.

[19] Ahmed Ismail Zaky Farahat and S.A. El-Badry. Effect of high temperature deformation and different cooling rates on microstructure and mechanical properties. *Materials Science and Engineering: A*, 525(12):48 – 54, 2009.

[20] M.E Fitzpatrick. *Analysis of Residual Stress by Diffraction Using Neutron and Synchrotron Radiation*. Taylor and Francis, London and New York, 2003.

[21] Francisca Garcia Caballero, Carlos Capdevila, Jesus Chao, J Cornide, Carlos Garcia Mateo, H Roelofs, St Hasler, G Mastrogiacomo, et al. The microstructure of continuously cooled tough bainitic steel. *2nd Int Conf. Super-High Strength Steels*, 2010.

[22] Leif Gerward. X-ray attenuation coefficients: current state of knowledge and availability. *Radiation Physics and Chemistry*, 41(4):783–789, 1993.

[23] Antonio Augusto Gorni and JHD SILVEIRA. Accelerated cooling of steel plates: The time has come. *Journal of ASTM International*, 5(8):7, 2008.

[24] A Grajcar, M Kaminska, M Opiela, P Skrzypczyk, B Grzegorczyk, and E Kalinowska-Ozgowicz. Segregation of alloying elements in thermomechanically rolled medium-mn multiphase steels. *Journal of Achievements in Materials and Manufacturing Engineering*, 55(2):256–264, 2012.

[25] Ylva Granbom. *Structure and mechanical properties of dual phase steels.* PhD thesis, KTH, Stockholm, Sweden, 2010.

[26] Philipp Guetlich. *The Principle of the Moessbauer Effect and Basic Concepts of Moessbauer Spectrometry.* uni lemans france, http://pecbip2.univ-lemans.fr/webibame/, 04 2015.

[27] Seong-Ho Han, Shi-Hoon Choi, Jae-Kwon Choi, Hwan-Goo Seong, and In-Bae Kim. Effect of hot-rolling processing on texture and r-value of annealed dual-phase steels. *Materials Science and Engineering: A*, 527(7–8):1686 – 1694, 2010.

[28] Bob B He. *Two-dimensional X-ray diffraction.* John Wiley and Sons, 2011.

[29] Baltazar V. H. Hernandez, M. L. Kuntz, M. I. Khan, and Y. Zhou. Influence of microstructure and weld size on the mechanical behaviour of dissimilar ahss resistance spot welds. *Science and Technology of Welding and Joining*, 13(8):769–776, 2008.

[30] L. Herojit Singh, S.S. Pati, A.C. Oliveira, and V.K. Garg. Moessbauer study of stability and growth confinement of magnetic fe3o4. *Hyperfine Interactions*, pages 1–7, 2014.

[31] Seyed Mohammad Kazem Hosseini, Abbass Zaeri-Hanzaki, and Steve Yue. Effect of austenite deformation in non-recrystallization region on microstructure development in low-silicon content trip-assisted steels. *Materials Science and Engineering A*, 618(0):63 – 70, 2014.

[32] Allen H. Hunter, Jeffrey D. Farren, John N. DuPont, and David N. Seidman. An atom-probe tomographic study of arc welds in a multi-component high-strength low-alloy steel. *Metallurgical and Materials Transactions A*, 44(4):1741–1759, 2013.

[33] P.J. Hurley and P.D. Hodgson. Formation of ultra-fine ferrite in hot rolled strip: potential mechanisms for grain refinement. *Materials Science and Engineering: A*, 302(2):206 – 214, 2001.

[34] P. Jacques, F. Delannay, X. Cornet, Ph. Harlet, and J. Ladriere. Enhancement of the mechanical properties of a low-carbon, low-silicon steel by formation of a multiphased microstructure containing retained austenite. *Metallurgical and Materials Transactions A*, 29(9):2383–2393, 1998.

[35] H.J. Jun, J.S. Kang, D.H. Seo, K.B. Kang, and C.G. Park. Effects of deformation and boron on microstructure and continuous cooling transformation in low carbon hsla steels. *Materials Science and Engineering A*, 422(12):157–162, 2006. NANOAM.

[36] JU SEOK KANG and CHAN GYUNG PARK. Characterization of bainitic microstrucutres in low carbon hsla steels. *International Journal of Modern Physics B*, pages 593–598, 2008.

[37] Enda Keehan. *Effect of microstructure on mechanical properties of high strength steel weld metals*. PhD thesis, Chalmers University of Technology and Goeteborg University, 2004.

[38] N.J. Kim, A.J. Yang, and G. Thomas. Effect of finish rolling temperature on the structure and properties of directly quenched nb containing low carbon steel. *Metallurgical Transactions A*, 16(3):471–474, 1985.

[39] J Klarner, B Buchmayr, and W Rainer. Toughtubes, extrem feinkoernige nahtlose stahlrohre. *BHM*, 156(5):168–174, 2011.

[40] J. B. Cohen. Klimanek, P.I. C. Noyan. Residual stress measurement by diffraction and interpretation. *Crystal Research and Technology*, 24(2), 1989.

[41] Chenna Krishna S, Narendra Kumar Gangwar, Abhay K. Jha, Bhanu Pant, and Koshy M. George. Microstructure and properties of 15cr-5ni-1mo-1w martensitic stainless steel. *steel research international*, 86(1):51–57, 2015.

[42] Roman Kuziak. Physical simulation of thermomechanical treatment employing gleeble 3800 simulator. *Institute for Ferrous Metallurgy, Gliwice, Poland*, 2006.

[43] HA Lanjewar, Pranav Tripathi, D Satish Kumar, M Singhai, and PK Patra. Effect of transformation temperature and accelerated cooling on development of strength in plain carbon steel with ferritic structure. *Journal of Steel and Related Materials*, 2013.

[44] ZHAO Baochun LI Guiyan LIU Yonghao YANG Jing HUANG Lei. Detection and analysis of cct curve of low-carbon micro-alloyed steel with mo. *Hot Working Technology*, 2008.

[45] Hongfei Li, Guangwei Fan, Yan He, Jingang Bai, Caili Zhang, and Peide Han. Austenite transformation behaviour of 2205 duplex stainless steels under hot tensile test. *steel research international*, 86(1):84–88, 2015.

[46] DIPESH KUMAR Mishra. *Thermo-mechanical Processing of API X60 grade pipe line steel*. PhD thesis, NIOT Roukela, 2014.

[47] Ali Mkaddem, Faiez Gassara, and Ridha Hambli. A new procedure using the microhardness technique for sheet material damage characterisation. *Journal of Materials Processing Technology*, 178(13):111 – 118, 2006.

[48] Hardy Mohrbacher. Principal effects of mo in hsla steels and cross effects with microalloying elements. *Central Iron and Steel Research Institute (CISRI)*, pages 75–96, 2010.

[49] Hardy Mohrbacher. The development of niobium microalloyed steel for the production of seamless tubes. In *Metal: 2006 15 th International metallurgical and materials conference*, page 1, 2006.

[50] Shahrooz Nafisi, Muhammad Arafin, Robert Glodowski, Laurie Collins, and Jerzy Szpunar. Impact of vanadium addition on api x100 steel. *ISIJ International*, 54(10):2404–2410, 2014.

[51] R. Narayanasamy, N.L. Parthasarathi, and C. Sathiya Narayanan. Effect of microstructure on void nucleation and coalescence during forming of three different {HSLA} steel sheets under different stress conditions. *Materials & Design*, 30(4):1310 – 1324, 2009.

[52] I. C. Noyan, T. C. Huang, and B. R. York. Residual stress/strain analysis in thin films by x-ray diffraction. *Critical Reviews in Solid State and Materials Sciences*, 20(2):125–177, 1995.

[53] W Ozgowicz, M Opiela, A Grajcar, E Kalinowska-Ozgowicz, and W Krukiewicz. Metallurgical products of microalloy constructional steels. *Journal of Achievements in Materials and Manufacturing Engineering*, 44(1):7–34, 2011.

[54] Zbigniew Pater and Jan Kazanecki. Thermo-mechanical analysis of piercing plug loads in the skew rolling process of thick-walled tube shell. *Metallurgy and Foundry Engineering*, 32:31–40, 2006.

[55] R Pschera, J Klarner, and C Sommitsch. Finite elemente analyse der reibungsbedingungen beim schraegwalzen mit diescherscheiben. In *Proceedings Seminar Rohrherstellung und -verarbeitung*, pages 59–69. LUT, 2007.

[56] K.K. Ray, D. Chakraborty, and S. Ray. Toughness characterization of niobium-bearing hsla steels. *Journal of Materials Science*, 29(4):921–928, 1994.

[57] P.C.M. Rodrigues, E.V. Pereloma, and D.B. Santos. Mechanical properities of an hsla bainitic steel subjected to controlled rolling with accelerated cooling. *Materials Science and Engineering A*, 283(12):136 – 143, 2000.

[58] Arindam Sarkar. *A development study of Microalloyed steel (HSLA) through experimental exploration.* PhD thesis, National Institute of Technology Rourkela, 2012.

[59] N. Saunders, U.K.Z. Guo, X. Li, A.P. Miodownik, and J.-Ph. Schille. Using jmatpro to model materials properties and behavior. *JOM*, 55(12):60–65, 2003.

[60] N Saunders, Z Guo, X Li, AP Miodownik, and J Ph Schille. The calculation of ttt and cct diagrams for general steels. *JMatPro Software Literature*, 2004.

[61] Kun Shi, Hong Hou, Jiang-Biao Chen, Ling-Ti Kong, Han-Qian Zhang, and Jin-Fu Li. Effect of bainitic packet size distribution on impact toughness and its scattering in the ductile and brittle transition temperature region of qandt mn-ni-mo bainitic steels. *steel research international*, 2015.

[62] R. Song, D. Ponge, and D. Raabe. Mechanical properties of an ultrafine grained steel processed by warm deformation and annealing. *Acta Materialia*, 53(18):4881–4892, 2005.

[63] R. Song, D. Ponge, D. Raabe, J.G. Speer, and D.K. Matlock. Overview of processing, microstructure and mechanical properties of ultrafine grained bcc steels. *Materials Science and Engineering: A*, 441(12):1–17, 2006.

[64] Trans Tech Publ. *Depth-resolved residual stress analysis with high-energy synchrotron X-rays using a conical slit cell*, volume 768, 2014.

[65] Imao Tamura, Hiroshi Sekine, and Tomo Tanaka. *Thermomechanical processing of high-strength low-alloy steels*. Butterworth-Heinemann, 2013.

[66] B. Tanguy, J. Besson, R. Piques, and A. Pineau. Ductile to brittle transition of an a 508 steel characterized by charpy impact test: Part i: experimental results. *Engineering Fracture Mechanics*, 72(1):49 – 72, 2005.

[67] Alexander Timoshenkov, Piotr Warczok, Mihaela Albu, Juergen Klarner, Ernst Kozeschnik, Gerald Gruber, and Christof Sommitsch. Influence of deformation on phase transformation and precipitation of steels for oil country tubular goods. *steel research international*, 85(6):954–967, 2014.

[68] J.A. Todd and P. Li. Microstructure-mechanical property relationships in isothermally transformed vanadium steels. *Metallurgical Transactions A*, 17(7):1191–1202, 1986.

[69] Bertram Eugene Warren. *X-ray Diffraction*. Courier Corporation, 1969.

[70] H-R Wenk and P Van Houtte. Texture and anisotropy. *Reports on Progress in Physics*, 67(8):1367, 2004.

[71] Stahl Eisen Werkstoffblatt. Sew 088:1993 sew 088:1993 weldable fine grained steels; guidelines for processing, particular for fusion welding. Technical rule, 10 1993.

[72] Stahl Eisen Werkstoffblatt. Din sew 090-2 high tenacity quenched and tempered fine grain steel part 2: Technical delivery conditions for tube and hollow sections, 1993.

[73] D.L. Williamson, R.G. Schupmann, J.P. Materkowski, and G. Krauss. Determination of small amounts of austenite and carbide in hardened medium carbon steels by moessbauer spectroscopy. *Metallurgical Transactions A*, 10(3):379–382, 1979.

[74] Gerald Winter, Juergen Klarner, Bruno Buchmayr, and Jozef Keckes. Experimental characterization and modelling of residual stress gradients across straight and bent seamless steel tubes. *ESAFORM*, 2015.

[75] Gerald Winter, Mario Stefenelli, Juergen Klarner, Peter Staron, Torben Fischer, Jozef Keckes, and Bruno Buchmayr. Triaxial residual stresses in thermomechanically rolled seamless tubes characterized by high-energy synchrotron x-ray diffraction. *ASME PVP*, pages V003T03A020–V003T03A020, 2013.

[76] M. Zhang, L. Li, R.Y. Fu, D. Krizan, and B.C. De Cooman. Continuous cooling transformation diagrams and properties of micro-alloyed trip steels. *Materials Science and Engineering: A*, 438(0):296–299, 2006. Proceedings of the International Conference on Martensitic Transformations.

[77] Xiao guang ZHOU, Zhen yu LIU, Sheng yong SONG, Di WU, and Guo dong WANG. Upgrade rolling based on ultra fast cooling technology for c-mn steel. *Journal of Iron and Steel Research, International*, 21(1):86 – 90, 2014.

2

Discussion of Results

The results from the experimental investigations are discussed in this chapter. The discussion was grouped into sub - chapters, according to the UHSTMRT as well as thesis targets, listed in table 2.1. The discussion and interpretation comprise not only the scientific findings but also reflect specific experimental difficulties, advantages and disadvantages of the methods, main results, methods accuracy and comparability. The results from the tubes obtained using novel alloying concepts are compared with the results from a reference QaT tube.

UHSTMRT targets	
Dependence of residual stress state in tubes on the applied ACR intensity	✓
Microstructure- and phase gradients across the tube wall as function of applied ACR intensity	✓
Transition behaviour of developed alloying concepts	✓
Macro mechanical behaviour characterization	✓
Micro mechanical behaviour characterization	✓
Weldability and weld - application - performance characterization	✓
Lifetime performance characterization and market launch	⊛

Table 2.1.: UHSTMRT targets. Status: ✓- accomplished; ⊛- outlook;

In accordance with the above listed targets and the related areas of interest, the applied investigation methods and their major scopes were described in tables 2.2 (Fundamental material characterization), 2.3 (mechanical material characterization), 2.4 (residual stress characterization), 2.5 (metallographic and microscopic material characterization), 2.6 (X - ray diffraction material characterization) and 2.7 (weldability characterization).

Fundamental material characterization	
Hot flow curves	Reveal the required hot forming forces during the tube manufacture processing.
CCT curves	Reveal the transition behaviour of the alloying concepts and test heats. Pre - calculation by software package JMAT - PRO; Experimental devices: Gleeble and TA dilatometer;
Moessbauer spectroscopy	Quantitative phase analyses to determine the volume fraction of fcc and bcc phases.
Spark optical emission spectroscopy	Quantitative alloying contents verification and statistical analyse.
Inclusions inspection	Verification of the test heats purity.

Table 2.2.: Fundamental material characterization.

Mechanical material characterization	
Hardness	Reveal the uniformity of the QaT processing, the penetration depth as function of the applied ACR intensity as well as TM - processing efficiency both, the increasing hardness and ACR intensity.
Tension testing	Reveal the stress - strain response as a function of the applied treatment. Macro scale experiments to reveal the mechanical properties of the tube as whole; Micro scale experiments to reveal the local mechanical properties across the tube wall;
Charpy impact testing	Reveal the toughness response as a function of the applied treatment. Macro scale experiments to reveal the toughness properties of the tube wall as whole; Micro scale experiments to reveal the local toughness properties at different positions across the wall;
Fracture surface inspection	Reveal the fracture properties of tubes after various processing treatments to evaluate the influence of the exhibited gradients.

Table 2.3.: Mechanical material characterization.

Residual stress characterization	
Synchrotron measurements	Reveal the local and position resolved triaxial residual strains and stresses of straight and bent tubes as a function of applied ACR intensity.
Drilling hole method	Reveal the local axial and tangential residual stresses on the tube surface down to 1.5 mm tube drill depth and to validate the synchrotron data.
Contour method	Qualitative analyses of residual stress state, finite element analysis of the non - uniform displacement of the gap formed during the tube cutting.
X - ray diffraction	Reveal the residual stresses by layer remove method at the tube surface.

Table 2.4.: Residual stress characterization.

Metallographic and microscopic material characterization	
LOM	Reveal the local and position resolved triaxial residual strains and stresses of straight and bent tubes as a function of applied ACR intensity.
LEXT	Reveal the microstructure by digital 3D laser scanning microscopy.
SEM	Scanning electron microscopy to evaluate grain morphology and energy dispersive X - ray analysis to reveal chemical gradients.
TEM	Electron diffraction analyses of tube microstructure, especially grain morphology, as well as high angle annular dark field TEM examination of precipitates.

Table 2.5.: Metallographic and microscopic material characterization.

X - ray diffraction material characterization	
$\Theta/2\Theta$	Reveal the phase distribution position - resolved across the tube wall.

Table 2.6.: X - ray diffraction material characterization.

Weldability characterization	
MAG welding	Reveal the weldability and the weld - application - performance of the investigated tubes.

Table 2.7.: Weldability characterization.

2.1. Residual stress behaviour as function of ACR intensity

X - ray diffraction data [98] obtained from synchrotron experiments using conical slit cell allowed to determine lattice parameters across the tube wall position - resolved with a resolution of 0.8 mm for bcc ferritic phase (figures A.4 and A.5). The data were used to quantify axial, tangential and radial residual stress distributions across tube walls cooled down using various cooling conditions (table 1.6) in order to evaluate the relationship between ACR and the stress profiles. The diffraction data revealed that the tubes differed also in microstructure as revealed by varying diffraction peak broadening (figure 1.22) and Debye - Scherrer ring azimuthal morphology. The limitation of the performed experiments was given by the provided conical slit cell, which only supported the diffraction rings of bcc phase. The Moessbauer spectroscopy examinations on the tubes characterized using synchrotron diffraction indicated that the amount of fcc austenite phase is under the detection limit of 0.5 % (figure 1.28). The influence of martensite on the stress state was not evaluated at this stage but is planned in the future using an upgraded conical slit developed for the tube subject area in order to assess the stress state in fcc and bcc phases simultaneously within one experiment (figure 1.24).

As an important validation of the synchrotron data, the drilling hole method was applied to determine axial and tangential stresses in the tube surface region down to the depth of 1.5 mm. The results (figure C.7) from the drilling hole method mirrored the stress dependencies, especially the ratios between tangential and axial stresses, obtained from the synchrotron experiments though there was a relatively small shift caused by the boundary conditions.

The residual stress data collected from tubes produced using different cooling conditions indicated the enormous importance of the cooling process control during the thermo - mechanical rolling (figure A.5). Axial, tangential and radial tensile stresses up to 120 MPa were observed on both wall sides in as rolled as well as moderately cooled tubes. Such stress levels may result in the limitation of the tube

lifetime during cyclic mechanical loading because superimposed external stresses can promote fatigue crack growth and result even in macroscopic fracture. The tubes produced under high ACR's, however, revealed a shift of the tensile axial, tangential and radial residual stresses to the neutral respectively to the compression state. These observations allow drawing the conclusions, that (i) the surface cooling process can effectively decrease the tensile triaxial residual stresses and induce even the reversal of the stress state to compression, (ii) the mechanical properties can be improved by tuning the ACR intensity and (iii) the static and dynamic load capacity of the tube can be increased. By selecting dedicated cooling conditions, not only the microstructure (figure 1.3) but also the residual stresses in TM - tubes can be tuned effectively.

Complementary to the residual stress experiments on straight tubes [95], also the whole procedure was applied to bent tubes and mirrored the same results. An azimuthal distribution of stresses in bent tubes was a superposition of the intrinsic stresses formed after the cooling and the stresses formed during bending (figure C.5a).

2.2. Microstructure- and phase gradients as function of ACR intensity

One of the main aims of this thesis was to understand the influence of thermo - mechanical treatment on the functional tube properties which change as a result of varying microstructure and residual stress state. The motivation was to characterize microstructures of tubes produced using various ACR intensities and evaluate the correlation to macroscopic tube toughness, ultimate tensile strength and resistance to fatigue. One of the novelty of this thesis is that not only average microstructural and mechanical data were considered, but also the variation of the properties across the tube walls was evaluated.

Beside classical metallographic methods, advanced analytical techniques to investigate the microstructural properties were applied like TEM, SEM and LEXT as well as laboratory and synchrotron X - ray diffraction and the Moessbauer spectroscopy [96]. This pool of investigations was necessary to reveal the tube wall gradients (figures 1.23, 1.3 and 1.25) produced as a result of the TM - treatment during tube rolling.

The produced ultra - fine grained steel tubes extravagate the resolution of the light microscopy and afforded the use of the laser scanning digital microscopy as

well as electron microscopy. Also the scanning electron microscopy was not effective to distinguish between different bcc phases like ferrite, acicular ferrite and bainite as well as upper and lower bainitic phases. The transmission electron microscopy was sufficient enough to reveal the local microstructure but at the nanometer scale. In figures 2.1 to 2.6, exemplary HAADF and TEM records, respectively, taken next to the outer tube surface, are presented. The records are illustrated for the S890 QL_1 tube in figures 2.3 and 2.4 and for the TM - tubes, manufactured from TH 02 in figures 2.1 and 2.2 as well as for TH 04 in figures 2.5 and 2.6.

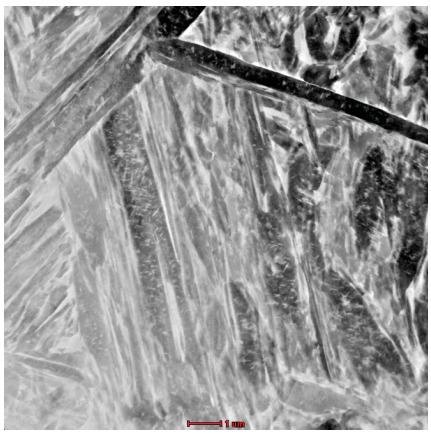

Figure 2.1.: HAADF record of tube T4 / TH 02 / ACR 30 °C/sec.

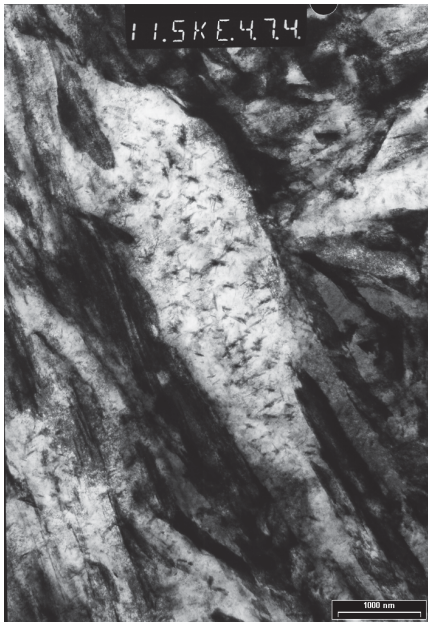

Figure 2.2.: TEM record of tube T4 / TH 02 / ACR 30 °C/sec.

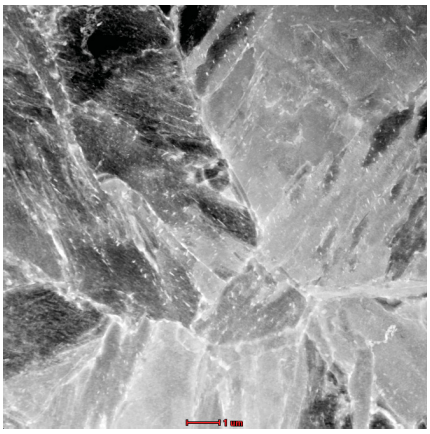

Figure 2.3.: HAADF record of tube T5 / S890 QL_1.

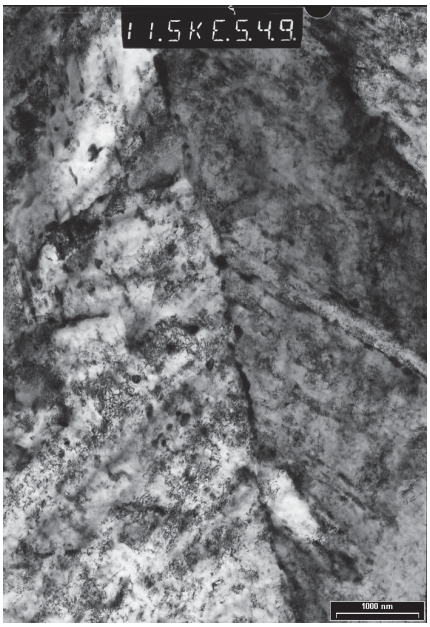

Figure 2.4.: TEM record of tube T5 / S890 QL_1.

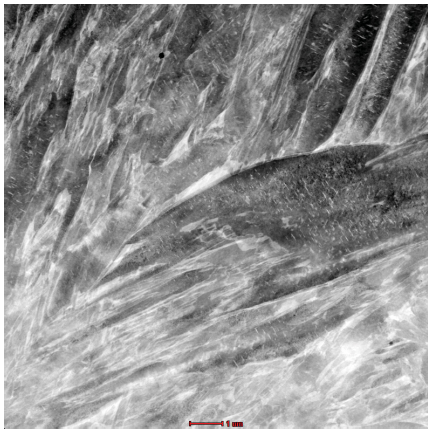

Figure 2.5.: HAADF record of tube T9 / TH 04 / ACR 30 °C/sec.

Figure 2.6.: TEM record of tube T9 / TH 04 / ACR 30 °C/sec.

The results from TH 02 tube T4 exhibit predominantly carbide-free [82, 84, 91] upper bainite (figure 2.1) and rarely spotted lower bainite (figure 2.2). The distribution of fine laths is homogeneous also containing a high dislocation density. At the lath boundaries martensite and / or retained austenite, which is locally rough, could be observed. Also sparely areas of lath shaped tempered martensite was located with M3C.

The reference tube S890 QL_1 consist to 100 % of tempered martensite as presented in figure 2.4. The grain and lath boundaries as well as the lath itself allocated high quantities of carbides (figure 2.3) and further a high dislocation density.

The intensively cooled tube TH 04 tube T9 indicates predominantly bainite (figure 2.6). The distribution between upper and lower bainite is homogeneous and further very high dislocation density as well as very fine uniform distributed laths with several exhibited ultra - fine precipitations are observable in figure 2.5. The lath boundaries are spotty clogged with a thin film [82] of martensite and / or retained austenite. Also very rarely tempered martensite was observed, shaped as laths with M3C.

The microstructure characterizations revealed that the well - known tempered martensitic properties of the quenched and tempered high strength tube are considerably over - matched by the TM - tubes. Also the effect (table 1.5) of changed or added alloying contents (tables 1.3 and 1.4) between TH 02 and TH 04 was visualized by these investigations. The comparison between the two test heats under intensively cooling conditions reveal, that the predominantly phase the bainitic microstructures exists.

The fcc phase quantity at the cross sections of the TM - tubes is for TH 02 around 10.0 to 15.0 % and for TH 04 7.0 to 9.0 %. The results of the investigated tubes surrendered, that the fraction of the retained austenite decreases while the applied spray water cooling was increased up to 25 % of the origin amount. These effects were qualitatively observed in the investigated TEM lamellae and quantitatively confirmed with the Moessbauer spectroscopy measurements as well as qualitatively with the X - ray diffraction $\Theta/2\Theta$ investigations (figure E.4).

Base on the cross - sectional microstructure analysis discussed above, it is further possible to discuss the lifetime performance of the tubes with the observed microstructures. The tempered fine grained martensitic structure of the QaT tube was distinctly overhauled by predominate bainitic microstructure [93], due to reduced residual stress states and increased toughness and UTS. Therefore the forecast of the lifetime performance will be assessed, based on these investigations. The TH 02 displayed carbide - free upper bainite and rarely lower bainite. The upper bainite consists of more retained austenite [91, 92] witch induces a decrease of the toughness. The homogeneous among of upper and lower bainite, as well as the decreased volume fraction of the retained austenite in TH 04, will definitely enhance the toughness [78], down to low temperatures as well as fatigue resistance. The thin films observed at the lath boundaries in TH 04 (figure 2.6) operates like a lubrication film [90, 83, 92] between the ferrite laths and promote better forming behaviour than the

martensitic, tempered martensitic and/or retained austenitic phases. These lath lubrication films were predominantly located in the TH 04 tube specimens. For cyclic loading and further fatigue [89, 81, 80], bainite is famous for the ability to reduce or eliminate stress peaks, induced by outer or inner notches and or cracks and effect in comparison to quenched and tempered [79, 85] tubes at identically strength levels superior resistance.

2.3. Transition behaviour of developed alloying concepts

The transition behaviour of the quenched and tempered tubes were completely analysed and standardized [94, 87]. In the present work, the Moessbauer and TEM analysis showed that the transition behaviour of S890 QL_1 results in the formation of 100 % tempered martensite. The mechanical testing of these tubes indicated this observation. The thermo - mechanically treatment in combination with the accelerated cooling after the last forming operation (table 1.2) induces a formation of gradient layers of phases over the tube cross section in dependence to the applied cooling intensity (figure 1.3). The identification of these gradients will be briefly discussed in the summary of the mechanical behaviour characterization. The transition behaviour of the TM - tubes was investigated by using three different methods. A pre - calculation to assess the influence of individual alloying elements and further the prediction of the phase transitions as well as the achievable mechanical values were performed with the software package JMAT - PRO (figure 1.31 TH 02 and figure 1.32 TH 04). The best matches obtained with this tool under the focus of weldability and ultra - high strength properties were then utilized in the cooperation with the pre - material supplier. After the tube manufacturing, the tubes transition characteristics were investigated by using a Gleeble (figure 1.34) device as well as a dilatometer device TA. The individual results are compared in table 2.8 for TH 02 and in table 2.9 for TH 04, under the focus of an ASTM E112 grain size 10 valid for all samples and calculations.

	JMAT - Pro	**Gleeble**	**TAD**
AT	865 °C	860 °C	870 °C
MST	340 °C	360 °C	360 °C
BST	350 °C / 15 sec	360 °C / 30 sec	345 °C / 10 sec
FST	500 °C / 250 sec	⊠	⊠
PST	550 °C / 400 sec	⊠	⊠

Table 2.8.: Dilatometer data comparison for TH 02.

	JMAT - Pro	Gleeble	TAD
AT	877 °C	880 °C	880 °C
MST	345 °C	360 °C	355 °C
BST	355 °C / 150 sec	370 °C / 45 sec	350 °C / 40 sec
FST	560 °C / 10000 sec	⊠	⊠
PST	520 °C / 1000 sec	⊠	⊠

Table 2.9.: Dilatometer data comparison for TH 04.

The pre - calculated values from JMAT - PRO compared to the experimental data from the Gleeble and device from TAD exhibit a certain degree of divergence. The area of expected temperatures for the AT, MST and BST correlates, but the scheduled times are mostly fare away from the experimental investigated values. The main discrepancies of the JMAT data are observed for the ferritic and perlitic phases, due to unavailability. So in the post experimental investigations these aspects were validated by new samples with varying grain sizes. The perlitic phase is strictly absent in the specimens of TH 02 as well as of TH 04 (figure 1.35), but the ferritic phase was found after a cooling time from 800 °C to 500 °C of 18000 sec and decreased ASTM E112 grain size in the area of 7. So this deviation from the pre - calculated transition behaviour compared to the analysed values in the case of used alloying concepts (table 1.3) is not satisfactory. The experimental and calculated values are in agreement and for both methods positively to verify. Evaluating the occurrence of the bainitic phase, none of the methods allowed distinguishing (figure 1.34) between the upper and lower bainitic fraction.

2.4. Macro mechanical behaviour characterization

Residual stress, microstructural and phase gradients formed across tube walls of thermo - mechanically treated tubes influenced decisively tube functional properties. To reveal the overall dependence of the mechanical properties on the gradients, very extensive macroscopic characterization of the tubes was performed.

The tubes overall macroscopic properties were analysed by cross - sectional tension tests - specimen geometry (lxbxh): 320.0 mm x 25.0 mm x 10.0 mm, Charpy impact tests - specimen geometry(lxbxh): 55.0 mm x 10.0 mm x 7.0 mm and hardness profile measurements across the tubes cross section. The revealed properties displayed

significant enhancement of the mechanical characteristics which correlated well with the increasing spray water intensities. The QaT treatment resulted in a more or less uniform cross - section (figure 1.6a). The inspections of the fractured specimens visualized these gradients (i) in the case of tension tests by changing crack (figure 1.12) path directions in accordance to the applied ACR intensity gradient, and (ii) in the case of the Charpy tests by changing the fraction of the areas of cleavage fracture versus the shear fracture (table 1.7) as a result of the ACR intensity gradient. The V - notched specimen fracture surfaces (for RT investigations figures 1.5 and 1.6) exhibited different thickness of the shear lips on the tube surfaces, so the smaller specimen shear lip is orientated to the tubes inner wall side and the larger one to the tubes outer surface. Consequently, this different appearance of the shear lips thickness is also an effective tool to visualize the depth of the penetration of the applied spray water cooling. In the case of the QaT tube, uniform shear lips as well as the smallest area of cleavage fracture were observed, although the specimens exhibited the minor strength. The hardness tests also revealed (i) the increasing mechanical strength (figure 1.16) due to increasing ACR intensity as well as (ii) the penetration depth (table 1.10) of the water cooling. In QaT tube, a nearly constant hardness profile across the tube wall indicated a uniform tempering treatment.

In order to draw conclusions from the macro investigations, tube wall thickness - averaged mechanical characteristics were evaluated which indicated the influence of the applied spray water cooling qualitatively without considering the structure - function gradients in detail. The analysis of the data indicated (i) the increase of the UTS, FS and toughness (tables 1.10, 1.7 and 1.9) in accordance to the increasing cooling intensity as well as (ii) the uniform behaviour of the QaT steel tube caused by the homogeneous tempering treatment after quenching. The stress - strain response of the QaT tubes exhibits a very pronounced yield point and small UTS in comparison with data from the other TM - tubes (figure 1.13). The stress - strain data documented that tensile loading of the QaT tube above the magnitude of the UTS limit will result in an abrupt fracture when the maximum yield stress is slightly exceeded, contrary to the TM - tubes, where the exceeding of the yield stresses resulted in a progressive material plastification due to the fine grained microstructure. For the TM - tubes, yield points (table 1.9, figures 1.12 and 1.13) are much less distinct and UTS increases gradually as a function of the increasing cooling intensity and transformed phases. Further, yield stresses and also other important functional parameters like toughness and fatigue [88] are expected to be improved and can be effectively tuned by the ACR intensity.

2.5. Micro mechanical behaviour characterization

In order to reveal tube functional gradients resulting from non - homogeneous temperature profile across the wall during the water spraying (table 1.2), the tube walls were split into several layers and miniaturized samples were fabricated for tension (figure 1.11) and Charpy impact tests (figure 1.7). These experiments revealed not only the gradients of the mechanical properties in QaT and TM - tubes but allowed also indirectly determining the gradients of ACR intensities and the effective penetration depth of the TM cooling. Accelerated cooling supports grain refinement and improves tube strength as well as toughness, as pre - assigned from the macroscopic mechanical behaviour characterizations. The applied spray water cooling penetration depth was qualitative indicated in the macroscopic examinations.

The tubes layer properties were analysed on micro - sized specimens by tension testing - specimen (figure 1.10) geometry (lxbxh): 22.0 mm x 1.0 mm x 1.0 mm and Charpy V - notched tests - specimen (figure 1.4) geometry (lxbxh): 3.0 mm x 4.0 mm x 27.0 mm. The first appointment of these micro - sized specimens was to find out the influence of the sample machining which was significant at the early stages. After optimizing the sample machining procedure, various testing devices were screened and validated. The extensive pre - examinations of the specimen machining as well as of the testing devices was necessary for the implementation of this advanced approach of the material local analysis. The output from the tests on miniaturized specimens correlated well with the results from other local techniques which also indicated tube gradual behaviour.

The results from the miniaturized specimens allowed to understand and to interpret the results from the macroscopic mechanical tests and to make the correlation especially to the material gradual microstructure [97]. Therefore, in order to interpret the data from the miniaturized specimens, the local mechanical characteristics were correlated with the penetration depth of the cooling, in accordance to the specific microstructural gradients. For the first time, the results opened the way to tune the functional parameters of TM - tubes by dedicated gradient design of mechanical properties and microstructure. Furthermore with this advanced treatment option and its understanding, it was possible to design tubes with extraordinary good mechanical properties compared to single phase tubes. The revealed microstructural layers are also in well accordance to the results of the X - ray diffraction gradient examinations. Some deviations of the results from the micro sized specimens out - valued to the macro sized specimens were found during the tension testing. This can be explained by a complex stress profile in the macro samples, as

revealed by the synchrotron experiments. So the tensile tests on the micro - sized specimens revealed actually intrinsic properties of the material, without the stress influence. This means that combined micro- and macro characterization can reveal the influence of residual stresses on the product functional behaviour.

2.6. Weldability and weld - application - performance characterization

The weldability was tested on tubes from TH 02 and TH 04, manufactured with ACRs of 30 °C/sec as well as S890 QL_1, to validate the weld - application - qualification. The qualification tests of the tubes were performed by MAG - welding with massive - wire as consumable (according to ISO 16834 - A) to reveal the influence (i) of the present microstructural gradients, (ii) in the weldment as well as (iii) in the HAZ. Pre - calculation of the tubes weld - behaviour based on the alloying concepts was not correctly assessed with conventional methods, due to the high levels of CC and CEW, so the experimental analysis was necessary. The main focus of the qualification was based on the heat conduction under multilayer - welding as well as the influence of segregation in both weldment and HAZ. The main boundaries of the (pre -)preparation for the full - depth weld as V - weld - seams are listed in table 2.10. TH 02 and S890 QL_1 were welded without and TH 04 was welded with tempering layers. This tempering layer effect was required due to the high CCs, which was further promoted by welding in flat position (PA) for the TH 04 tubes, with the exception that the root - layer was welded in horizontal position (PC) like the tubes of TH 02 and S890 QL_1.

Parameter	**Validity**	**Value**
Minimum preheating temperature	S890 QL_1	100 °C
Minimum preheating temperature	TH 02	150 °C
Minimum preheating temperature	TH 04	150 °C
Maximum interlayer temperature	ALL	180 °C
Heat input	S890 QL_1	6.0 - 10.0 kJ/cm
Heat input	TH 02	5.0 - 8.0 kJ/cm
Heat input	TH 04	5.0 - 8.0 kJ/cm

Table 2.10.: Welding investigations, parameter set-up and boundaries.

The investigation of the weldability and the weld - application - performance for UHSTMRT and QaT tubes revealed no significant differences in the case of the pool - crater as well as the arc - stability. Further all required specifications of mechanical properties like tensile, toughness and hardness as well as chemical properties for both, weldment and HAZ, were positively validated.

2.7. Outlook

The aim of this thesis was to analyse multi-scale properties of weldable ultra - high strength thermo - mechanically rolled seamless steel tubes. For this aim, the fundamental knowledge on the tubes behaviour under load conditions in context to the complex structure - function - relationship and the applied water cooling intensity was collected. In future, performance tests on welded structures, assembled in various engineering applications and tested under static and dynamic loads, will be performed.

This knowledge built - up, of static and dynamic cyclically loaded tubes in real applications will be the deliverables, in direct comparison to the actual available and used “state of the art” QaT - tubes. The activities documented in this thesis represent actually pre - investigations for this important task.

The importance of (i) the well - controlled thermo - mechanically tube manufacturing process, (ii) the understanding of the received structural and mechanical properties, (iii) the further processing like welding and (iv) the post - performance characterization under static and dynamic load conditions of components made of UHSTMRT, needs to be understood in order to open new possibilities for the construction design of various engineering applications. Finally, the overall mechanical performance, production efficiency and the mechanical stability under load conditions is the required further work which has to be done in cooperation with partners. So the next steps will be the characterization of the static and dynamic fatigue strength and the fracture - mechanic behaviour of UHSTMRT as well as of S890 QL_1, both in welded and un - welded condition. To quantify also the influence of welding, all tubes will be tested with tree types of weld - connection listed in table 2.11. The tubes for the tests are listed in table 2.12.

Weld - Type	Description
I	Circumferential welded with MAG
II	Weld pool protection and circumferential welded with MAG
III	Root welded with TIG and circumferential welded with MAG

Table 2.11.: Description of weld - types for further investigations.

Tube	Grade	ACR	QaT	Weld - Type
FT 1	TH 04	25°C/sec	-	-
FT 2	TH 04	25°C/sec	-	I
FT 3	TH 04	25°C/sec	-	II
FT 4	TH 04	25°C/sec	-	III
FT 5	S890 QL_1	-	✓	-
FT 6	S890 QL_1	-	✓	I
FT 7	S890 QL_1	-	✓	II
FT 8	S890 QL_1	-	✓	III

Table 2.12.: Specimen denotation for lifetime performance and fatigue characterization.

2.7.1. Static tension characterization by tension - testing:

The specimens are manufactured out of tube - wall - sections as whole (curved profile) in welded (Cross - weld specimen) and un - welded condition for the tubes 01 to 08 according to table 2.12.

2.7.2. Static toughness characterization by Charpy impact testing

The toughness of the tubes 01 to 08 are tested at - 40 °C on micro - sized specimens, whereby the welded tubes are investigated at different positions along the HAZ.

2.7.3. Fatigue behaviour characterization / S - N curve (Woehler curve)

The behaviour of notched and un - notched flat - specimens with origin tube surface (tube 01 and 05) are load - controlled tested at R = - 1 (tension - compression) and R = 0.1 (non - relaxing tension). The welded specimens (tubes 02, 03, 04, 06, 07 and 08) are tested vertically to the weld - seam on integral - flat - specimens.

2.7.4. Fracture behaviour characterization

For all tube specimens, all regions of cyclic loading like crack ignition as well as growth and failure behaviour are important results of the overall performance study

and hat to be investigated with all tubes listed in table 2.12 after all stages according to figure 2.7.

- Region I - Non - propagating fatigue cracks
- Region II - Stable fatigue crack propagation
- Region III - Unstable fatigue crack propagation failure behaviour

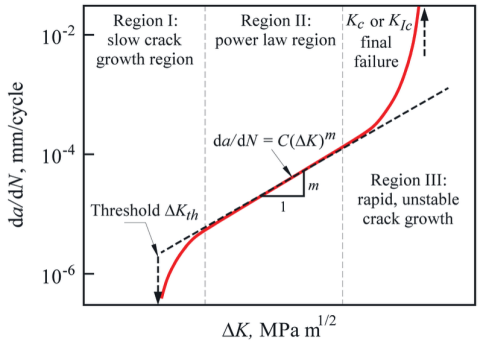

Figure 2.7.: Stages of fatigue - life-cycle characterization [86].

2.7.5. Characterization of insitu - transition behaviour of TH 04 by high energy synchrotron source

The developed alloying concept TH 04 was positive validated according to the requirements. The observed transition behaviour is not fully revealed in respect to the formation as well as to the exact formation path of the bainitic phases. This transition behaviour can be observed with an experimental insitu synchrotron study.

2.7.6. Characterization of the orientation of TM - treated tube walls, as function of applied ACR intensity

Position - resolved investigations revealed the complex phase- and microstructural gradients across the tube wall. Position - resolved XRD analysis indicated the presence of crystallographic texture gradients. To reveal this effect quantitatively and especially its dependence on the ACR intensity, extensive EBSD and / or X - ray pole - figure measurements will be performed.

[78] K Angamuthu, B Guha, and D.R.G Achar. Investigation of dynamic fracture toughness behaviour of strength mis-matched t steel weldments. *Engineering Fracture Mechanics*, 64(4):417 – 432, 1999.

[79] H. Beladi, I.B. Timokhina, X.Y. Xiong, and P.D. Hodgson. A novel thermo-mechanical approach to produce a fine ferrite and low-temperature bainitic composite microstructure. *Acta Materialia*, 61(19):7240 – 7250, 2013.

[80] Hossein Beladi, Ilana B Timokhina, and Peter D Hodgson. The formation of ultrafine ferrite and low temperature bainite through thermomechanical processing. In *Materials Science Forum*, volume 706, pages 2047–2052. Trans Tech Publ, 2012.

[81] D.V. Edmonds and R.C. Cochrane. Structure-property relationships in bainitic steels. *Metallurgical Transactions A*, 21(6):1527–1540, 1990.

[82] Robert William Kerr Honeycombe. *Steels: microstructure and properties: microstructure and properties.* Edward Arnold Ltd, 1981.

[83] Hajro Ismar, Zijah Burzic, Nenad Kapor, and Tugomir Kokelj. Experimental investigation of high-strength structural steel welds. *Strojniski vestnik - Journal of Mechanical Engineering*, 58(6), 2012.

[84] George Krauss and Steven W. Thompson. Ferritic microstructures in continuously cooled low- and ultralow-carbon steels. *ISIJ International*, 35(8):937–945, 1995.

[85] A. Lambert-Perlade, A.F. Gourgues, J. Besson, T. Sturel, and A. Pineau. Mechanisms and modeling of cleavage fracture in simulated haz microstructures of a high-strength low alloy steel. *Metallurgical and Materials Transactions A*, 35(13):1039–1053, 2004.

[86] Waldemar A Monteiro. Light metal alloys applications. 2014.

[87] P Nevasmaa, P Karjalainen-Roikonen, A Laukkanen, T Nykaenen, A Ameri, T Bjoerk, T Limnell, and J Kuoppala. Fracture characteristics of new ultra-high-strength steel with yield strengths 900–960 mpa. Technical report, Rautaruukki research Report, 2013.

[88] MJ Peet, P Hill, M Rawson, S Wood, and HKDH Bhadeshia. Fatigue of extremely fine bainite. *Materials Science and Technology*, 27(1):119–123, 2011.

[89] R.A. Ricks, P.R. Howell, and G.S. Barritte. The nature of acicular ferrite in hsla steel weld metals. *Journal of Materials Science*, 17(3):732–740, 1982.

[90] Kun Shi, Hong Hou, Jiang-Biao Chen, Ling-Ti Kong, Han-Qian Zhang, and Jin-Fu Li. Effect of bainitic packet size distribution on impact toughness and its scattering in the ductile and brittle transition temperature region of qandt mn-ni-mo bainitic steels. *steel research international*, 2015.

[91] Koh ichi Sugimoto, Tsutomu Iida, Jyunya Sakaguchi, and Takahiro Kashima. Retained austenite characteristics and tensile properties in a trip type bainitic sheet steel. *ISIJ International*, 40(9):902–908, 2000.

[92] Koh ichi Sugimoto, Kiyotaka Nakano, Sung-Moo Song, and Takahiro Kashima. Retained austenite characteristics and stretch-flangeability of high-strength low-alloy trip type bainitic sheet steels. *ISIJ International*, 42(4):450–455, 2002.

[93] Koh-ichi Sugimoto, Hikaru Tanino, and Junya Kobayashi. Impact toughness of medium-mn transformation-induced plasticity-aided steels. *steel research international*, 2015.

[94] Stahl Eisen Werkstoffblatt. Din sew 090-2 high tenacity quenched and tempered fine grain steel part 2: Technical delivery conditions for tube and hollow sections, 1993.

[95] Gerald Winter, Juergen Klarner, Bruno Buchmayr, and Jozef Keckes. Experimental characterization and modelling of residual stress gradients across straight and bent seamless steel tubes. *ESAFORM*, 2015.

[96] Gerald Winter, Juergen Klarner, Bruno Buchmayr, and Jozef Keckes. Macro- and microscopic properties of gradient ultra-high-strength seamless steel tubes produced by dedicated thermo-mechanical treatments. *IFHTSE*, 2015.

[97] Gerald Winter, Juergen Klarner, Jozef Keckes, and Bruno Buchmayr. Multi-scale and multi-method characterization of mechanical and microstructural. *XXXIV Verformungskundliches Kolloquium: ISBN 987-3-902078-20-9; pp. 203-209*, 2015.

[98] Gerald Winter, Mario Stefenelli, Juergen Klarner, Peter Staron, Torben Fischer, Jozef Keckes, and Bruno Buchmayr. Triaxial residual stresses in thermo-mechanically rolled seamless tubes characterized by high-energy synchrotron x-ray diffraction. *ASME PVP*, pages V003T03A020–V003T03A020, 2013.

3

List of Appended Publications

3.1. First Author Papers

Paper A
G. Winter, M. Stefenelli, J. Klarner, P. Staron, T. Fischer, J. Keckes and B. Buchmayr
Triaxial residual stresses in thermomechanically rolled seamless tubes characterized by high-energy synchrotron x-ray diffraction
American Society of Mechanical Engineers,
ASME PVP 2013 - Pressure Vessels and Piping Division (Publication)

Paper B
G. Winter, J.Klarner, J. Keckes and B. Buchmayr
Multi-scale and multi-method characterisation of mechanical and microstructural properties of graded thermo-mechanically rolled seamless steel tubes
XXXIV. Verformungskundliches Kolloquium (Publication)

Paper C
G. Winter, J. Klarner, P. Staron, B. Buchmayr and J. Keckes
Experimental characterization and modelling of residual stress gradients across straight and bent seamless steel tubes
ESAFORM 2015 - International Conference on Material Forming (Publication)

Paper D

G. Winter, J.Klarner, J. Keckes and B. Buchmayr

Macro- and microscopic properties of gradient ultra-high-strength seamless steel tubes produced by dedicated thermo-mechanical treatments

IFHTSE 2015 - International Federation for Heat Treatment and Surface Engineering (Publication)

Submitted Article E

G. Winter, J. Klarner, B. Buchmayr and J. Keckes

Gradients of mechanical properties and microstructure across ultra-high-strength seamless steel tube

Walls: the influence of thermo-mechanical treatment

SRI 2015 - Steel research international (Article) SRI 2015

3.2. Contribution of the author to the papers

Table 3.1.: Contribution of the Author to the appended publications in percent.

Paper / Article	Conception and planning	Experiments	Analysis and interpretation	Manuscript preparation
A	80	70	80	80
B	100	100	80	80
C	100	100	80	80
D	100	100	80	80
E	100	100	80	80

A

Triaxial Residual Stresses in Thermomechanically Rolled Seamless Tubes Characterized by High-Energy Synchrotron X-ray Diffraction

Gerald Winter[a], Mario Stefenelli[b], Jürgen Klarner[a], Peter Staron[c], Torben Fischer[c], Jozef Keckes[d], Bruno Buchmayr[e]

[a]voestalpine Tubulars GmbH & Co KG, Department R&D, Kindberg, Austria

[b]Materials Center Leoben Forschung GmbH

[c]Helmholtz-Zentrum Geesthacht, Center for Materials and Coastal Research, Institute of Materials Research, Geesthacht, Germany

[d]Department Materials Physics, Montanuniversität Leoben and Erich Schmid Institute, Austrian Academy of Sciences, Leoben Austria

[e]Department Product Engineering, Chair of Metal Forming, Montanuniversität Leoben Austria

Abstract

Residual stresses in seamless steel tubes have a significant influence on the mechanical stability and reliability of industrial constructions. In this contribution, triaxial residual stresses in seamless rolled tubes with an outer diameter of 82 mm and a wall thickness of 9.8 mm were analysed at synchrotron source PETRA III at DESY in Hamburg using the HZG beamline HEMS (P07) with a photon energy of 75 keV. The position-resolved measurements were performed using a conical-slit measurement technique with a spatial resolution in the direction of the X-ray beam of 0.8 mm. The tubes were produced under dedicated thermal conditions resulting in complex microstructure and residual stress profiles across the tube walls. The (experimental) measurements allowed determining axial, tangential and radial residual stress profiles. The results reveal tensile stresses up to 150 MPa on the outer

wall side and compressive stress of about −120 MPa on the inner wall side. The measurements document the importance of the cooling process control during the thermo-mechanical rolling, which represents a key factor for the design of dedicated microstructure and residual stress levels in the tubes.

A.1. Introduction

Non-destructive residual stress characterization in steel components at large penetration depths is a challenging task and can be nowadays performed using neutron diffraction and high-energy synchrotron X-ray diffraction [100]. The advantage of synchrotron X-rays with energies in the range of 50-300 keV is the high beam intensity enabling relatively fast measurements and in comparison with the neutron diffraction, better spatial resolution down to µm-range [106]. The possibility of fast measurements combined with a relatively small probe volume can be used for the characterization of large two and three-dimensional strain maps at depths down to a few cm.

The X-ray diffraction analysis of macroscopic residual stress fields is usually performed in two steps [102]. At first, lattice spacings $d^{hkl}(x,y,z)$ of hkl crystallographic planes are determined at different orientations of the diffraction vector Q and sample positions (x,y,z). Additionally, small pieces of the reference material (with relaxed macroscopic stresses) with the size of about $1 \times 1 \times 1\,\mathrm{mm}^3$ are measured using the same set up in order to determine unstressed lattice parameter d_0^{hkl} [102]. The X-ray elastic strain $\varepsilon^{hkl}(x,y,z)$ can then be evaluated according to

$$\varepsilon^{hkl}(x,y,z) = \frac{d^{hkl}(x,y,z) - d_0^{hkl}}{d_0^{hkl}} \tag{A.1}$$

As a second step, experimentally determined X-ray elastic strains $\varepsilon^{hkl}(x,y,z)$ are used to evaluate spatial distribution of triaxial residual stresses $\sigma_i(x,y,z)$ applying X-ray elastic constants E^{hkl} and ν^{hkl} of the material as follows [102].

$$\sigma_i(x,y,z) = \frac{E^{hkl}}{(1+\upsilon^{hkl})}\left(\varepsilon_i^{hkl}(x,y,z) + \frac{\upsilon^{hkl}}{(1-2\upsilon^{hkl})}\left(\varepsilon_A^{hkl} + \varepsilon_R^{hkl} + \varepsilon_T^{hkl}\right)\right) \tag{A.2}$$

Using the dedicated selection of the measurements directions, the stresses as well as the strains can be determined for radial (R), axial (A) and tangential (T) sample directions.

E^{hkl} and ν^{hkl} represent the elastic properties of the material and depend on the

single crystal elastic constants of crystallites, crystallographic texture and grain interaction model.

The characterization of residual stress spatial distribution $\sigma_i(x, y, z)$ in bulk materials is still not trivial task, because the diffraction signal may originate from a relatively large sample volume. In the case of neutron diffraction, which works with the resolution down to $1 \times 1 \times 1\,\mathrm{mm}^3$, the gouge volume is usually defined by primary and secondary selection slits. In the case of X-ray diffraction analysis operating with smaller gauge volumes, the better spatial resolution can be achieved by using more advanced optical components. Recently, a conical slit cell (CSC) was proposed (Fig. A.1a) to perform spatial resolved characterization of X-ray elastic strain in all directions $\varepsilon^{hkl}(x, y, z)$ [104].The system is based on several concentric slits that are focused on a spot within the sample by their conical shape (Fig. A.1b). The analysis of full diffraction rings enables the simultaneous determination of all strain components in the plane. Moreover, also basic information on the texture of the material can be obtained. To achieve depth resolutions well below 1.0 mm, the slit width as well as the beam cross-section has to be around 20 µm [104]; moreover, the depth resolution in x-direction also depends on the energy resolution given by the monochromator. Thus, a third-generation synchrotron source with high brilliance is required for the use of a CSC. So far, only few examples for the application of CSC for residual stress and texture analysis can be found in the literature [103]. A CSC produced by Institute für Mikromechanik Mainz is used for residual stress analysis at the HZG beamline HEMS at the PETRA III synchrotron source at DESY in Hamburg. While depth resolutions of a few 100 µm can be achieved with narrow beams, the grain size of the studied material often prevents a conventional analysis of diffraction rings with such high resolutions; however, strategies for improving grain statistics can often be applied in such cases. In many cases, only moderate depth resolutions are required, and with a larger beam cross-section, the grain statistics can be improved.

In this contribution, spatial distribution of triaxial residual stresses across the wall of a thermo-mechanically treated seamless steel tube was characterized. The concept of thermo-mechanical treatment enables a control of microstructure in seamless steel tubes and allows the optimization of mechanical properties like high strength combined with excellent toughness and weldability. Conventional quenching and tempering in heating furnace and quenching device are substituted by the accelerated spray water cooling applied directly after the stretch reducing mill [101]. During the cooling, it is expected that complex residual stress and microstructure gradients connected with the formation of martensite are formed across the tube wall.

The aim of this work was to perform a position-resolved characterization of residual stresses across the walls of three tubes and evaluate the magnitude of radial, axial and tangential residual stress components in ferrite as a function of thermal treatment.

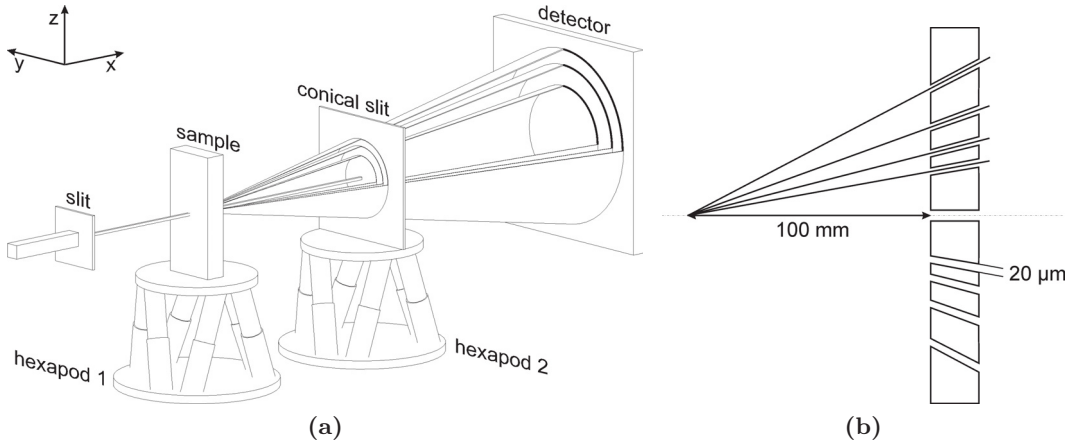

Figure A.1.: A schematic experimental setup using a conical slit cell which allows selecting a small sample volume (a) and a detail of the conical slit cell providing the spatial resolution of 0.8 mm (b).

A.2. Experiment

Thermo-mechanically treated seamless steel tubes are produced in a few steps. The piercing of a round solid billet is the first forming operation to make a seamless tube, also known as the Mannesmann piercing procedure [105]. Two barrel-type rolls rotate in the same direction to feed the billet forward to the plug which is free to rotate. The rolling gap in the horizontal is closed by two Diescher discs. The push bench is the second forming device in the production for the elongation of the material using an internal tool. The mandrel bar pushes the pierced billet through several non-driven roller stands to produce the so-called pipe shell. In the reheating furnace the cold pipe shells get their required temperature for the last forming step the stretch-reducing mill. The heated pipe shells is stretched to achieve the final geometry by several driven roller stands. Directly after rolling, the tube surface is cooled down by spray water at high cooling rate to fix the ultrafine grained microstructure [99]. With respect to the achieved heat transfer and the tube cross-section, the tube consists of different microstructure layers. For high wall thickness tube surface section is martensitic followed by bainitic and ferritic/perlitic layer.

In this work, residual stresses in three types of seamless tubes were characterized.

The tubes denoted further as A, B and C distinct by the cooling intensity and consequent microstructure gradient across their walls. Tube A was not water sprayed, tube B was moderately water sprayed and tube C was intensively cooled down after the stretch reducing mill. As a result of the different cooling rates, the tubes B and C exhibited an increased amount of martensite and bainite (Fig. A.2).

The A, B and C tubes were characterized at the HZG beamline HEMS (P07) at the PETRA III synchrotron source in Hamburg. For the experiment, the X-ray energy of 77.5 keV was used. The cross section of the X-ray beam was $50 \times 50\,\mu m$ and the depth resolution was about 0.8 mm. The grain size of the material was small enough to yield homogeneous diffraction rings with this gauge volume.

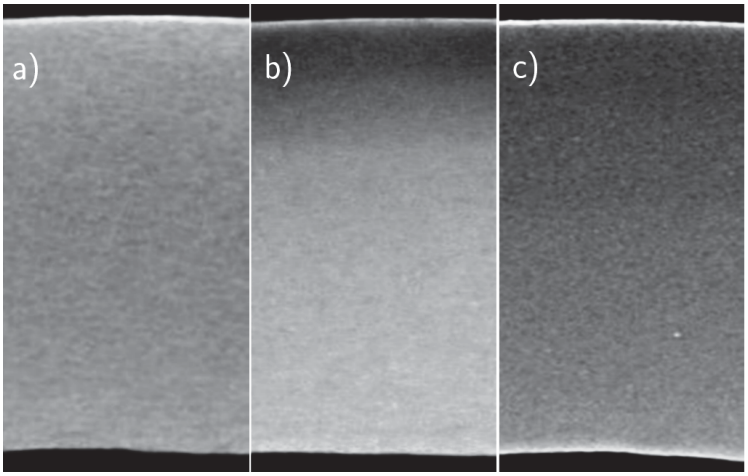

Figure A.2.: Microstructure (from outside to inside) across the tube walls A (a), B (b), C (c).

Strain measurements were carried out in two steps. At first the X-ray beam was oriented perpendicular to the tube axis and the tube wall was moved across the focus of the conical slits (Fig. A.1b) in x-direction with a step of 0.5 mm. Simultaneously Debye-Scherrer rings were collected using the 2D detector. In the next step, the beam was directed parallel to the tube axis and rings cut from tubes (with a thickness of 15 mm) were scanned along the x-axis. At the end the unstressed lattice parameter was determined by scanning small pieces of the tube material.

From the first set of measurements, $d^{hkl}(x)$ dependence as a function of x and the angle δ (*cf.* Fig. A.3) was determined using the Bragg's law. Axial and tangential strain components $\varepsilon_A^{hkl}(x)$ and $\varepsilon_T^{hkl}(x)$ were quantified from $d^{hkl}(x)$ values (obtained

for $\delta = 0$ and $\delta = 90$ degrees, respectively (Fig. A.3)) applying the unstressed lattice parameter d_o^{hkl} and Eq. (A.1). In a similar way tangential and radial strain components $\varepsilon_R^{hkl}(x)$ and $\varepsilon_T^{hkl}(x)$ were determined by analysing diffraction data in the geometry with the X-ray beam oriented parallel to the tube axis.

Both X-ray elastic strains $\varepsilon_i^{hkl}(x)$ as well as residual stresses $\sigma_i(x)$ were determined with an error of 10 %.

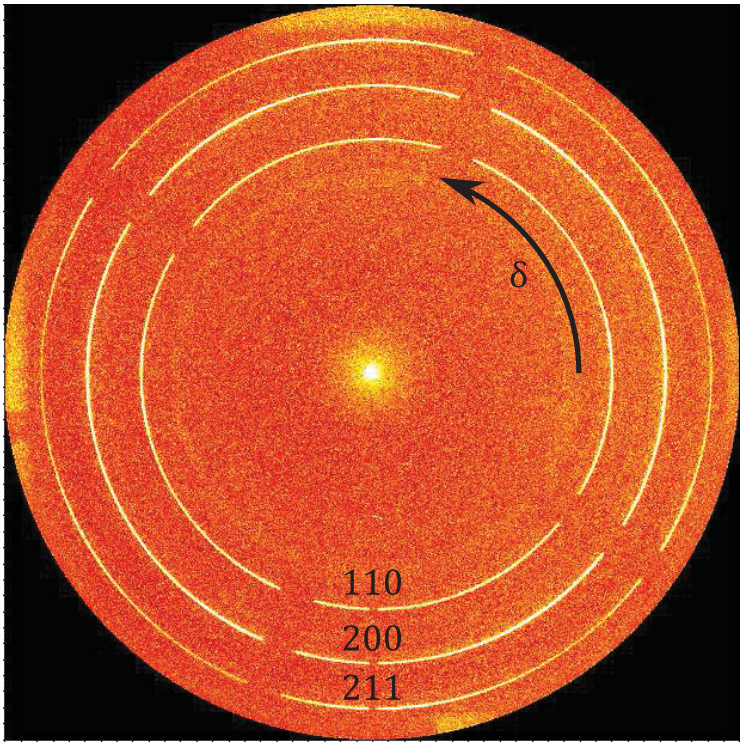

Figure A.3.: A representative X-ray diffraction pattern with ferrite 110, 200 and 211 Debye-Scherrer rings collected from a seamless steel tube using conical slits.

A.3. Results and Discussion

A representative X-ray diffraction pattern with typical Debye-Scherrer rings (collected from thermo-mechanically treated seamless steel tube B) is presented in Fig. A.3. One can identify 110, 200 and 211 diffraction rings originated from the ferrite phase. Similar patterns were collected from all three tubes and were used to evaluate distribution of X-ray strain $\varepsilon_i^{hkl}(x)$ across the walls.

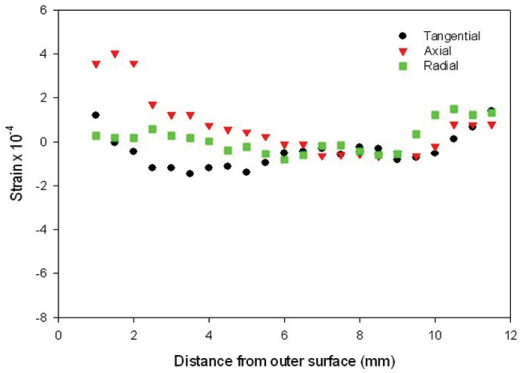

(a) Tube A

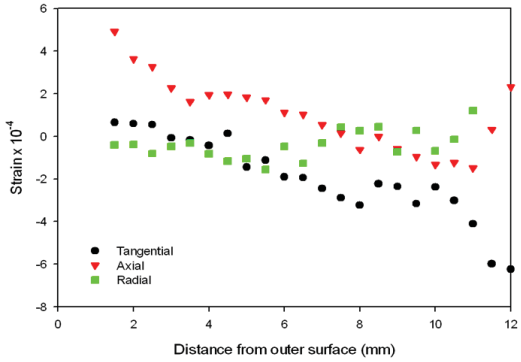

(b) Tube B

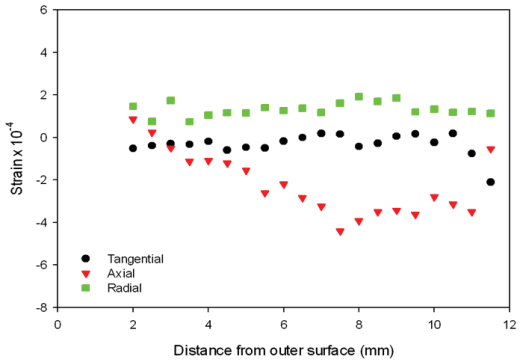

(c) Tube C

Figure A.4.: Distributions of axial, tangential and radial elastic strains (from outside to inside) across the walls of tube A (a), B (b), C (c).

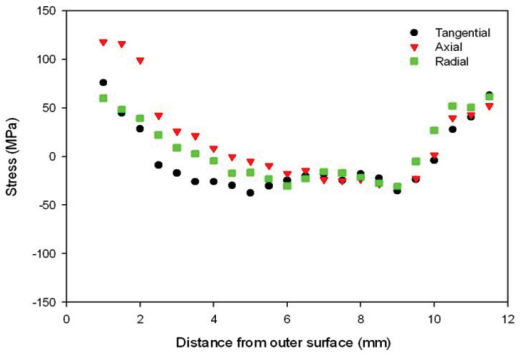

(a) Tube A

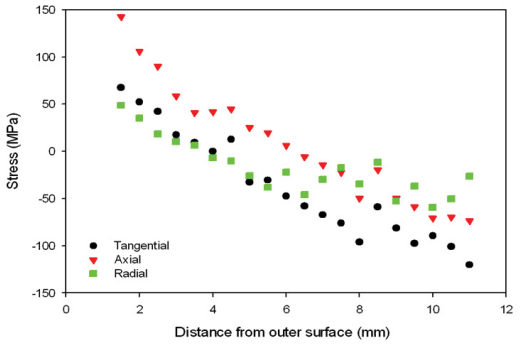

(b) Tube B

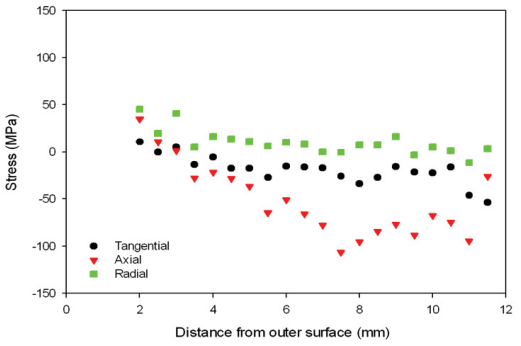

(c) Tube C

Figure A.5.: Distributions of axial, tangential and radial residual stresses (from outside to inside) across the walls of tube A (a), B (b), C (c).

In Fig. A.4, experimentally determined axial, tangential and radial X-ray elastic strain dependencies $\varepsilon_i^{hkl}(x)$ obtained from A, B and C tubes are presented. At this stage the results unambiguously demonstrate that the different cooling modes caused the formation of very specific strain profiles across the walls of A, B and C tubes.

The results from Fig. A.5 were used to quantify axial, tangential and radial residual stresses in ferrite using Eq. (A.2). Since the conical slits were aligned just for the ferrite reflections, the strains presented in Fig. A.4 represent the distortion in the ferrite crystallites and strains in the ferrite phase. The samples B and C differ in microstructure and phases because of different cooling intensity, the measured strains may differ from the tubes macroscopic strains. Due to above reasons, in order to evaluate stresses from the measured strains, ferrite X-ray elastic constants Young modulus of 225 GPa and Poisson number of 0.276 were applied for all three pipes. Similar as for strains, also in the case of residual stresses presented in Fig. A.5 very specific stress dependences $\sigma_i(x)$ can be observed.

In the tube A (produced without external cooling) one can observe relatively high axial, tangential and radial tensile stresses up to 120 MPa on both wall sides. This stress level may results in the limitation of the tube lifetime during cyclic mechanical loading because superimposed external stresses can promote the crack growth. In the wall centre low compressive stresses were detected.

In the tube B (produced using moderate water cooling), axial tensile stresses up to 150 MPa can be observed only on the outer wall side whereby the wall inner side is under compression.

In the tube C (produced using intensive water cooling), negligible residual stresses can be observed on the outer side and the inner side is under compression.

A.4. Conclusions

Methodologically, the results document that conical slit cell can be effectively used to evaluate the magnitude of X-ray elastic strains and macroscopic residual stresses in steel tubes with a spatial resolution of 0.8 mm.

The residual stress data collected from A, B and C tubes (cooled under different conditions) document the importance of the cooling process control during the thermo-mechanical rolling of steel tubes. The tensile stresses detected in the outer wall side can represent a serious problem in the tube performance. By selecting dedicated cooling conditions, not only the microstructure but also residual stresses in the tubes can be tuned effectively.

A.5. Acknowledgements

Financial support by the Austrian Federal Government (in particular from the Bundesministerium für Verkehr, Innovation und Technologie and the Bundesministerium für Wirtschaft, Familie und Jugend) and the Styrian Provincial Government represented by Österreichische Forschungsförderungs-gesellschaft mbH and by Steirische Wirtschaftsförderungs-gesellschaft mbH, within the research activities of the K2 Competence Centre on "Integrated Research in Materials, Processing and Product Engineering" operated by the Materials Center Leoben Forschung GmbH in the framework of the Austrian COMET Competence Centre Programme, is gratefully acknowledged.

This project was supported by "Die Österreichische Forschungsförderungsgesellschaft" FFG Basisprogram and project "2655990 UHSTMRT".

Portions of this research were carried out at the HZG beamline HEMS (P07) at the PETRA III synchrotron source at DESY in Hamburg, a member of the Helmholtz Association (HGF). We would like to thank Dr. Norbert Schell for assistance at the HZG beamline HEMS. We thank also to EU for the financial support to perform the experiment at DESY.

[99] B. Buchmayr and J. Klarner. Optimierung von prozessketten fuer rohrfoermige endprodukte. *Aachener Stahlkolloquium*, 28, 2013. cited By (since 1996)1.

[100] M.E Fitzpatrick. *Analysis of Residual Stress by Diffraction Using Neutron and Synchrotron Radiation*. Taylor and Francis, London and New York, 2003.

[101] J Klarner, B Buchmayr, and W Rainer. Toughtubes, extrem feinkoernige nahtlose stahlrohre. *BHM*, 156(5):168–174, 2011.

[102] J. B. Cohen. Klimanek, P.I. C. Noyan. Residual stress measurement by diffraction and interpretation. *Crystal Research and Technology*, 24(2), 1989.

[103] R.V. Martins, U. Lienert, L. Margulies, and A. Pyzalla. Determination of the radial crystallite microstrain distribution within an almg3 torsion sample using monochromatic synchrotron radiation. *Mat Sci Eng A*, 402(1-2):278–287, 2005.

[104] H.F. Poulsen, S. Garbe, T. Lorentzen, D.J. Jensen, F.W. Poulsen, N.H. Andersen, T. Frello, R. Feidenhans'l, and H. Graafsma. Applications of high-energy synchrotron radiation for structural studies of polycrystalline materials. *J Synchrotron Radiat*, 4(3):147–154, 1997. cited By (since 1996)95.

[105] R Pschera, J Klarner, and C Sommitsch. Finite elemente analyse der reibungsbedingungen beim schraegwalzen mit diescherscheiben. In *Proceedings Seminar Rohrherstellung und -verarbeitung*, pages 59–69. LUT, 2007.

[106] A. Pyzalla. Methods and feasibility of residual stress analysis by high-energy synchrotron radiation in transmission geometry using a white beam. *J Nondestruct Eval*, 19:21–32, 2000.

B

Multi-scale and multi-method characterization of mechanical and microstructural properties of graded thermo-mechanically rolled seamless steel tubes

Gerald Winter[a,d], Juergen Klarner[a], Jozef Keckes[c] and Bruno Buchmayr[d]

[a]voestalpine Tubulars GmbH & Co KG, Department R&D, Kindberg, Austria

[c]Department Materials Physics, University of Leoben, Austria

[d]Department Product Engineering, Chair of Metal Forming, University of Leoben, Austria

Abstract

Thermo-mechanical treatment of rolled seamless steel tubes results in the formation of pronounced gradients of phases, crystallite sizes, texture and residual stresses across the tube wall. Those gradients influence decisively functional properties and lifetime of tubes in service. In this contribution, multi-scale mechanical properties prepared by using varying thermo-mechanical treatments are characterized at two dimensional levels. At first the overall macroscopic properties were determined by testing the tubes as full wall section. Secondly, micro-sized sample were fabricated from the individual tube regions and mechanically tested. Complementary, residual stresses and microstructure across the tube wall were characterized using laboratory and synchrotron X-ray diffraction, Moessbauer spectroscopy and transmission electron microscopy. Using this multi-method and multi-scale approach it was possible to determine a whole set of parameters like phases, grain morphology, dislocation densities, residual stress profiles, tensile strength and fracture strains as well as

hardness profiles across the tube wall. Finally the data were correlated with the conditions applied during tube production in order to understand the formation of gradients as well as their influence on mechanical qualities.

Kurzfassung

Thermomechanisches Walzen von nahtlosen Stahlrohren bewirkt eine ausgeprägte Änderung der Phasen, Kristallgrößen, Textur und Eigenspannungen über die Rohrwand. Diese Gradienten beeinflussen signifikant die funktionalen Eigenschaften des Rohres und das Verhalten im Einsatz. In diesem Zusammenhang sind die mechanischen Eigenschaften von unterschiedlichen Varianten der thermomechanischen Rohrproduktion in zwei Größenskalen zu charakterisieren. Zuerst sind die makroskopischen Eigenschaften zu ermitteln wobei das Rohr als Streifenprobe geprüft wird. Im zweiten Schritt wurden die Untersuchungen mittels Kleinstproben an lokalen Stellen der Rohrwand entnommen und durchgeführt. Der Zusammenhang zwischen den Eigenspannungen und der Mikrostruktur, die sich über die Rohrwand abändern, sind mittels Synchrotron-Strahlung, Röntgenbeugung, Moessbauer-Spektroskopie und Durchstrahlungs-Mikroskopie zu ermitteln. Durch diese Multi-Methoden und Multi-Skalen Betrachtung der vorliegenden Eigenschaften besteht die Möglichkeit eine umfassende Beschreibung der Phasen, Strukturen, Versetzungsdichten, Eigenspannungsprofile und mechanischen Eigenschaften wie Streckgrenzen, Zugfestigkeiten, Dehnungen als auch Härteprofile über die Rohrwand zu erstellen. Als letzter Schritt sind die applizierten Produktionsbedingungen den ermittelten Eigenschaften der Rohre gegenüber zustellen, um die Ausbildung der Gradienten als auch die daraus resultierenden abgeänderten mechanischen Eigenschaften verstehen zu können.

Keywords

Steel tube, thermo-mechanical treatment, structure-property gradient

B.1. Introduction

Seamless steel tubes, used extensively in structural, mechanical and general engineering fields, have to fulfil a variety of mechanical and chemical requirements. The increasing demand for the production of light weight, high-strength and high-performance tubes requires an optimization of the intrinsic material properties, like ultimate tensile strength (UTS), fracture strain (FS) and fracture toughness (FT), as well as structural and design aspects [108].

The production of seamless steel tubes includes a series of sub-processes like billet heating, piercing, push bench processing, reheating, stretch reducing and spraywater cooling [111]. During the production, the variety of thermo-mechanical processing results in the formation of complex residual stress fields across the tube wall which further correlate with a complex gradual steel microstructure induced by the cooling conditions.

In the past, primarily mechanical but also other functional properties of tubes were characterized using characterization approaches which provided usually overall "volume-averaged" data like UTS and FS of the tube.

Since during the production of seamless steel tubes, the varying thermo-mechanical processing [107] conditions are applied, residual stresses and microstructure gradients result in the formation of complex gradients of mechanical properties.

Therefore, in order to understand the overall structure property relationship [109] of seamless steel tubes as gradient engineering components, it is necessary to understand the relationship between the local variation of (i) microstructure, (ii) residual stresses, (iii) phases (iv) mechanical properties across the tube wall and (v) actual production conditions used for product manufacturing.

The aim of this contribution is to perform multi-scale characterization of mechanical properties for seamless steel tubes by performing tensile tests on full section tube wall specimens and on small micro sized specimens fabricated from different regions across the wall. The mechanical data are correlated with the results from microstructural and residual stress characterization performed using a variety of advanced analytical techniques.

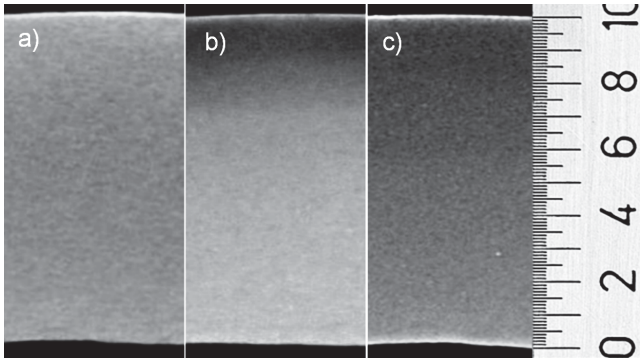

Figure B.1.: Gradient microstructures across the 10 mm thick tube walls A (a), B (b) and C (c) induced by the varying water cooling intensity. The darker region at the outer tube wall side in b) indicates the presence of martensite followed by bainite whereby in c) martensite is present across the whole cross-section.

B.2. Tube samples

Three types of seamless steel tubes analysed in this work will be further denoted as A, B and C contained besides iron following elements: C, Si, Mn, P, S, Cr, Ni, Cu, Al, Ti, V and Nb. The tubes differed in the applied cooling conditions whereby for A no cooling was used, for B a moderate cooling was used and for C an intensive cooling was used (Fig. B.1). The microstructure of tube A consists of homogeneous distributed ferrite and perlite, tube B and C exhibited an increased amount of martensite and bainite especially in the outer tube wall regions.

B.3. Experimental characterisation

B.3.1. Residual stress characterisation

Triaxial residual stress characterization was performed at P07 beamline of the PETRA III synchrotron source in Hamburg using the X-ray energy of 77.5 keV by applying a conical slit system (fig. B.2), as specified in our previous works [116].

During the measurement, the tubes were moved with a step of 0.5 mm along the beam direction and Debye-Scherrer rings were collected simultaneously using a two dimensional detector.

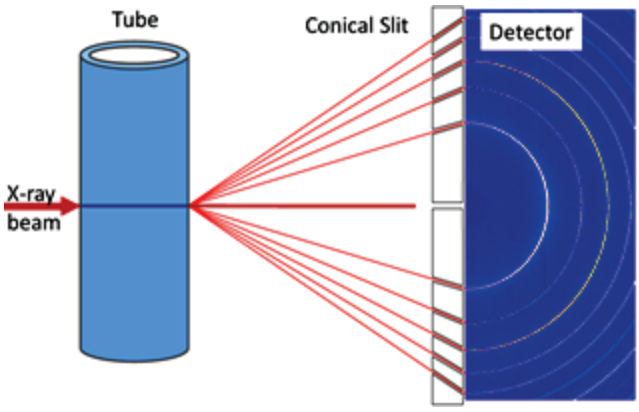

Figure B.2.: A schematic description of the scanning synchrotron experiment. The tube was moved along the X-ray beam and the gauge volume in tube wall was selected by the conical slit system. The Debye-Scherrer rings observed on the detector were used to quantify strain in the sample with a spartial resolution of 0.8 mm.

By moving the tubes, the focus of the dedicated conical slits also moved within tube wall and in this way the gauge volume as well as resolution were defined (Fig. B.2) [113, 110]. Diffraction data were used to evaluate lattice spacing as a function of the position x across tube wall from measured hkl reflections using Bragg's law [117, 118].

Additionally, small pieces of tube material were characterized position resolved using the same procedure in order to determine the distribution of unstressed lattice parameters across the wall. The results were used to calculate triaxial strains and, by applying Young modulus E of 225 GPa and Poisson number υ of 0.276, triaxial residual stress stresses were determined.

B.3.2. Moessbauer spectroscopy

57Fe Moessbauer spectra were measured in scattering geometry using a standard Moessbauer spectrometer in a constant acceleration mode with a 57Co(Rh) radioactive source [114]. The spectra were measured at room temperature. The relative contents of individual Fe-bearing phases were monitored through the corresponding spectral areas.

B.3.3. Electron microscopy

Microstructure [112] present in steel tube walls was investigated by standard scanning and transmission electron microscopy (SEM and TEM) using LYRA 3 FEG-SEMxFIB and JEM - 2100F systems, respectively.

B.3.4. X-Ray diffraction analysis

Scanning X-ray diffraction with an X-ray beam of 0.5 mm in diameter across tube walls of samples A, B and C was performed using Rigaku Smartlab system equipped with X-ray mirror, focusing optics and scintillation detector using Cu-K α radiation [115].

B.3.5. Mechanical tests

Vickers hardness HV 0.5 across tube wall was determined using Buehler Micromet 5104 system. Miniaturized tensile tests on samples of about 1 mm in thickness machined from different positions across tube walls were performed using Kammrath & Weiss system equipped with 5 kN load-sensor in strain-controlled mode.

B.4. Results and discussion

B.4.1. Residual stresses

Residual stress profiles across the wall of tubes A, B and C are presented in Fig. B.3. In tube A one can observe "relatively" high axial, tangential and radial tensile stresses up to 120 MPa on both wall sides.

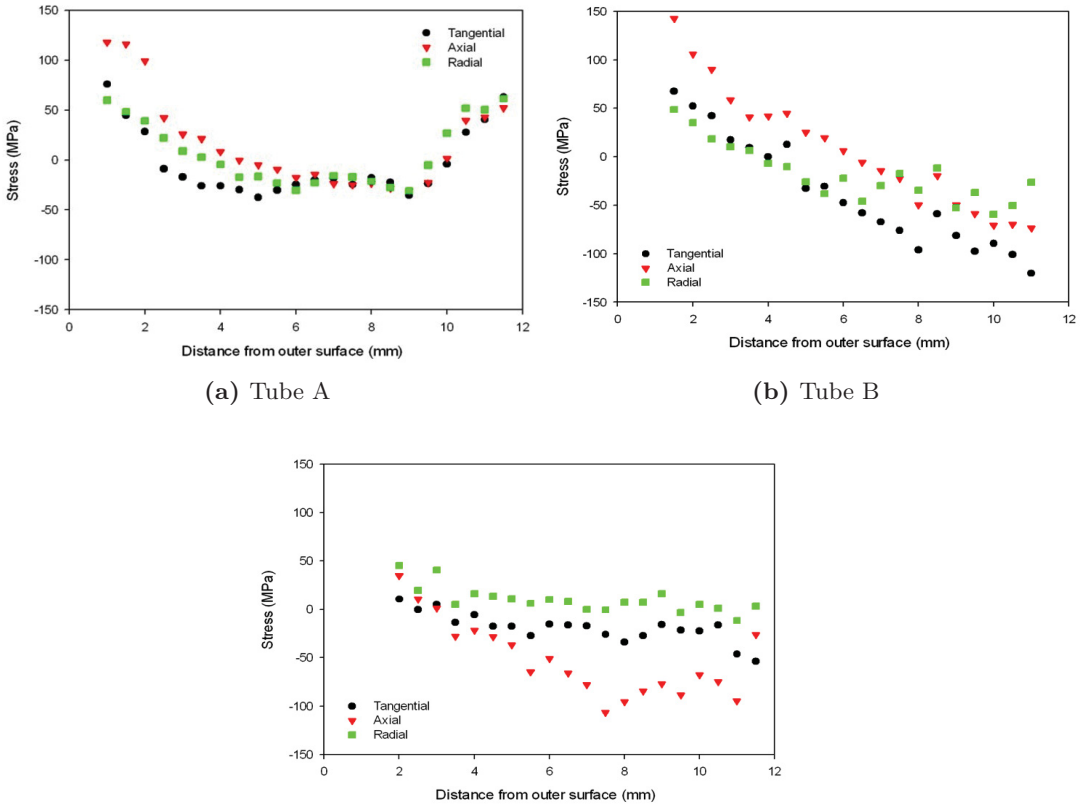

(a) Tube A

(b) Tube B

(c) Tube C

Figure B.3.: Distributions of axial, tangential and radial residual stresses (from outside to inside) across the walls of A (a), B (b), C (c) tubes. By increasing the cooling intensity from a) to c), the stress profile was adjusted.

In tube B, axial tensile stresses up to 150 MPa are detected only in outer wall side whereby wall inner side is under compression. In tube C, negligible residual stresses are observed on the outer side and the inner side is under compression. The development of the residual stresses across the walls of A, B and C tubes

correlates well with the applied cooling conditions and wall microstructure gradient (Fig. B.1). Increasing cooling intensity resulted in reduction of tensile stresses whereby the stresses in most intensively cooled tube C were practically zero or compressive (Fig. B.3). Therefore by applying dedicated thermo-mechanical treatment, magnitude and nature of residual stresses in tube wall were adjusted.

B.4.2. Hardness Profile

Results from hardness (HV 0.5) measurements across differently treated tube walls of A, B and C samples are presented in Fig. B.4. The uncooled and medium cooled samples A and B exhibit constant hardness of about 200 and 240 HV 0.5, respectively, whereas in the intensively cooled sample C a steep profile of the hardness with maximal value of 375 HV 0.5 was observed. These results infer that by adjusting the cooling intensity, the mechanical properties across tube wall can be effectively adjusted.

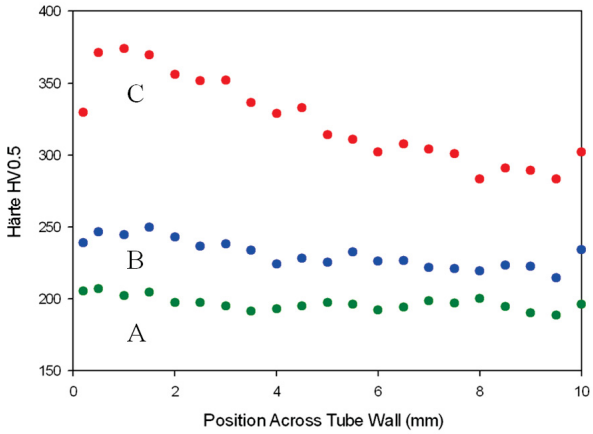

Figure B.4.: Micro-hardness distribution from outer to inner side of tube wall indicates the influence of varying cooling intensity on local mechanical properties of sample A, B and C.

B.4.3. Macro- and micro- tensile tests

Results from tensile tests from micro-samples machined from different regions of the tube walls are presented in Fig. B.5. The used micro tensile specimens exhibit a local gauging surface of 1 mm^3 (length x width x height [mm] 22 x 6 x 1). Similar as

the hardness data also the local stress-strain response indicates that varying cooling intensity resulted in strong gradients of mechanical properties across the tube walls.

In the uncooled sample (Fig. B.5, Fig. B.5a), UTS magnitude is relatively constant across the wall of about 700 MPa, similar as the hardness in Fig. B.4. In case of the fracture strain, one can observe a small variation whereby outer sample region shows the maximal value of about 40 %. In the sample B (Fig. B.5b), a variation of the UTS in the individual regions is obvious, whereby the maximal UTS was detected in the most intensively cooled outer tube region. The cooling effect can be clearly recognized in case of FS, where all FSs are smaller as in sample A (Fig. B.5a) and outer tube layer shows a relatively brittle response with FS=28 %.

In the case of sample C (Fig. B.5c), intensive cooling modified the mechanical properties across tube wall remarkably. Similar as in Fig. B.5b, the outer region exhibits the maximal UTS up to 1.35 GPa and relatively small FS of 20 %. With increasing distance of individual sample regions from outer tube wall, UTS decreases significantly, but remains still about the UTS values observed for samples A and B. Similar also FS behaviour of the relatively hard (Fig. B.5) tube C shows brittle response in comparison with the data from Fig. B.5a and B.5b.

An important observation as a function of the applied cooling intensity is the abrupt transition from elastic to plastic material response in A and B (Fig. B.5a, Fig. B.5b) diminishes in C (Fig. B.5c).

The stress-strain analysis of individual regions in tubes A, B and C documents that the mechanical properties of tube gradient material (cf. Fig. B.1) can be adjusted in a relatively large ranges, 650 - 1350 MPa for UTS and 0.19 – 0.39 for FS. These results demonstrate that cooling intensity may be used as an effective tool to engineer functional properties of seamless steel tubes.

Complementary to tensile tests on micro-sized specimens, also tensile tests on full wall section samples were performed as shown in Fig. B.6. For the UTS, values of 730, 840 and 1250 MPa, and for FS, values of 0.25, 0.20, and 0.15, were evaluated for A, B and C samples. Additionally, there was observed a significant increase in yield strength of 580, 670 and 1070 MPa for A, B and C.

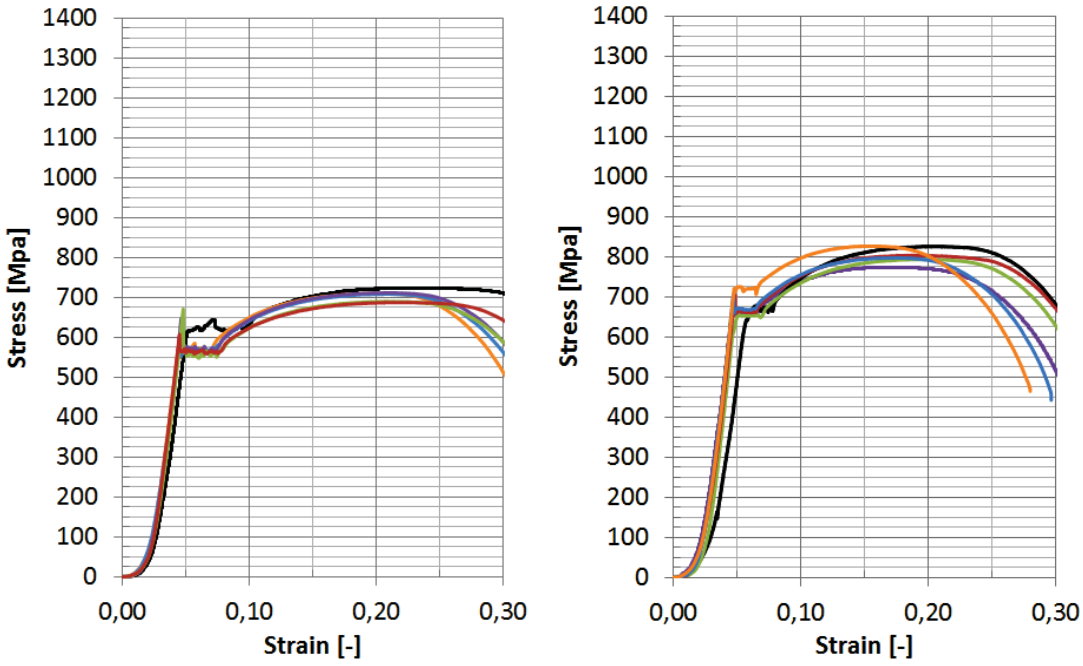

(a) Tube A

(b) Tube B

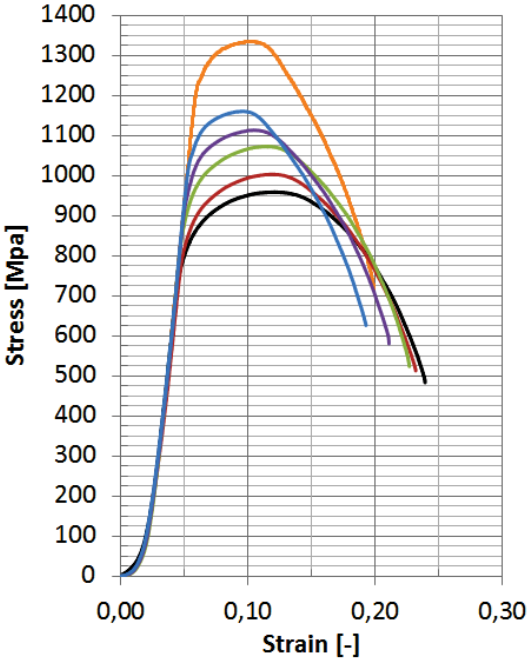

(c) Tube C

(d) Position from outer (orange) to inner (black) tube surface

Figure B.5.: Results from tensile tests on miniaturized specimens document the variation of mechanical properties across tube wall in A (a), B (b) and C (c).

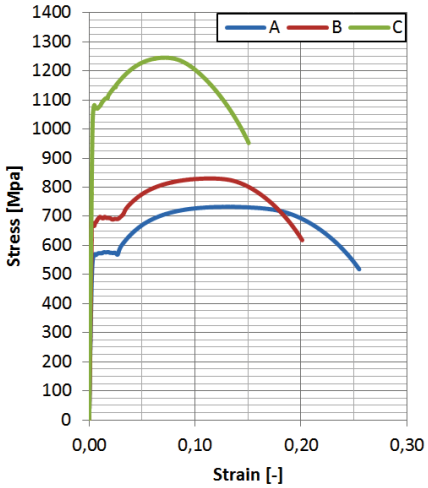

Figure B.6.: Results from tensile tests on full wall section specimens document the variation of mechanical properties across tube wall in A, B and C.

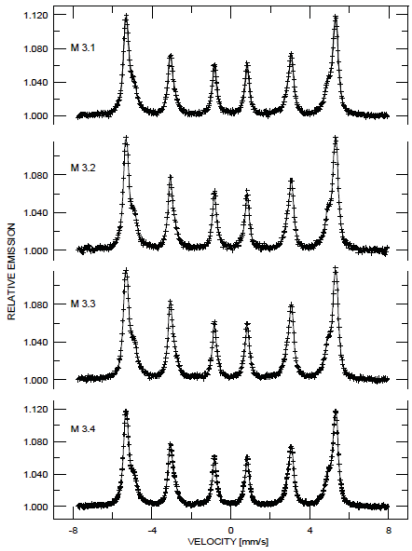

Figure B.7.: Representative Moessbauer spectra obtained from sample C document a ferrite nature of the steel tube. Spectra collected from other samples A and B indicated also only ferrite phase.

B.4.4. Moessbauer spectroscopy

Moessbauer spectroscopy was used to determine volume fraction of crystalline phases in the samples position resolved by analysing four tube sections with a thickness of about 2 mm for every tube.

The results demonstrated that all three samples A, B and C consisted exclusively of ferrite and there was not austenite detected in the samples (Fig. B.7). Consequently, the fraction of retained austenite, if any, was smaller than 0.5 % what represents the detection-limit of this method.

B.4.5. Electron microscopy analysis

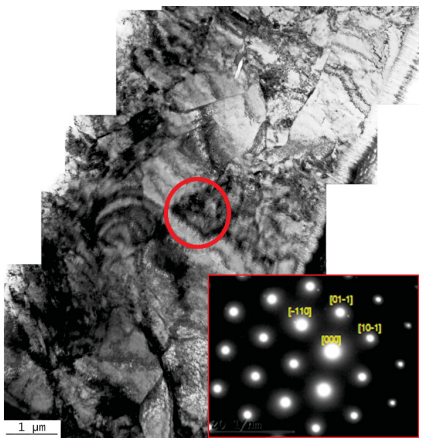

Figure B.8.: Representative overview of the microstructure in TEM lamella out of tube C. The microstructure is ferritic with grains containing high dislocation densities, except a low number of isolated carbides and no relevant precipitation. The red marked region in TEM lamella document representative [111] zone of ferritic microstructure presented in the diffraction pattern at the right bottom corner.

Conventional TEM analysis was performed on four equidistant tube regions for every sample A, B and C. In Fig. B.8, representative conventional TEM micrographs indicate the microstructure of the sample C.

The microstructure of all 12 TEM samples was 100 % ferritic with a very high dislocation density in the order of 10^{15} m-2. Except a very low number of isolated volumes with pearlite structure, no relevant precipitation has been detected in any of the twelve investigated lamellae. A comparison of TEM micrographs obtained from

the twelve TEM lamellas indicated qualitatively, that dislocation density across the tube walls correlates with the cooling intensity.

B.4.6. XRD analysis

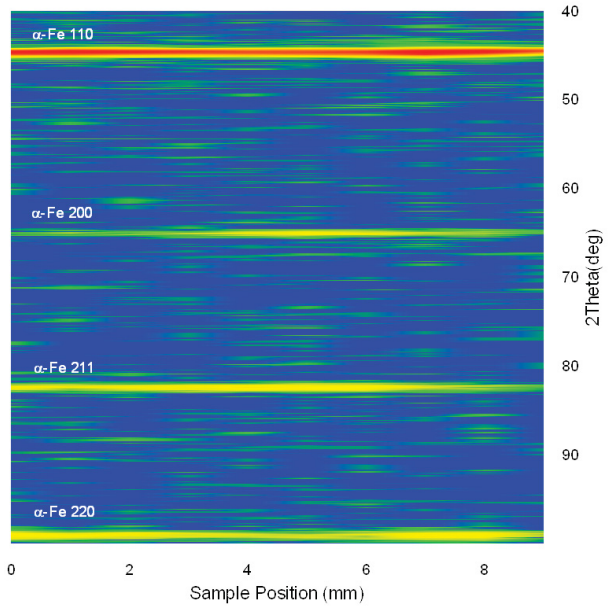

Figure B.9.: $\Theta/2\Theta$ data collected (from inner to outer side) of the tube wall of the sample C using the beam of 0.5 mm in diameter documents the presence of α iron with the corresponding reflections.

Representative X-ray diffraction data collected across the wall of the sample C using the beam of 0.5 mm in diameter is presented in Fig. B.9.

The diffraction data document that the sample consists of crystallite ferrite phase without any traces of austenite; though a relatively intensive cooling rates were applied. Moreover, the results demonstrate that the alloying concept results in suppression of martensite formation even at very high cooling intensity. This can be interpreted by the fact that micro-alloying elements distributed in the lattice interstitial positions hinder the material phase transformation.

B.4.7. Macro- and micro- fracture behavior

Morphology of fractured samples after tensile tests on tubes walls tested as whole as well as on micro-sized samples fabricated from different regions across tube walls.

In Fig. B.11, fractured specimens A, B and C are presented. For the sample A (Fig. B.11a), the fracture contour indicates a ductile behaviour as a consequence of the homogeneous material properties across the wall. In Fig. B.11a, the crack path in sample B is at the angle of 45 degrees with respect to direction of applied force, obviously initiated by the main shear stress. The fracture surface is not straight and one can observe a crack deflection at about one third of tube wall thickness caused by the abrupt material properties change. Obviously the moderate conditions influenced the microstructure and also material properties only in the tube outer region (cf. Fig. B.5b) without modifying microstructure (Fig. B.9). Thus the fracture surface can be used as an indicator of the efficiency of the cooling process – it demonstrates how deep the material properties were modified.

(a) Tube A

(b) Tube B

(c) Tube C

Figure B.10.: Fracture surfaces of the samples A (a) , B (b) and C (c) after tensile experiments. The in-plane width of the samples is equal to tube wall thickness whereby the upper part represents the tube outer surface.

For the sample C, applied cooling intensity resulted in the modification of material microstructure and properties across the whole tube wall thickness (cf. Fig. B.4).

Though the UTS increased significantly and FS decreased (Fig. B.5c), the fracture behaviour is still ductile due to the small grain size and large dislocation density

(Fig. B.8). The combination of high UTS and ductility represents an important achievement of this study.

Figure B.11.: Fracture surfaces of micro-samples machined from tubes A (a), B (b) and C (c) after tensile experiments. The top-bottom sequence corresponds to outer-inner sample position in tube wall.

In order to understand contribution of individual tube regions to the macroscopic fracture behaviour as well as the correlation to the cooling intensity, fractured micro-sized specimens from Fig. B.5 were evaluated (Fig. B.11). The crack surfaces from the sample A indicate homogeneous ductile behaviour over the whole wall thickness documented by constant necking in Fig. B.11a. For the moderately cooled tube B, the first two tensile samples indicate necked brittle fracture, in agreement with Fig. B.11a, caused by only moderate-cooling conditions which modified the material properties only locally. In Fig. B.11a, the brittle fracture of all samples was caused by the intensive cooling. Remarkably, all samples exhibit a certain degree of necking what again documents the presence of ductility in this high-strength material.

An important result of the tensile investigations at macro and micro scales is the fact that small samples (Fig. B.11) exhibited significantly larger FS in comparison with the full sections samples (Fig. B.10). A technological implementation of this effect could results in a significant improvement of overall fracture response of steel tubes manufactured from this steel grade.

B.5. Conclusions

Mechanical-, microstructural- and residual stress properties of three steel tubes differing in applied cooling intensity were analysed using a variety of experimental techniques in order to reveal gradient of structure-property relationship across tube wall. The experimental findings document, that different thermo-mechanical treatments results in the formation of gradiented microstructures of purely ferritic material. Also residual stresses across the wall change significantly after intensive cooling and shift to the compressive domain. The microstructure and stress conditions correlate excellent with hardness and stress strain behaviour of individual tube regions. The intensive cooling results in the formation of hard material especially in outer wall of the cooled tubes with a relatively high ultimate tensile strength and reduced fracture strain. Gradients of hardness, UTS and FS across tube walls indicate that the applied cooling intensity can be effectively used to adjust the mechanical properties in a gradient manner.

Finally multi-method and multi-scale analysis revealed that seamless steel tubes are high tech engineering components with complex structure-property relationship. Consequently, a further optimization of functional tube properties must be based on the optimization of their microstructural and residual stress gradients.

B.6. Acknowledgment

Financial support by the Austrian Federal Government (in particular from the Bundesministerium für Verkehr, Innovation und Technologie and the Bundesministerium für Wirtschaft, Familie und Jugend) and the Styrian Provincial Government represented by Österreichische Forschungsförderungsgesellschaft mbH and by Steirische Wirtschaftsförderungsgesellschaft mbH, is gratefully acknowledged.

This project was supported by “Die Österreichische Forschungsförderungsgesellschaft” FFG Basisprogram and project “2655990 UHSTMRT”.

[107] Wolfgang Bleck, Dietmar Haemberg, Ulrich Prahl, Piyada Suwanpinij, and Nataliya Togobytska. Optimal control of a cooling line for production of hot rolled dual phase steel. *steel research international*, 85(9):1328–1333, 2014.

[108] Wolfgang Bleck, Hubert Hummel, Andreas Kern, and Udo Schriever. Ermuedungsverhalten von mobilkranbauteilen aus hochfesten baustaehlen. *Stahlbau*, 73(11):901–907, 2011.

[109] Wolfgang Bleck, Thorsten Labudde, and Sascha Hoffmann. Challenges in the characterization of new steels. *MP*, 52(9):572–577, September 2010.

[110] J. H. Hollomon C. Zener. Effect of strain rate upon plastic flow of steel. *Journal of Applied Physics, 15(1), S. 22-32*, 1944.

[111] J Klarner, B Buchmayr, and W Rainer. Toughtubes, extrem feinkoernige nahtlose stahlrohre. *BHM*, 156(5):168–174, 2011.

[112] D. Krizan, K. Spiradek-Hahn, and A. Pichler. Relationship between microstructure and mechanical properties in nb-v microalloyed trip steel. *Materials Science and Technology*, 31(6):661–668, 2015.

[113] R. Mahnken. A newton-multigrid algorithm for elasto-plastic viscoplastic problems. *Computational Mechanics*, 15(5):408–425, 1995.

[114] M. Kopcewicz P. Pawluk, E. Skolek and W. Swiatnicki. The comparative study of phase composition of steels using x-ray diffraction and moessbauer spectroscopy. *Solid State Phenomena, Vols 203-204, pp. 150*, 2013.

[115] L.M. Wang, Z.B. Wang, and K. Lu. Grain size effects on the austenitization process in a nanostructured ferritic steel. *Acta Materialia*, 59(9):3710–3719, 2011.

[116] Gerald Winter, Mario Stefenelli, Juergen Klarner, Peter Staron, Torben Fischer, Jozef Keckes, and Bruno Buchmayr. Triaxial residual stresses in thermomechanically rolled seamless tubes characterized by high-energy synchrotron x-ray diffraction. *ASME PVP*, pages V003T03A020–V003T03A020, 2013.

[117] P.J. Withers and H.K.D.H. Bhadeshia. Residual stress. part 1 - measurement techniques. *Materials Science and Technology*, 17(4):355–365, 2001.

[118] P.J. Withers and H.K.D.H. Bhadeshia. Residual stress. part 2 - nature and origins. *Materials Science and Technology*, 17(4):366–375, 2001.

C

Experimental characterization and modelling of residual stress gradients across straight and bent seamless steel tubes

Gerald Winter[a,b], Jürgen Klarner[a], Peter Staron[c], Bruno Buchmayr[b], Jozef Keckes[d]

[a]voestalpine Tubulars GmbH & Co KG, Department R&D, Kindberg, Austria

[b]Department Product Engineering, Chair of Metal Forming, Montanuniversität Leoben Austria

[c]Institute of Materials Research, Helmholtz-Zentrum Geesthacht, Germany

[d]Department Materials Physics, Chair of Material Physics, University of Leoben, Austria

Keywords

seamless steel tubes, residual stress, thermo-mechanical treatment, synchrotron X-ray diffraction, finite element modeling

Abstract

Residual stress gradients across the wall of seamless steel tubes influence decisively the mechanical stability and reliability of automotive and industrial constructions. Irreversible bending moments imposed on the tubes induce gradual and asymmetric elasto-plastic deformation across the tube cross-sections which result in very complex residual stress distributions. The aim of this contribution is to present a novel methodology as well as complementary modeling approach to assess the three-dimensional distribution of triaxial residual stresses in bent steel tubes. The stress characterization was performed using high energy X-ray diffraction at the HEMS beamline of PETRA III synchrotron source in Hamburg as well as using laboratory hole drilling. For the complementary modeling of the stress distribution, a FEM

software package DEFORM^{HT} was used. The results reveal that the stress gradients across the tube wall are primarily influenced by the martensite profile predetermined by the parameters for thermo-mechanical treatment of the tubes. The tube bending causes the formation of continually varying compressive and tensile stresses across the tube circumference whereas the stress magnitude across the wall thickness scales again with the martensite appearance. Finally the results document the importance of the water cooling process control and the influence of the applied bending radius on the resulting stress distributions as well as related mechanical parameters like fracture toughness and fatigue behaviour.

C.1. Introduction

The production of seamless steel tubes comprises a series of sub-processes like billet heating, piercing, push bench rolling, intermediate cooling, reheating, stretch reducing and water cooling. During the production, the variety of thermo-mechanical processing results in the formation of complex residual stress fields across the tube wall which further correlate with a complex gradual steel microstructure induced by the water cooling conditions [124].

The residual stress fields in seamless tubes are able to decisively influence material properties and consequently also the mechanical stability and reliability of automotive and industrial constructions made of [119]. Stresses can primarily influence fracture toughness and ultimate tensile strength of the tubes and secondary modify also oxidation behaviour and weld resistance to cyclic fatigue [120]. When the seamless steel tubes are plastically deformed, plastic deformation results in the formation of additional stress fields which are superimposed on those formed after the production.

The aim of the production route is therefore (i) to pre-adjust the stress magnitude during water cooling and (ii) to control especially tensile stress magnitude.

In order to perform an effective stress management in seamless steel tubes, it is necessary to apply complex characterization approaches in order to determine three-axial stress distributions across the tube wall as a function of complex thermo-mechanical treatment.

High-energy synchrotron X-ray diffraction is used to characterize residual stress profiles across the tube wall (i) of three “as-produced” seamless steel tubes differing in thermo-mechanical treatment conditions and (ii) of a plastically bent tube. The aim is to find out how the thermal treatments influence the stress fields and which stresses remain in the tube after bending.

C.2. Experiment

The tubes analyzed in this work were produced of low alloyed carbon steel containing besides Fe [in weight percent] C [0.2], Si [0.9], Mn [1.0], Cr [0.5], Ni [0.8], Ti, V, B and Nb. The tubes denoted further as A, B and C. Tube A was produced without an application of water cooling, B using a moderate and C using a very intensively water cooling intensity after stretch reduce milling. The different water cooling conditions resulted in varying microstructures across their 10 mm thick walls, as documented in Fig. C.1. The microstructure of tube A consists of homogeneous distributed ferrite and perlite, tube B and C exhibited an increased amount of martensite and bainite especially in the outer tube wall regions (cf. C.1).

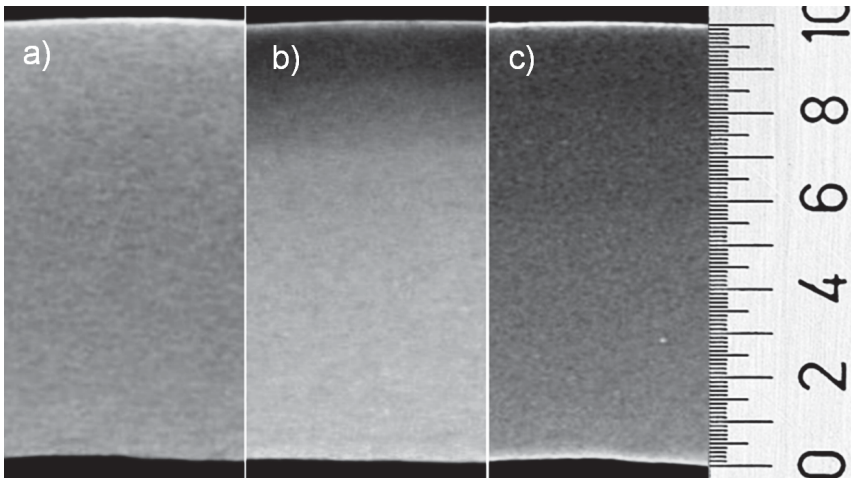

Figure C.1.: Gradient microstructures across the 10 mm thick tube walls A (a), B (b), C (c) induced by the varying water cooling intensity. The darker region at the outer tube wall side in b) indicates the presence of martensite followed by bainite whereby in c) martensite is distributed across the whole cross-section.

Additionally, tube C was bent using a three-point bending device in order to induce plastic deformation and modify the stress distribution across the wall. This tube is further denoted as C_Bent (cf. Figs. C.2a and C.3). The tubes A, B, C and C_Bent were characterized at P07 beamline of the PETRA III synchrotron source in Hamburg using the X-ray energy of 77.5 keV (Fig. C.3a). The cross section of the X-ray beam was 50 µm × 50 µm and the depth resolution achieved with a conical slit cell was about 0.8 mm. Strain measurements were carried out in two steps. At first the X-ray beam was oriented perpendicular to the tube axis in order to assess axial

and tangential strains. Then the beam was oriented parallel to the tube axis and tangential as well as radial strains were characterized in 10 mm thick rings that had been cut from the tubes. During the measurement, the tubes were moved with a step of 0.5 mm (Fig. C.3b) along the beam direction and Debye-Scherrer rings were collected simultaneously using the 2 D detector. By moving the tubes, the focus of the dedicated conical slits also moved within the tube wall and in this way the gauge volume as well as the resolution were defined (Fig. C.3b) [121, 123].

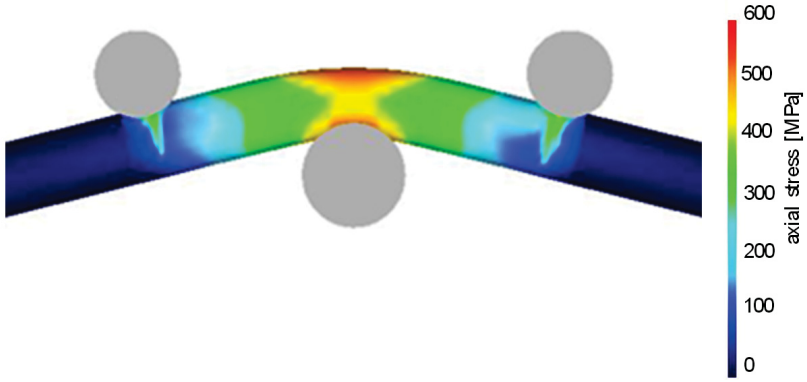

Figure C.2.: FEM model of a bent tube C after plastic deformations shown in colour code for axial stress. The sample is further denoted as C_Bent (cf. Fig. C.1 and Fig. C.3).

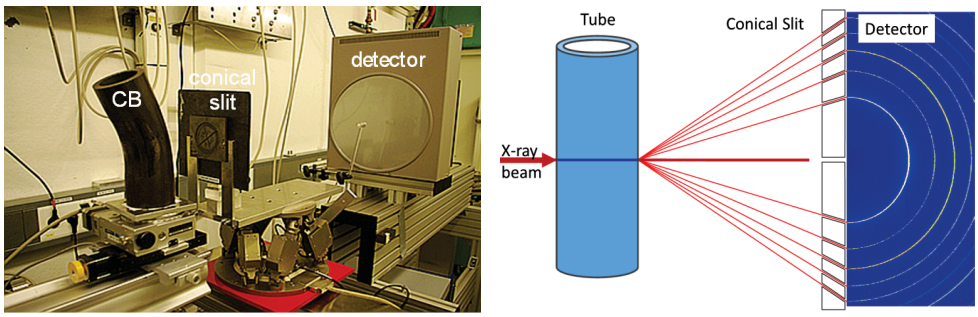

(a) Synchrotron measurement setup **(b)** Synchrotron schematic measurment setup

Figure C.3.: Photograph of the synchrotron experiment on a bent tube (C_Bent) with a conical slit and an X-ray detector (left). By moving the tube in the focus of the conical slit (right), residual stresses were evaluated with a spatial resolution of 0.8 mm from Debye-Scherrer rings observed on the detector.

The diffraction data were used to evaluate lattice spacing $d^{hkl}(x)$ as a function of the position x across tube wall from the measured hkl reflections using Bragg's law. Additionally, small pieces of the tube material were characterized position resolved using the same procedure in order to determine the distribution of unstressed lattice parameters $d_o^{hkl}(x)$ across the wall for the samples A, B and C (Fig. C.1) [125, 122]. The results were used to calculate triaxial strains as follows

$$\varepsilon_i^{hkl}(x) = \frac{d_i^{hkl}(x) - d_0^{hkl}(x)}{d_0^{hkl}(x)} \tag{C.1}$$

where the index i represents axial, tangential and radial components. Strain values were further used to calculate axial, tangential and radial stress components like presented in our previous work [126]. By applying Young modulus E of 225 GPa and Poisson number υ of 0.276, stresses were determined by

$$\sigma_i(x,y,z) = \frac{E^{hkl}}{(1+\upsilon^{hkl})}\left(\varepsilon_i^{hkl}(x,y,z) + \frac{\upsilon^{hkl}}{(1-2\upsilon^{hkl})}\left(\varepsilon_A^{hkl} + \varepsilon_R^{hkl} + \varepsilon_T^{hkl}\right)\right) \tag{C.2}$$

Both X-ray elastic strains as well as residual stresses were determined with an error of 10 %.Additionally, the hole-drilling method was used to determine residual stresses in a near surface region of the bent sample.

C.3. Result and Discussion

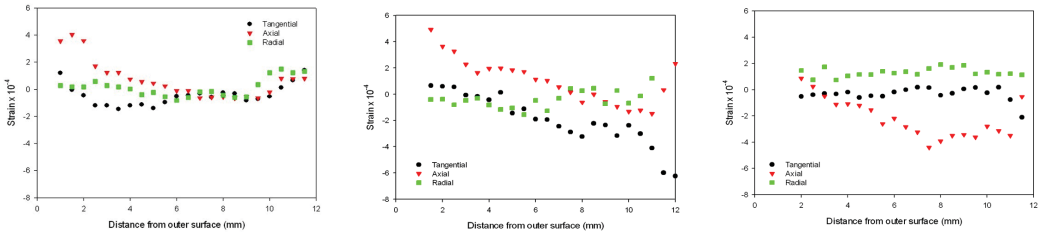

(a) Tube A (b) Tube B (c) Tube C

Figure C.4.: Distributions of tangential, axial and radial residual stresses (from outside to inside) across the walls of A (a), B (b), C (c) tubes. By increasing the water cooling intensity from a) to c), the tensile stresses were reduced and the stress profiles was adjusted.

Residual stress profiles across the wall of tubes A, B and C are presented in Fig. C.4. In tube A relatively high axial, tangential and radial tensile stresses up to 120 MPa on both wall sides are observed. In tube B, axial tensile stresses up to 150 MPa are detected only on the outer wall side whereby the wall inner side is under compression. In tube C, negligible residual stresses are observed on the outer side and the inner side is under compression. The development of the stresses across the walls of A, B and C tubes correlate well with the applied water cooling conditions and wall microstructure gradient (Fig. C.1).

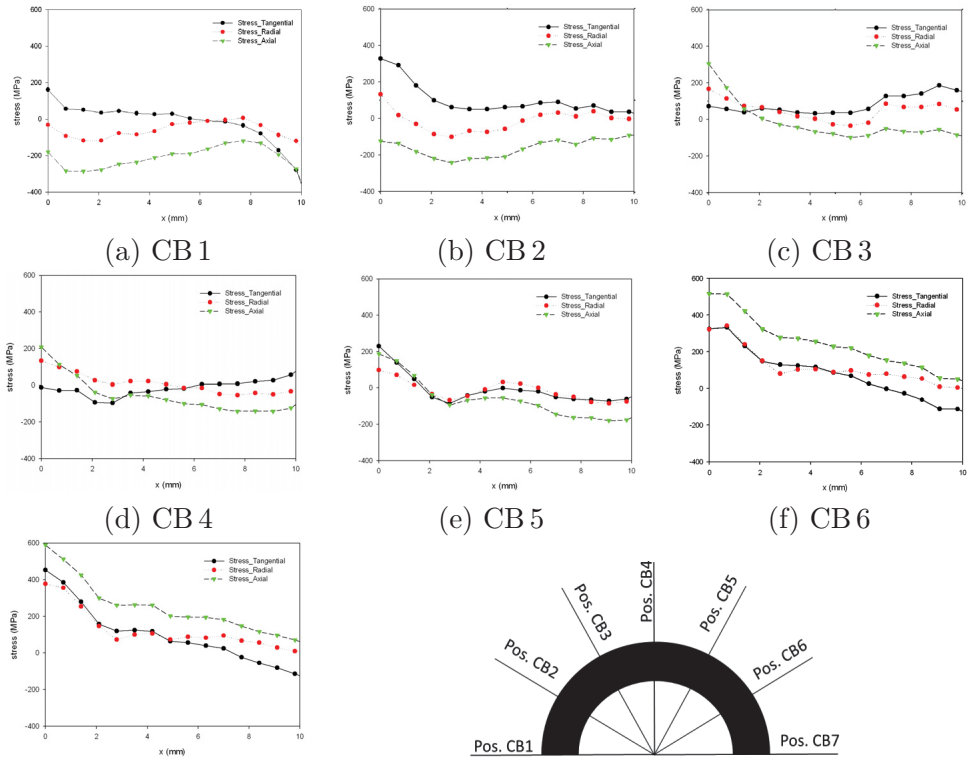

(a) CB 1 (b) CB 2 (c) CB 3

(d) CB 4 (e) CB 5 (f) CB 6

(g) CB 7 (h) Schematic position overview

Figure C.5.: Distributions of tangential, axial and radial residual stresses (from outside to inside) across the wall of the bent tube C (sample C_Bent) measured at seven positions (Pos.) along the tube circumference presented schematically as a black bold half circle at the right bottom corner. Positions CB 1 and CB 7 were the positions with the maximal compressive and tensile stresses applied during the bending (Fig. C.2a), respectively.

The increase of the water cooling intensity resulted in the reduction of tensile stresses as can be recognized in Fig. C.4a. Moreover, further increase of the water

cooling intensity in tube C resulted in the formation of compressive stresses in some regions (Fig. C.4a). Therefore by applying dedicated thermo-mechanical treatments, the magnitude and nature of residual stresses in the tube wall were adjusted. The next aim was to assess how plastic deformation induced by three point bending (Fig. C.2a) influences the stress profile across the tube wall and as well as at which position across the wall thickness the maximal residual stresses occur after the deformation. For this reason, residual stresses in the tube C_Bent (Fig. C.2a) were analysed using the same synchrotron approach (Fig. C.3).

The characterization was performed at seven positions along the tube circumference with an azimuthal distance of 30 degrees (Fig. C.5). Positions CB 1 and CB 7 were the positions with the maximum compressive and tensile stresses applied during the bending, respectively (Fig. C.2a).

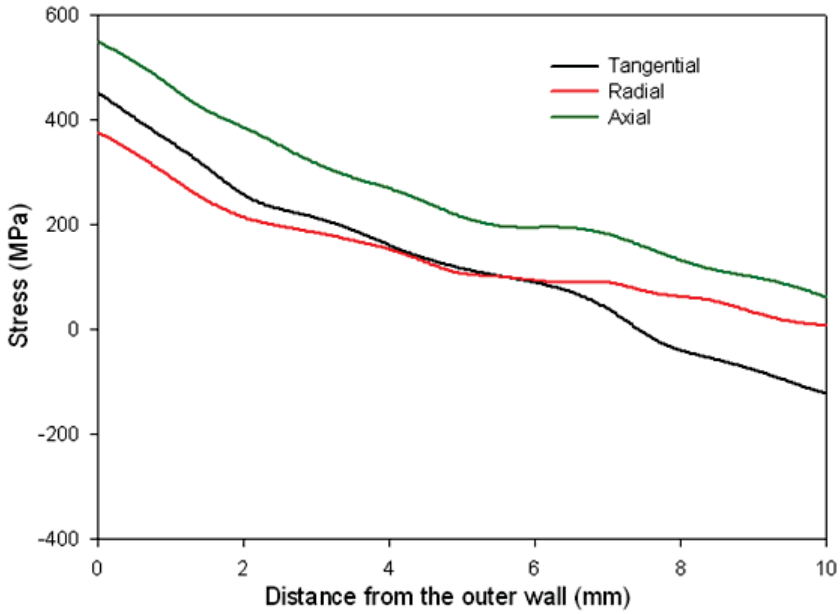

Figure C.6.: Modelled residual stress distributions in the bent tube after plastic deformation (Fig. C.2a) obtained using FEM software DEFORM^{HT}.

The results from Fig. C.5 indicate that plastic deformation induced by the three-point bending (Fig. C.2a) resulted in a very complex inhomogeneous stress distribution across the tube wall. At position CB 1, where the maximal compressive stress was applied, axial stresses remained compressive of about -300 MPa in the outer tube wall. The compressive axial stresses at position CB 1 relaxed interestingly towards

the inner and outer wall regions. At position CB 7, where the maximal tensile stress was applied, axial residual stresses remained about 600 MPa (Fig. C.5) in the outer tube wall, without any relaxation at the surface. In the inner wall of the CB 7 position, the axial stresses were negligible, that could be explained by a possible local fracture. At position CB 4, which was identical with the neutral axis during the bending (Fig. C.2a), the axial stresses were still about +200 MPa on the outer tube wall. This indicates that the deformation was very inhomogeneous. In general, the results from Fig. C.5 document that the bending moment and the resulting plastic deformation caused a residual stress gradient of about 1 GPa (-400 MPa at CB 1 to +600 MPa at CB 7) across the tube C_Bent.

The measured stress distributions from Fig. C.5 were modelled using the FEM software DEFORM^{HT} (Fig. C.2a). The calculated data were in a relatively good agreement with the experimental results. In Fig. C.6, an example of the modelled stress profiles for the position CB 7 documents that the model could approximately reproduce the stress magnitudes as well as stress gradients across the tube wall.

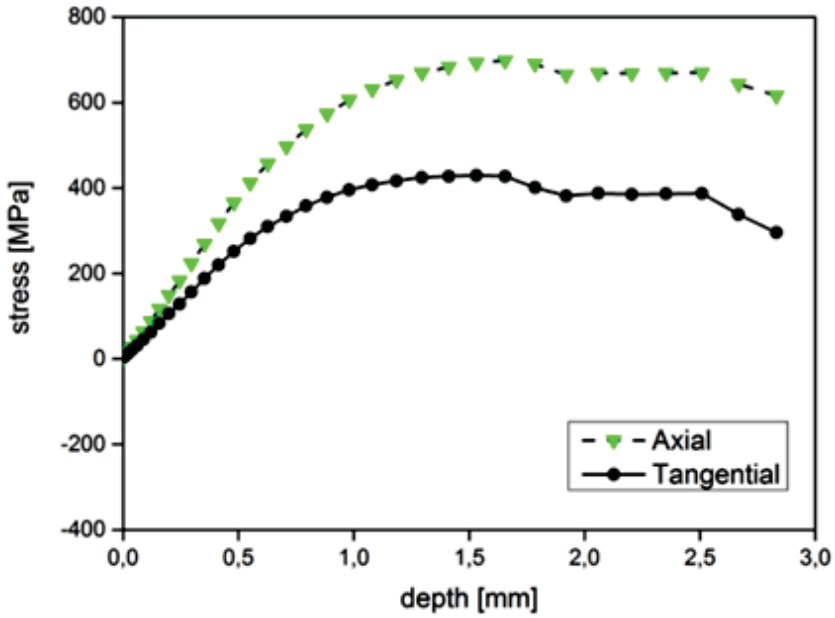

Figure C.7.: Distributions of residual stresses (from outside to inside) in the tube C_Bent measured at the position CB 7 (Fig. C.5) using the hole drilling approach.

Complementary, tube C_Bent was characterized using the hole drilling method. In Fig. C.7, results obtained for the measurement position CB 7 are presented. The

in-plane stresses correspond to the axial and tangential stresses from Fig. C.5 obtained at the position CB 7. The axial and tangential stresses in Fig. C.7 reach values of about 650 and 400 MPa at the depths of 1.5 mm and more. The stress levels correspond relatively good with the respective stress values of 600 and 450 MPa from Fig. C.5. The differences in the absolute stress magnitude (between Fig. C.5 and C.6) and the negligible surface stresses (Fig. C.7) can be interpreted by the limited accuracy of the hole drilling approach as well as by the surface stress relaxation.

C.4. Summary

Synchrotron high-energy X-ray diffraction, hole drilling and FEM approaches were used to characterize residual stresses in three seamless steel tubes differing in the applied water cooling conditions. The results demonstrate that the water cooling intensity influences microstructural as well as residual stress gradients across the tube wall. By using dedicated water cooling conditions, it is possible to decrease tensile stresses in the tubes significantly. Additionally, a tube deformed plastically using three point bending was analysed. The results show that the bending resulted in the formation of stress peaks in the range from -300 MPa up to 600 MPa in the case of axial stresses.

Methodologically, the results demonstrate that conical slit cell can be effectively used to evaluate the magnitude of X-ray elastic strains and macroscopic residual stresses in steel tubes with a resolution of 0.8 mm.

[119] J.L. Chaboche. Constitutive equations for cyclic plasticity and cyclic viscoplasticity. *International Journal of Plasticity*, 5(3):247–302, 1989.

[120] MG Cockcroft and DJ Latham. Ductility and the workability of metals. *J Inst Metals*, 96(1):33–39, 1968.

[121] M.E Fitzpatrick. *Analysis of Residual Stress by Diffraction Using Neutron and Synchrotron Radiation*. Taylor and Francis, London and New York, 2003.

[122] H.F. Poulsen, S. Garbe, T. Lorentzen, D.J. Jensen, F.W. Poulsen, N.H. Andersen, T. Frello, R. Feidenhans'l, and H. Graafsma. Applications of high-energy synchrotron radiation for structural studies of polycrystalline materials. *J Synchrotron Radiat*, 4(3):147–154, 1997. cited By (since 1996)95.

[123] A. Pyzalla. Methods and feasibility of residual stress analysis by high-energy synchrotron radiation in transmission geometry using a white beam. *J Nondestruct Eval*, 19:21–32, 2000.

[124] George F Schrader and Ahmad K Elshennawy. *Manufacturing processes and materials*. Society of Manufacturing Engineers, 2000.

[125] Armin Segmueller, IC Noyan, and VS Speriosu. X-ray diffraction studies of thin films and multilayer structures. *Progress in Crystal Growth and Characterization*, 18:21–66, 1989.

[126] Gerald Winter, Mario Stefenelli, Juergen Klarner, Peter Staron, Torben Fischer, Jozef Keckes, and Bruno Buchmayr. Triaxial residual stresses in thermomechanically rolled seamless tubes characterized by high-energy synchrotron x-ray diffraction. *ASME PVP*, pages V003T03A020–V003T03A020, 2013.

D

Macro- and microscopic properties of gradient ultra-high-strength seamless steel tubes produced by dedicated thermo-mechanical treatments

Gerald Winter[a], Jürgen Klarner[a], Bruno Buchmayr[b], Jozef Keckes[b]

[a]voestalpine Tubulars GmbH & Co KG, Department R&D, Kindberg, Austria

[b]University of Leoben, Austria

Abstract

Thermo-mechanically rolling of high-strength steels is typically used to adjust mechanical characteristics of engineering components. In the case of seamless steel tubes, the treatment results in the formation of non-homogeneous distributions of phases, microstructure and residual stresses. These generated gradients influence the overall mechanical response of tubes decisively. In this contribution, properties of seamless steel tubes produced, using a set of thermo-mechanical rolling treatments, are analyzed at macro and micro scale in order to reveal the correlation between local and global mechanical behavior, heat treatment conditions and local microstructure as well as residual stress state. The gradient tubes are characterized by moessbauer spectroscopy, transmission electron microscopy, intendation and X-ray diffraction. Tensile and fracture tests are performed on specimens out of tube wall sections as well as on miniaturized specimens isolated from distinct regions. The results document that local mechanical properties vary continuously across the tube walls. The investigated properties of these seamless steel tubes correlate (i) with the phase distribution of ferrite, perlite, bainite and martensite as well as (ii) the applied vary cooling intensities during the manufacturing process. The multi-scale characterization approach opens the possibility to understand the mechanical behavior of complex gradient materials.

Keywords

seamless steel tubes, thermo-mechanical treatment, mechanical properties, microstructure, structure-property gradients

D.1. Introduction

Seamless steel tubes are used in various engineering applications and have to fulfill a variety of functional requirements like mechanical stability, fatigue resistance and chemical durability. The increasing demand for production of light-weight, high-strength and high-performance tubes requires an optimization of intrinsic material properties [128] like ultimate tensile strength (UTS), fracture strain (FS) and fracture toughness (FT), as well as macro and micro structural and design aspects.

The production of seamless steel tubes [133] includes a series of sub-processes like billet heating and piercing, push bench processing, intermediate-cooling for phase transformation, reheating, stretch reducing and surface spraywater cooling to fix and define the required properties. During the production, the variety of thermo-mechanical intensities results in the formation of complex residual stress fields across the tube wall which further correlate with a complex gradual steel microstructure induced by the cooling conditions [129]. In the past, primarily mechanical, but also other functional properties of tubes were characterized using approaches which provided usually overall "volume-averaged" data like UTS, FS and toughness.

During the production of seamless steel tubes, thermo-mechanical treatment conditions are applied and shift the residual stress profile across the tube wall as well as the microstructure to a complex formation of gradiented mechanical properties [130]. To understand the overall structure property relationship of seamless steel tubes as gradient engineering component, it is necessary to understand the relationship between the local (i) microstructure, (ii) residual stress, (iii) phase, (iv) mechanical property and the applied (v) manufacturing and (vi) treatment conditions.

The aim is to perform multi-scale characterizations of denoted properties for seamless steel tubes by performing tensile tests at specimens retrieved on (i) whole tube wall sections and (ii) local small sections from different regions across the tube wall. The mechanical data correlates with results from the microstructural characterization performed using a variety of advanced analytical techniques [131, 132].

D.2. Tube samples

Five types of gradient seamless steel tubes are analyzed in this work and are further distinguished as T1, T2, T3, T4 and T5. These tubes from T1 - T5 are low alloyed weldable carbon steels with an outer diameter of 168.0 mm and 10.0 mm wall thickness. Tubes T1 to T4 contain beside iron the following main elements in maximum weight percent: C [0.20], Si [1.00], Mn [1.50], Cr [1.50], Ni [1.50], Mo [0.25] as well as micro alloying elements Ti, V, Nb and B. These tubes are all from the same heat and further chemical composition but differed in the applied cooling conditions. For tube T1 no cooling, for T2 a moderate cooling, for T3 a strong cooling and for T4 a very intensive cooling rate was chosen.

Tube T5 accords to the standard - SEW 090-2 from 1993 “High tenacity quenched and tempered fine grain steel” [135] and contains beside iron the following main elements in maximum weight percent: C [0.22], Si [0.86], Mn [1.80], Cr [1.60], Ni [2.10], Mo [0.74]. Tube T5 was similar to T1 only cooled on air after the last forming operation (stretch reducing) but subsequent by conventional quenching and tempering (Q&T) treatment, according to the SEW standard, was applied to set grade S890QT.

Light-optical micrographs in Fig. D.1 give an overview of the visible microstructural gradients across tube walls for T1 - T5 from HNO3 etched tube specimens. In the case of tube T1, the non-cooling condition resulted in the formation of an uniform microstructure across the whole tube wall. Tube T2, the applied moderate cooling intensity caused a formation of bainite and martensite in the outer tube wall region visible as darker shading. At the strong cooled tube T3, the boundary of the modified darker microstructure layer was moved nearly to the tube wall center. For the intensively cooled tube T4, the microstructure was completely homogeneous modified across the whole tube wall. In the Q&T tube T5, the microstructure is also homogeneous like tube T1 without local darker shadings.

In general observed shadings at micrographs in Fig. D.1 of tube T1 - T5 are etched very strong to distinguish the influenced areas. The shadings consist locally of linear transmissions, which can be interpreted as the rolling direction.

D.3. Experimental characterization

D.3.1. Mechanical tests

Vickers hardness HV 0.5 across the tube wall was determined by using Buehler Micromet 5104 system.

Micro tensile tests on samples with length 22.0 mm, width 1.0 mm (6.0 mm) and thickness 1.0 mm, machined from different positions across tube wall were performed by using Kammrath & Weiss system equipped with 5 kN load sensor in strain-controlled mode.

Macro tensile tests on samples with length 320.0 mm, width 25.0 mm (40.0 mm) and thickness 10.0 mm, machined from tube wall sections were performed using ZWICK material testing machine BPC-F1200HN.F11.

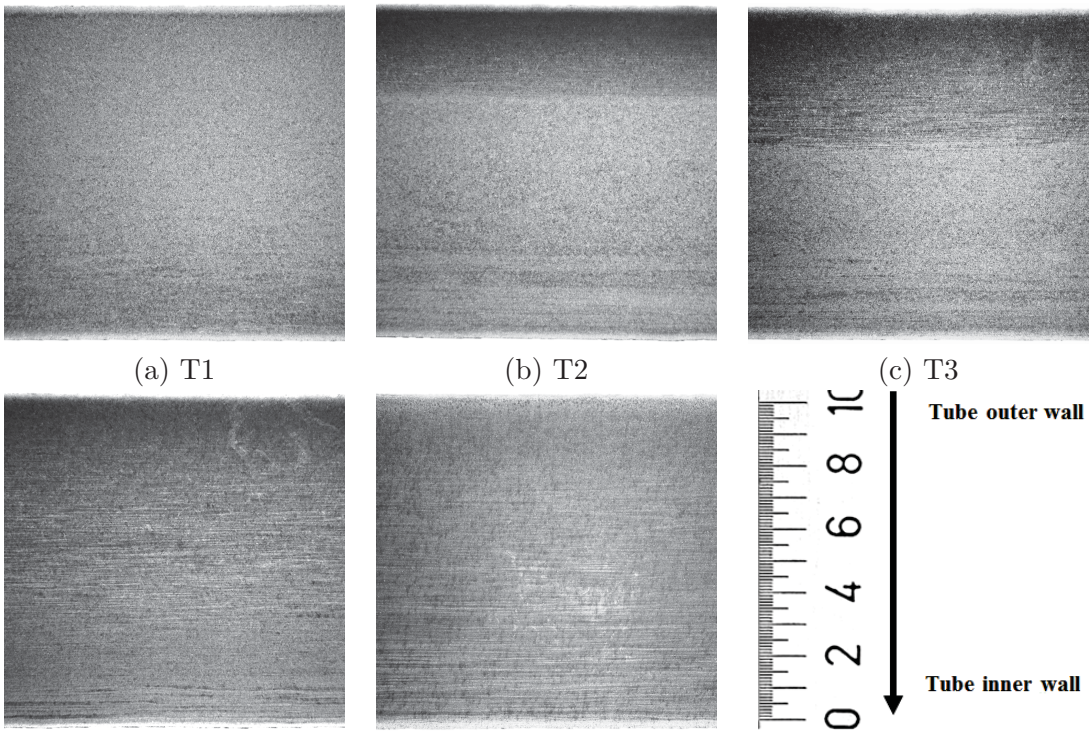

(a) T1 (b) T2 (c) T3

(d) T4 (e) T5 (f) Scale [10 mm]

Figure D.1.: Gradient microstructures across the 10 mm thick tube walls of investigated samples T1 - T5. The influenced area for T1 to T4 is induced by the varying cooling intensity increasing from no cooling at T1 up to intensive cooling at T4 and for T5 by Q&T treatment.

D.3.2. Moessbauer spectroscopy

Moessbauer [134] 57Fe spectra were measured in scattering geometry using a standard Moessbauer spectrometer in a constant acceleration mode with a 57Co(Rh) radioactive source. The spectra were measured at room temperature on "coin" specimens diameter with 25.0 mm and 1.00 mm thickness, machined from different positions across the tube wall. The relative contents of individual Fe-bearing phases were monitored through the corresponding spectral areas.

D.3.3. Electron microscopy

Microstructure present in the steel tube walls was investigated by standard scanning and transmission electron microscopy (SEM and TEM) using LYRA3 FEG-SEMxFIB and JEM-2100F systems, respectively.

D.3.4. X-Ray diffraction analysis

Scanning X-ray diffraction with an X-ray beam of 0.5 mm in diameter across the wall of samples T1 - T5 was performed using Rigaku Smartlab system equipped with X-ray mirror, focusing optics and scintillation detector using Cu-K α radiation [127].

D.4. Results and discussion

D.4.1. Micro-hardness profiles

Results from hardness HV 0.5 measurements across vary heat-treated tube walls of T1 - T5 are presented in Fig. D.2. The shown lines are the linear fitted HV 0.5 hardness values for the tube cross sections T1 - T5. The hardness of tube T5 is the lowest in the range of 348 - 363 HV 0.5 compared to the data from other analyzed tubes and documents that classical Q&T treatment influence the mechanical properties of the material only little. In the uncooled tube T1, the observed hardness is in the range of 395 - 403 HV 0.5. In the moderate cooled tube T2, the hardness is nearby constant of about 402 HV 0.5 over the cross section. In the strong cooled tube T3, the hardness increase is pronounced of 410 – 422 HV 0.5. The intensively cooled tube T4 shows the highest increasing with hardness values up to 420 - 437 HV 0.5.

All five investigated tube types exhibit a hardness increase from tube outer to inner wall whereby the most-pronounced hardness gradient is observed in tube T4. The results infer that by adjusting the cooling intensity, the mechanical properties across the tube wall can be effectively tuned.

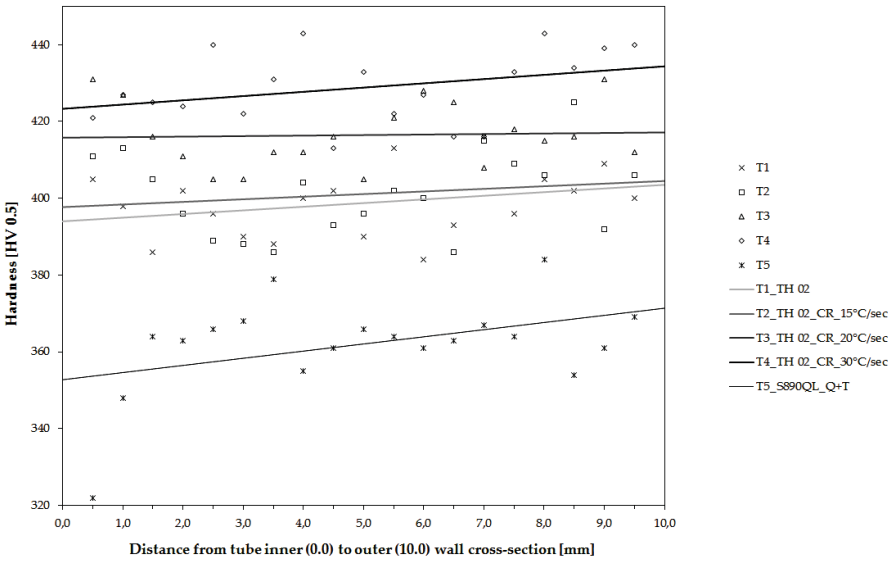

Figure D.2.: Hardness distribution (HV 0.5 - linear fitted data) from inner to outer side of the tube wall indicates the influence of varying cooling intensity on the local mechanical properties of steel tubes T1 to T4 and for tube T5 the influenced behavior by Q&T treatment.

D.4.2. Macro-tensile tests

Results from macro-tensile tests performed on specimens fabricated from whole tube wall sections with a thickness of 10 mm (cf. Fig. D.1) are presented in Fig. D.3. Similar as the hardness data from Fig. D.2 also the stress-strain responses document that the varying cooling intensity modified the mechanical properties of the tubes significantly for T1 to T4 and the Q&T treatment for T5.

The stress-strain response of tube T5 (Fig. D.3) exhibits a very pronounced yield point and small UTS in comparison with data from the other four tubes. For the tubes T1 - T4, yield points are much less distinct and UTS increase gradually as a function of the increasing cooling intensity and transformed phases (Fig. D.1). The maximum yield as well as ultimate strengths is observed at the data from tube T4 produced using very intensive cooling rate, in agreement with the hardness data from Fig. D.2.

The stress-strain data's from Fig. D.3 document that tensile load about the magnitude of the UTS limit of T5 will cause in an abrupt fracture when the maximum yield stress is slightly exceeded. T1 to T4, tensile loads exceeding yield stresses will

result in a progressive material plastification due to the fine grained microstructure. The comparison of data from T1 - T4 document that the cooling treatment after the last forming operation results in an increasing of UTS which saturates in T2 - T4 at the same level and therefore it is independent of the cooling intensity itself.

In the case of the yield stresses of tubes T1 - T4 it can be shown, that the increase of the cooling rate increases the yield stress too. So there is a systematical and proportional relationship ascertainable. Further, yield stresses and also important dependent functional parameters like toughness and fatigue are expected to be improved and can be effectively adjusted or tuned by intensive surface cooling of seamless steel tubes.

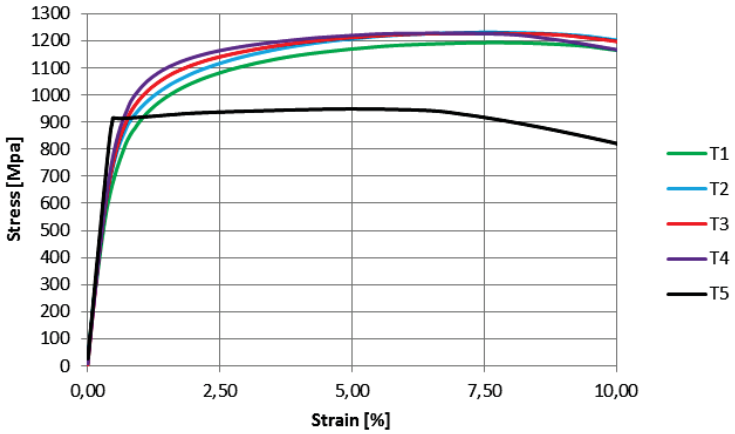

Figure D.3.: Results from macro-tensile tests performed on whole tube wall section specimens document the variation of mechanical properties of the individual manufactured tubes T1 - T5.

D.4.3. Micro-tensile tests

Results from tensile tests performed on micro tensile samples machined from different regions across the tube walls are presented in Fig. D.4. The results document that the microstructural gradients observed in Fig. D.1 result in gradual stress-strain response of individual tube regions (Fig. D.4).

In the uncooled tube T1, a region with the smallest UTS is in the outer tube wall area. This effect can be interpreted by the presence of tensile residual stresses up to 150 MPa reported in our previous study [137, 136]. In TM-treated tubes T2 to T4 by increasing the cooling intensity, UTS of the individual regions increase and the

maximum UTS can be observed reversely always in the outer regions. The outer tube region of T4 experienced the most intensive cooling rate and shows the highest UTS of ~1450MPa (Fig. D.4), in accordance with the hardness data (Fig. D.2).

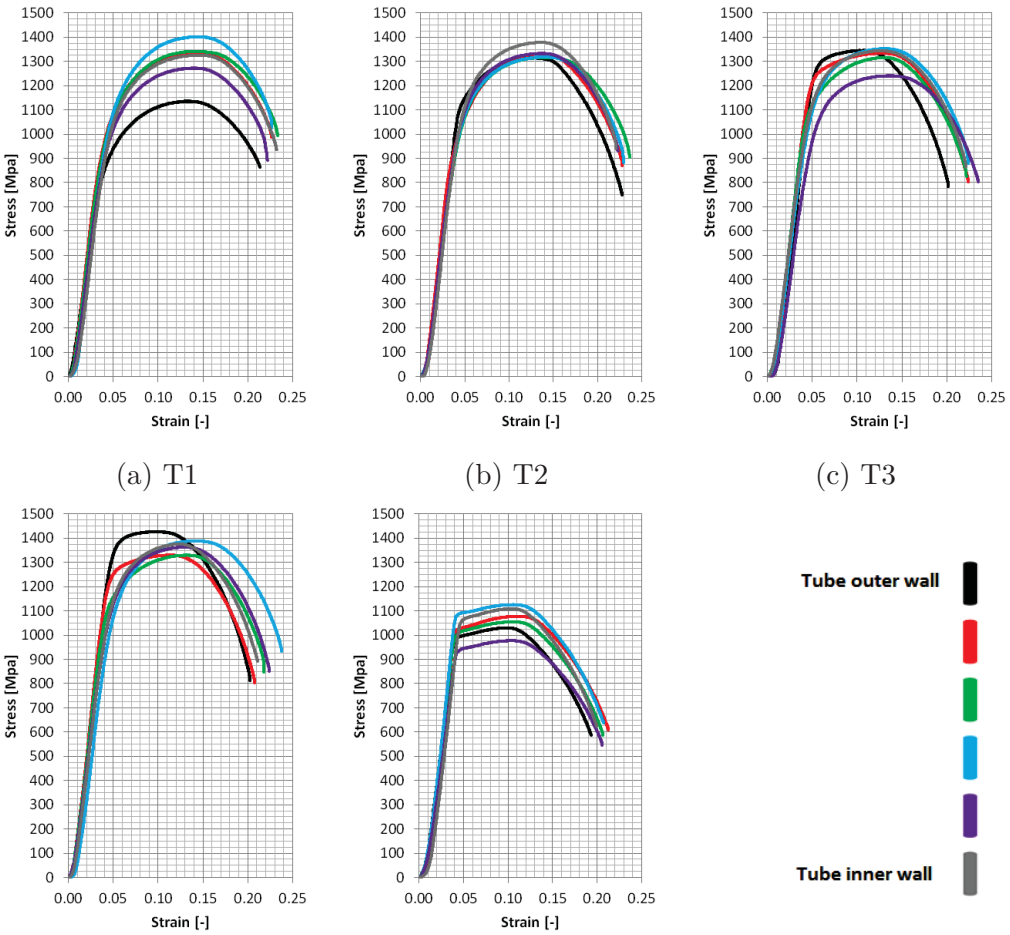

(a) T1 (b) T2 (c) T3

(d) T4 (e) T5 (f) Position scale

Figure D.4.: Results from tensile tests performed on miniaturized specimens document the variation of mechanical properties across the tube wall of T1, T2, T3, T4, and T5 tubes. The results correlate with the observed data given in Fig. D.3, performed on macro-sized tensile samples.

A detailed analysis of the stress-strain responses and UTSs from T4 individual regions (Fig. D.4) indicates that regions with highest UTS and yield stresses occur at the outer tube wall side at the three outer regions. This can be interpreted by the

very intensive cooling as well as by a secondary structural recovery after the cooling, which is caused by outer wall temperature increasing caused by the heat stored in the inner tube region.

This process resulted in a changing of the stress-strain curve whereby the elasto-plastic transition become more abrupt and simultaneously UTS as well as yield stresses increased although the fracture strains were not significantly reduced.

D.4.4. Fracture behaviour of the tube walls

After the tensile tests the morphology on full tube wall specimens of fractured samples were analyzed by using stereo-optical microscopy. In Fig. D.5, pictures of fractured specimens for tube T1 - T5 are presented.

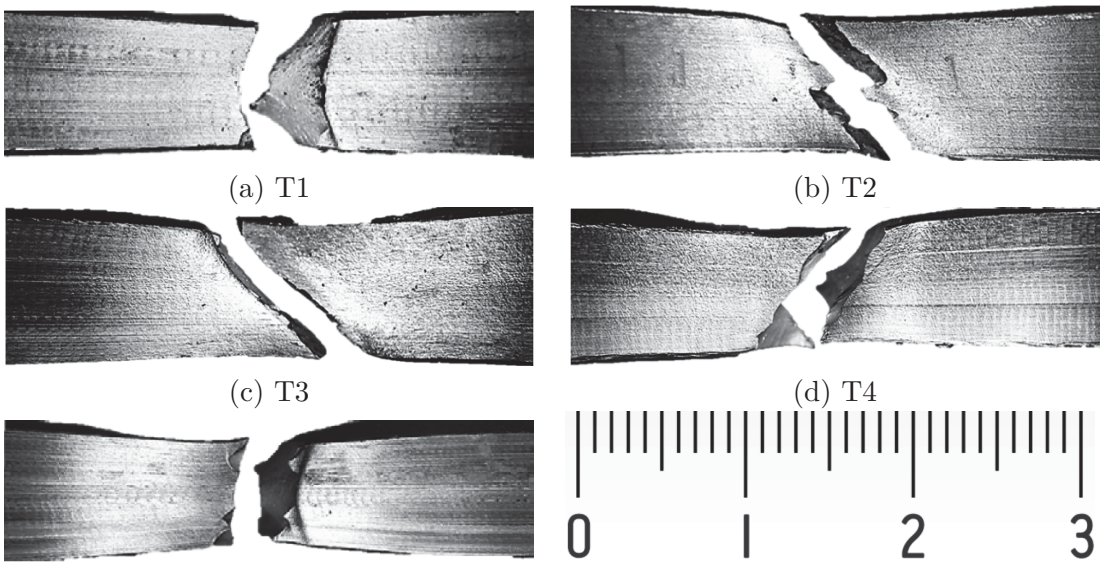

(a) T1 (b) T2 (c) T3 (d) T4 (e) T5 (f) Scale [3 cm]

Figure D.5.: Fracture surfaces of the samples T1 - T5 after tensile tests. The in-plane width of the samples is equal to the tube wall thickness whereby the top of the pictures represents the tube outer surface.

At tube T1, the fracture contour indicates a ductile behavior as a consequence of the homogeneous material properties across the tube wall cross section. The curved fracture surface was caused by inhomogeneous cooling ambient conditions which resulted in a formation of natural thermal gradients and consequently also

in the modification of microstructure profile as well as local mechanical properties (Fig. D.3).

The crack path specimen in tube T2 is at an angle of 45 degrees with respect to the direction of the applied force, obviously initiated by the main shear stress. The fracture surface is not straight and a crack deflection appeared at about one third of the tube wall thickness refers to outer tube wall side caused by the abrupt changing of material properties (Fig. D.1). Obviously, very moderate cooling conditions influenced the microstructure and also the materials properties only in the tube outer region. Thus the fracture surface can be used as an indicator of the efficiency of the cooling process, it demonstrates how deep the material properties were influenced.

In tube T3, crack deflection is still present but even though not so pronounced as in T2 and can be observed at about 2/3 of tube wall in agreement with the microstructure profile from Fig. D.1. In T4, the angle of the crack path can be assumed as homogenous across the whole tube wall cross-section. Cracked specimen T4, illustrated in Fig. D.5, show that the tube wall borders reveal local material hardening which results in a fracture surface coarsening.

In tube T5, the fracture surface is straight and indicates a brittle abrupt fracture which is in an excellent agreement with the observed elasto-plastic transition given in Figs. D.4 and D.5.

D.4.5. Local fracture behaviour across tube wall

After the tensile tests on the micro-sized samples the morphology of fractured samples, machined from different regions across tube wall were analyzed by using optical stereo-microscopy (Fig. D.6).

Although all micro-sized specimens exhibit a necking after the fracture, an analysis of the crack path angles from the individual tube regions indicates very different fracture behavior caused by the applied cooling rates. In tubes T1 - T4 a ductile response with varying angles of fracture surfaces can be obtained, but there is no direct correlation to the microstructure data from Fig. D.1.

Oblique crack can be interpreted by a local microstructure gradient within the micro-sized samples. In case of T5, all fracture surfaces are straight and indicate brittle response as well as pronounced necking caused by the homogeneous tempering treatment after quenching. This correlates also with the data from Fig. D.4 showing the same form of stress-strain response from individual regions across the tube wall.

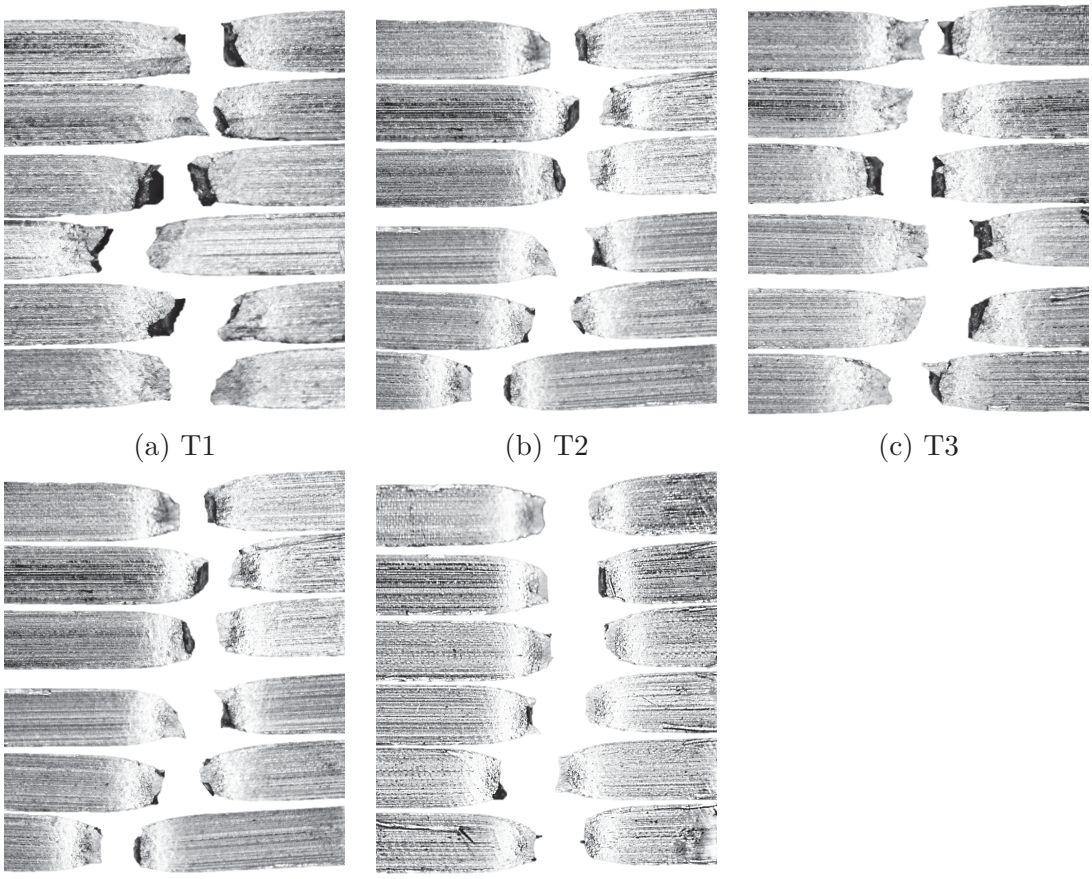

(a) T1 (b) T2 (c) T3

(d) T4 (e) T5

Figure D.6.: Fracture surfaces of the micro-sized samples T1 - T5 after tensile tests. The in-plane width of the samples is 1.0 mm whereby the top of the pictures represents the tube outer surface.

D.4.6. XRD analysis

Representative X-ray diffraction data collected across tubes walls of T1 - T5, measured with beam of 0.5 mm in diameter, are presented in Fig. D.7. The diffraction data documents that all samples consisted primarily of crystallite ferrite phases as indicated by *hkl* reflections (Fig. D.7).

Weak intensities of unnamed reflections in Fig. D.7 indicate a presence of austenite with a very small volume fraction as far as the logarithmic scale is considered. Very significant differences between the diffraction pattern data from tube T1 to T4 in comparison with those of tube T5 are observable. All ferrite hkl reflections collected from tubes T1 to T4 exhibit a significant broadening which was obviously caused

by the thermal treatment and modified the material microstructure.

An increase of *f*ull *w*idth of *h*alf *m*axima (FWHM) of diffraction peaks is usually attributed to small crystallites sizes and/or to formation of strains of second and third orders as a result of dislocation formation. So large FWHMs of ferritic reflections observed at the specimens for T1 to T4 confirm a very fine-grained microstructure. In tube T5, FWHMs of ferritic reflections are much less pronounced, which indicates that the induced Q&T treatment results in grain growth and structural recovery. Unfortunately, the diffraction data from Fig. D.7 does not display boundaries of microstructural regions which were observed for tubes T2 and T3 in Fig. D.1. This may be caused by too large instrumental broadening of the peaks. In order to verify the role of austenite as well as local microstructure, Moessbauer and electron microscopy analysis were done.

D.4.7. Moessbauer spectroscopy

Moessbauer spectroscopy (MS) was used to determine volume fraction of position resolved crystalline phases in samples by analyzing four tube sections with a thickness of about 2 mm for each tube. The results demonstrate that all five tubes exclusively consist of ferrite and there isn't any austenite detectable. Therefore, fraction of (retained) austenite, if present, was smaller than 0.5 %. This represents also the detection-limit of this method.

D.4.8. Electron microscopy analysis

Conventional TEM analysis was performed on tube wall cross section of all tubes in various regions. In Fig. D.8, representative conventional TEM micrographs indicate microstructures of the samples T1, T4 and T5. In line with the results of MS experiments, TEM microstructures of T1 and T4 were almost fully ferritic (α-Fe), similar to each other with a very high dislocation density in the order of $10^{15}\,\mathrm{m}^{-2}$.

For Q&T treated tube T5, a tempered BCC martensite microstructure was detected using STEM dark field from a thin TEM lamella. The microstructure consists of ferritic micro grains with a reduced dislocation density and numerous precipitates which mostly belong to the M23C6 carbide phase (Fig. D.8).

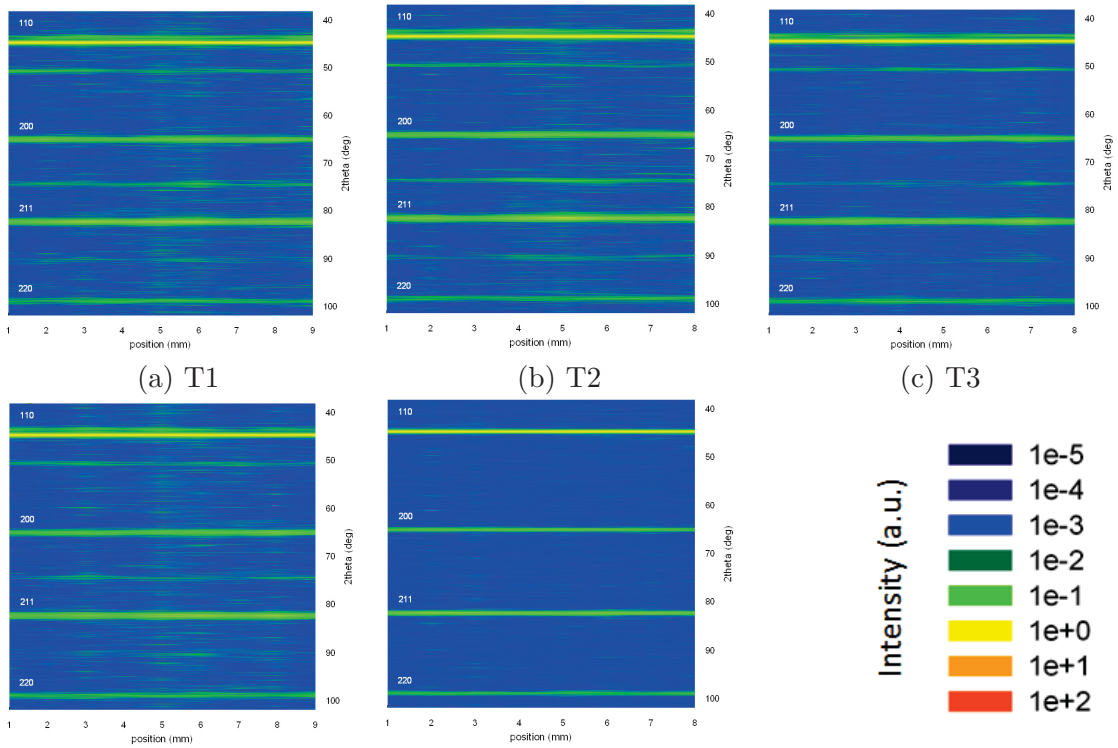

(a) T1 (b) T2 (c) T3

(d) T4 (e) T5 (f) Colour code scale

Figure D.7.: Diffraction data $\Theta/2\Theta$ collected (from inner to outer side) of the tube wall of T1-T5 using the beam of 0.5 mm in diameter documents the presence of α-iron with the corresponding reflections as well as traces of austenite.

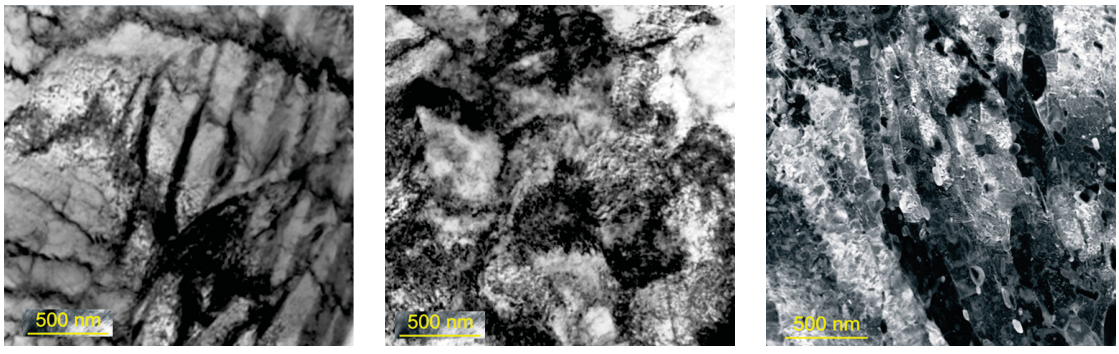

(a) T1 (b) T4 (c) T5

Figure D.8.: Representative TEM micrograhs of tube T1, T4 and T5 document the microstructural development.

D.5. Conclusions

Mechanical and microstructural properties of five steel tubes differing in applied cooling intensity and Q&T treatment were analyzed by using a variety of experimental techniques in order to reveal the gradient of structure-property relationship across tube walls. The experimental findings show, that different thermo-mechanically treatments results in the formation of gradient microstructures of exclusively ferritic phases with a relatively high dislocation density in tubes T1 - T4. In the case of tube T5, ferritic micro grains with a reduced dislocation density and numerous precipitates were found. The microstructure results correlate with hardness and stress strain behaviors of individual tube regions.

The intensive cooling results in the formation of hard material especially in outer wall areas of cooled tubes with a relatively high ultimate tensile strength and reduced fracture strain. Gradients of hardness, UTS and FS across tube walls indicate that the applied cooling intensity can be used effectively to adjust the mechanical properties in a determined manner. The reduction of dislocation density and formation of precipitates in tube T5 caused a decrease of important mechanical properties.

Finally multi-method and multi-scale analysis revealed that seamless steel tubes are high tech engineering components with complex structure-property relationship. Consequently, a further optimization of functional tube properties must be based on the optimization of their microstructural and residual stress gradients.

D.6. Acknowledgement

Financial support by the Austrian Federal Government (in particular from the Bundesministerium für Verkehr, Innovation und Technologie and the Bundesministerium für Wirtschaft, Familie und Jugend) and the Styrian Provincial Government represented by Österreichische Forschungsförderungsgesellschaft mbH and by Steirische Wirtschaftsförderungsgesellschaft mbH, is gratefully acknowledged.

This project was supported by “Die Österreichische Forschungsförderungsgesellschaft” FFG Basisprogram and project “2655990 UHSTMRT”.

[127] Anas BALTUSNIKAS and Rimantas Levinskas. Xrd analysis of carbide phase in heat resistant steels. *Mater. Sci*, 12(3):192–198, 2006.

[128] W. Bleck. Advanced high strength steels for the automotive industry. *Stahl und Eisen 134, Nr.7, page 25-34*, 2014.

[129] Wolfgang Bleck, Dietmar Haemberg, Ulrich Prahl, Piyada Suwanpinij, and Nataliya Togobytska. Optimal control of a cooling line for production of hot rolled dual phase steel. *steel research international*, 85(9):1328–1333, 2014.

[130] Wolfgang Bleck, Thorsten Labudde, and Sascha Hoffmann. Challenges in the characterization of new steels. *MP*, 52(9):572–577, September 2010.

[131] R. Pippan J. Zrnik, S. Scheriau. Structure and properties of aa6082. *XXXIV Verformungskundliches Kolloquium: ISBN 987-3-902078-20-9; pp. 193-197*, 2015.

[132] Hana Jirkova, Bohuslav Maajek, Ludmila Kuaerovaj, Ruth Treml, and Daniel Kiener. Influence of metastable retained austenite on macro and micromechanical properties of steel. *Journal of Alloys and Compounds*, 615(0):S163 – S168, 2014.

[133] J Klarner, B Buchmayr, and W Rainer. Toughtubes, extrem feinkoernige nahtlose stahlrohre. *BHM*, 156(5):168–174, 2011.

[134] M. Kopcewicz P. Pawluk, E. Skolek and W. Swiatnicki. The comparative study of phase composition of steels using x-ray diffraction and moessbauer spectroscopy. *Solid State Phenomena, Vols 203-204, pp. 150*, 2013.

[135] Stahl Eisen Werkstoffblatt. Din sew 090-2 high tenacity quenched and tempered fine grain steel part 2: Technical delivery conditions for tube and hollow sections, 1993.

[136] Gerald Winter, Juergen Klarner, Jozef Keckes, and Bruno Buchmayr. Multiscale and multi-method characterization of mechanical and microstructural. *XXXIV Verformungskundliches Kolloquium: ISBN 987-3-902078-20-9; pp. 203-209*, 2015.

[137] Gerald Winter, Mario Stefenelli, Juergen Klarner, Peter Staron, Torben Fischer, Jozef Keckes, and Bruno Buchmayr. Triaxial residual stresses in thermomechanically rolled seamless tubes characterized by high-energy synchrotron x-ray diffraction. *ASME PVP*, pages V003T03A020–V003T03A020, 2013.

E

Gradients of Mechanical Properties and Microstructure across Ultra-High-Strength Seamless Steel Tube Walls: The Influence of Thermo-Mechanical Treatment

Gerald Winter[a,c], Juergen Klarner[a], Jozef Keckes[b] and Bruno Buchmayr[c]

[a]voestalpine Tubulars GmbH & Co KG, Department R&D, Kindberg, Austria

[b]Department Materials Physics, University of Leoben, Austria

[c]Department Product Engineering, Chair of Metal Forming, University of Leoben, Austria

Abstract

Thermo-mechanical rolling of high-strength seamless steel tubes is routinely used to improve their mechanical properties. The treatment results in the formation of non-homogeneous distributions of phases, microstructure and residual stresses which influence the overall mechanical response of tubes decisively. In this contribution, microstructural and mechanical properties of air-cooled and intensive water spray-cooled low alloyed seamless steel tubes are analyzed across 10 mm tube wall cross sections. The aim is to reveal the correlation between heat treatment conditions, gradient microstructure and local tensile behaviour as well as Charpy impact response by analyzing miniaturized specimens machined from distinct tube wall regions. The results document that local mechanical properties vary significantly across the tube walls and can be correlated with the occurrence of gradient bainitic and bainitic-martensite microstructures. The intensive cooling increased the ultimate tensile strength from 1150 to 1450 MPa and a Charpy absorbed energy from

0.8 to 2.5 J (at -40 °C) in the outer tube region whereas the properties of the inner tube region were only marginally influenced. Finally, the local characterization allowed to quantify the role of spray water cooling on the gradient tube functional properties.

E.1. Introduction

Seamless steel tubes (SSTs) used in the automotive industry, structural applications or as drill pipes have to fulfil a variety of functional requirements like fatigue resistance, mechanical and chemical durability. The increasing demand for the production of light weight, high-strength and tough tubes requires an optimization of steel chemical composition as well as material microstructure. The production of SSTs includes a series of sub-processes like billet heating, piercing, push bench processing, reheating, stretch reducing and spray water cooling [142]. Thermo-mechanically treated SSTs exhibit usually ultra-high strength and excellent toughness which are primarily based on fine-grained material microstructure achieved by the advanced cooling technology [143]. In this way, overall mechanical behaviour of the tubes can be effectively influenced whereby the portion of alloying elements and productions costs can be reduced. Since the intensive water cooling during the last production step is applied on a outer tube side, very pronounced temperature gradients across the tube wall result in the formation of gradients of phases, microstructure and residual stresses [140]. As a consequence, those gradients are responsible for the variation of mechanical properties like hardness, ultimate tensile strength and toughness across the tube wall, as discussed in our previous works [146, 145]. Since steel exhibits a reduction of toughness with decreasing temperature due to ductile-brittle transition [141], the successful application of SSTs requires to evaluate how mechanical properties will change in low-temperature environments. For this purpose, usually Charpy impact tests, especially due to the simple nature of the technique, are still widely used to evaluate absorbed energy [138, 139]. In the present study, primarily impact properties of two ultra-high strength thermo-mechanically rolled SSTs produced from low-alloyed fine-grained steel are analyzed at room temperature (RT) and at -40 °C. The two tubes differ in the intensity of the spray water cooling. The toughness results are correlated with microstructure and hardness gradients as well as with varying tube tensile behaviour which originate from the dedicated thermo-mechanical treatment.

E.2. Experiment

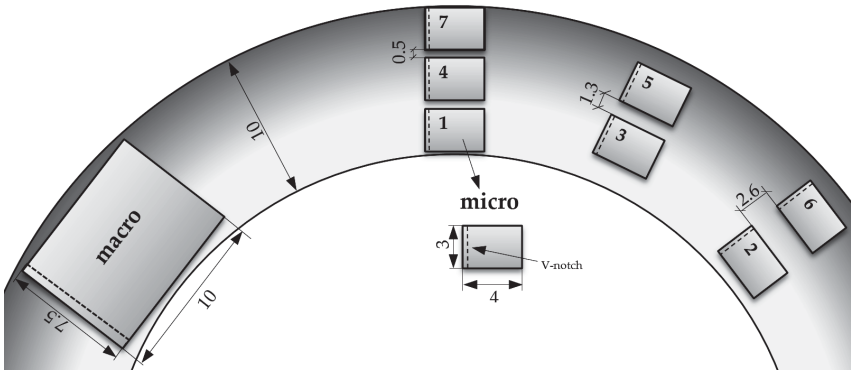

Figure E.1.: A schematic description of sample positions with dimensions at which macro and seven micro samples with lengths of 55 and 27 mm, respectively, were prepared for Charpy impact tests on TA and TB.

Low alloyed steel tubes with the wall thickness of 10 mm investigated in this work consisted of Fe alloyed with C, Mn, P, S, Cr, Ni and Ti of 0.2, 1.2, 0.01, 0.005, 1.0, 1 and 0.2 weight percent, respectively. For the two SSTs denoted further as TA and TB cooling rates of 5 (free air) and 30 °C/s (very intensive water spray cooling) were applied at the tube outer wall, respectively. Light microscopy was used to evaluate the microstructure of the tubes across the wall cross sections applying Olympus Lext OLS 4100 microscope. Before the analysis, the surfaces were chemically prepared using picrinic acid. Laboratory X-ray diffraction (XRD) analysis was used to evaluate phase and microstructure gradients using a 5 - circle X-ray diffractometer Smart Lab from Rigaku Co. equipped with Cu Kα radiation, a parabolic multilayer mirror in the primary beam and a secondary graphite monochromator. For the position-resolved analysis, a line beam profile with a size of 0.8 x 5 mm^2 was used whereby the tubes were scanned across the wall applying a sample movement step of 0.8 mm. Charpy impact tests were performed using a commercial device (Zwick RKP 450Z and Otto Wolpert - Werke PW 5 (50 J pendulum, 15 J hammer)) in the temperature range from -60 to 25 °C. The tests were carried out on macro and micro-samples, machined at different positions across the tube wall cross-sections according to the scheme in Fig. E.1.

Complementary Vickers hardness HV 0.5 tests across the tube cross-sections were performed using Buehler Micromet 5104 system. Miniaturized tensile tests on tube samples as a whole as well as on miniaturized tensile samples of about 0.8 mm in

thickness machined from different positions across tube walls were performed using Zwick BPC - F1200 HN.F11 system and using Kammrath & Weiss system in strain-controlled modes.

E.3. Results and Discussion

E.3.1. Optical microscopy

Optical micrographs of tubes TA and TB representative cross-sections are presented in Figs. E.2 and E.3. The images document a relatively uniform microstructure across TA and very gradual microstructure across TB tube walls. In the moderately cooled tube TA (Fig. E.2), the fine-grained microstructure is ferritic with traces of bainite. In TB tube (Fig. E.3), the intensive cooling resulted in the formation of very fine-grained bainitic microstructure, especially on the inner wall side, and of bainitic-martensitic microstructure at the outer tube wall side.

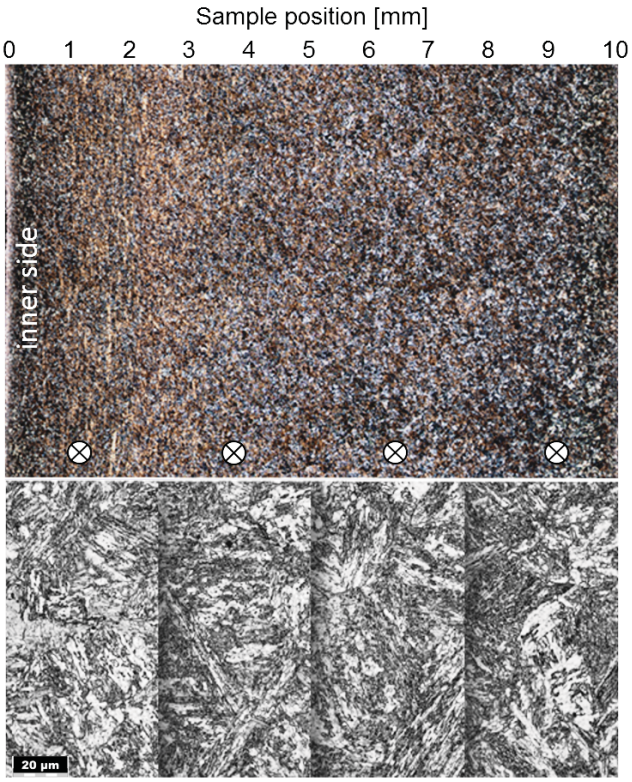

Figure E.2.: Optical images, overview (top) and four details taken at the position of the four circles (bottom), document a relatively homogeneous ferritic microstructure with traces of bainite across the TA tube wall cross-section.

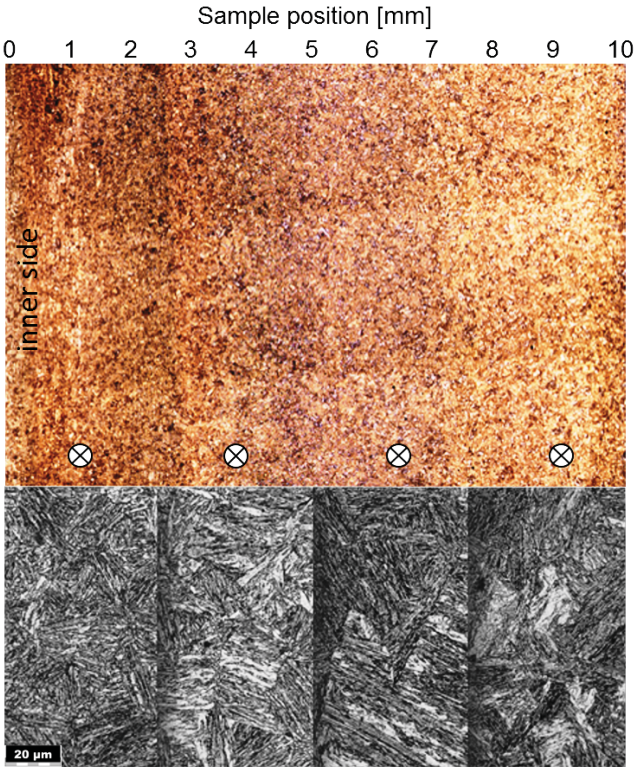

Figure E.3.: Optical images, overview (top) and four details taken at the position of the four circles (bottom), document a gradual microstructure across the TB tube wall cross-section. The detail images document that the intensive cooling of the tube inner side resulted in the formation of very fine bainitic microstructure which turns into bainitic-martensitic microstructure towards the outer tube wall side.

E.3.2. X-ray Diffraction Analysis

Results from the position-resolved XRD analysis on TA are presented in Fig. E.4. The results indicate that the tube consists mainly of ferrite (α - Fe phase) and there was a small portion of austenite (γ - Fe phase), less than 5 %. Interestingly, a comparison of the results from TA and TB did not indicate any significant differences in phase composition between the two tubes. A detailed analysis of the α-Fe 110 reflection intensity (Fig. E.5a) documented that the intensity remains constant across the whole TA cross-section whereas in TB there was significantly weaker intensity observed especially in TB tube center (Fig. E.5b). Since full width at half

maxima (FWHM) of α - Fe 110 reflections remained unchanged across the cross-sections of both tubes, it is supposed that the intensity variation can be attributed to crystallographic texture variation.

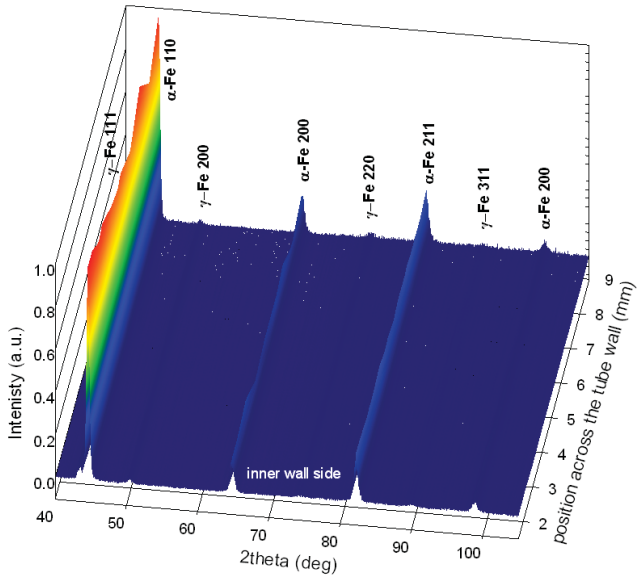

Figure E.4.: Representative XRD data collected with a step of 0.8 mm across the TA tube wall document the presence of ferrite (α - Fe phase) and a small portion of austenite (γ - Fe phase), with less than 5 %.

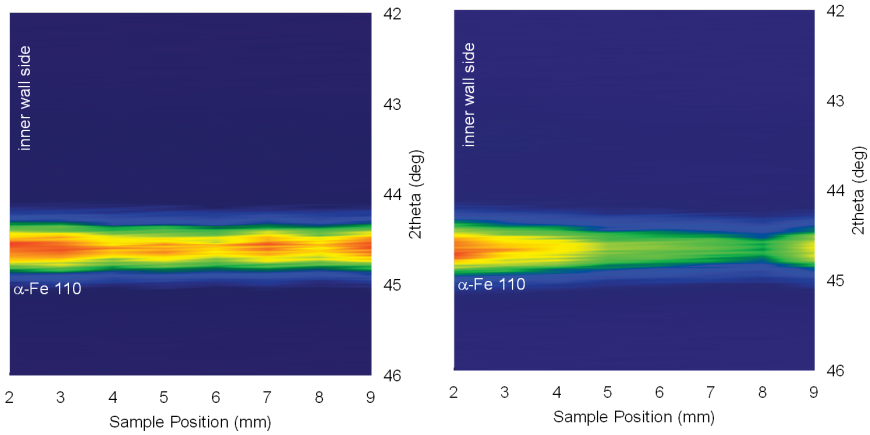

(a) TA **(b)** TB

Figure E.5.: XRD data collected with a step of 0.8 mm across TA and TB tube walls document the intensity development of α - Fe 110 reflections at the cross-sections.

E.3.3. Hardness Characterization

Results from hardness (HV 0.5) measurements across differently treated tube walls of TA to TB are presented in Fig. E.6. The hardness of tube TA is relatively small in the range of ∽ 386 - 413 HV 0.5 The intensively cooled tube TB shows a higher hardness in the range of ∽ 420 - 437 HV 0.5. The hardness level is relatively homogeneous for both tubes and does not reflect the microstructural gradients from Figs. E.2, E.3.

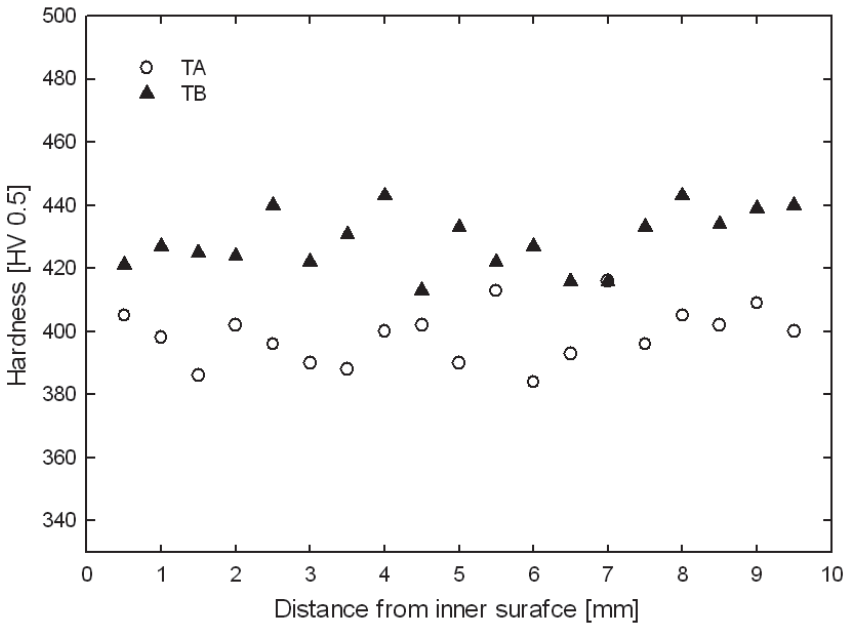

Figure E.6.: Micro-hardness distribution from inner to outer side of the wall indicates the influence of the varying cooling intensity on the local mechanical properties of TA and TB.

E.3.4. Tensile Response

Results from tensile tests from micro-samples of 0.8 mm in the thickness machined from different regions across TA and TB tube walls are presented in Fig. E.7. The results document that the microstructural gradients observed in Figs. E.2, E.3 result in the gradual stress-strain response of tube individual regions. In the moderately

cooled tube TA, a region with the smallest ultimate tensile strength (UTS) is interestingly the outer tube wall. This effect can be interpreted by the presence of tensile residual stresses up to 150 MPa reported in our previous study [144]. Since the outer region of tube TB experienced the most intensive spray water cooling, the highest UTS of ∽ 1450 MPa was observed (Figs. E.7, E.5a and E.5b), in agreement with the hardness data from Fig. E.6. A detailed analysis of the stress-strain responses and UTSs from TB individual regions (Fig. E.7) indicates that three tube outer regions exhibit highest yield stresses. This can be interpreted by the very intensive cooling as well as by a secondary structural recovery after the cooling, which was caused by the outer wall temperature increase caused by the heat stored in the tube inner region.

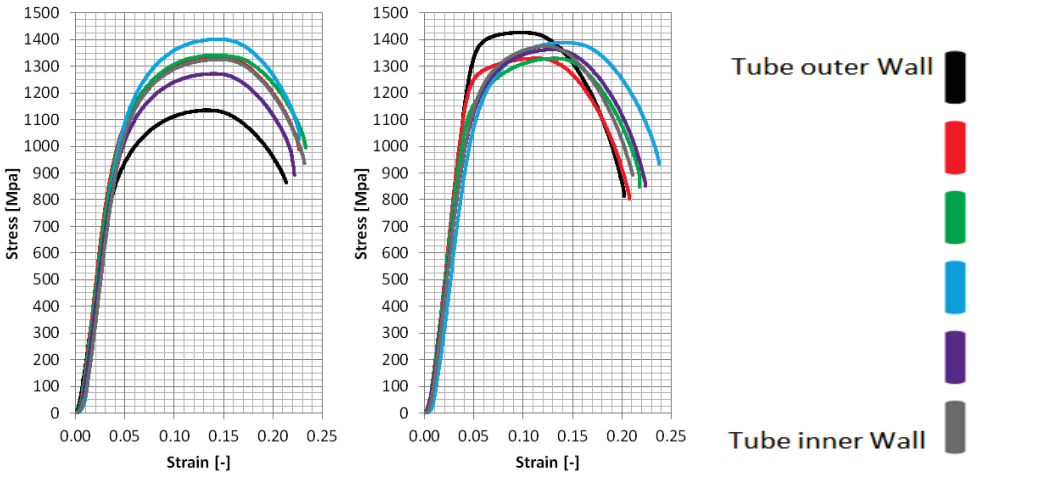

(a) TA **(b)** TB **(c)** Position resolved colour scale

Figure E.7.: Results from tensile tests on miniaturized specimens document the variation of mechanical properties across the walls of TA and TB tubes. UTS of the outer regions increased from 1150 to 1450 MPa after the intensive water spray cooling.

E.3.5. Macroscopic Charpy Tests

Charpy tests on macroscopic samples (Fig. E.1) were performed in the temperature range from -60 to 25 °C in order to elaborate the influence of low-temperature environment on the overall tube impact properties.

The results in Fig. E.8 document the thermo-mechanical treatment resulted in the increase of the absorbed energy from 32 to 62 J. The absorbed energy decreases as function of the decreasing temperature for both tubes and the dependencies converge at $\backsim$ 60 °C. For TB, the changes in the absorbed energy are significantly larger compared to those in TA. The abrupt changes especially between 25 and -10 °C could be attributed to a brittle-ductile transition of the bainitic steel which was completed at about -20 °C.

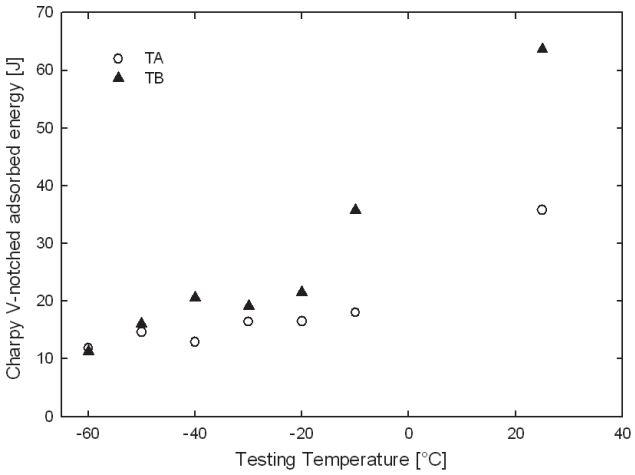

Figure E.8.: Results from Charpy V - notch tests on TA and TB macro samples document the development of the absorber fracture energy as a function of the testing temperature. The intensive water spray cooling caused a significant increase in the fracture resistance especially at RT.

In Fig. E.9 fracture surfaces of TA and TB tubes after Charpy V - notch tests at RT and -40 °C are presented. The appearance of the fracture surfaces gives information about the type of fracture that took place. TA and TB show predominantly a brittle fracture with typical bright and crystalline fracture surfaces. At the surfaces borders, jagged edges or shear lips which indicate a ductile behaviour, much more pronounced in TB tested at RT because of the large portion of dull and fibrous surface visible in Fig. E.9. This observation corresponds well with the increase in the absorbed energy (Fig. E.6) as well as with the higher tensile strength in Fig. E.7 from TB outer region. In both TA and TB, the tests at RT showed that the sizes of shear lips surfaces are larger on the outer side compared to the inner one. This effect documents that the free air as well as the intensive water spray cooling resulted in the increase of the fracture resistance of the outer tube wall side.

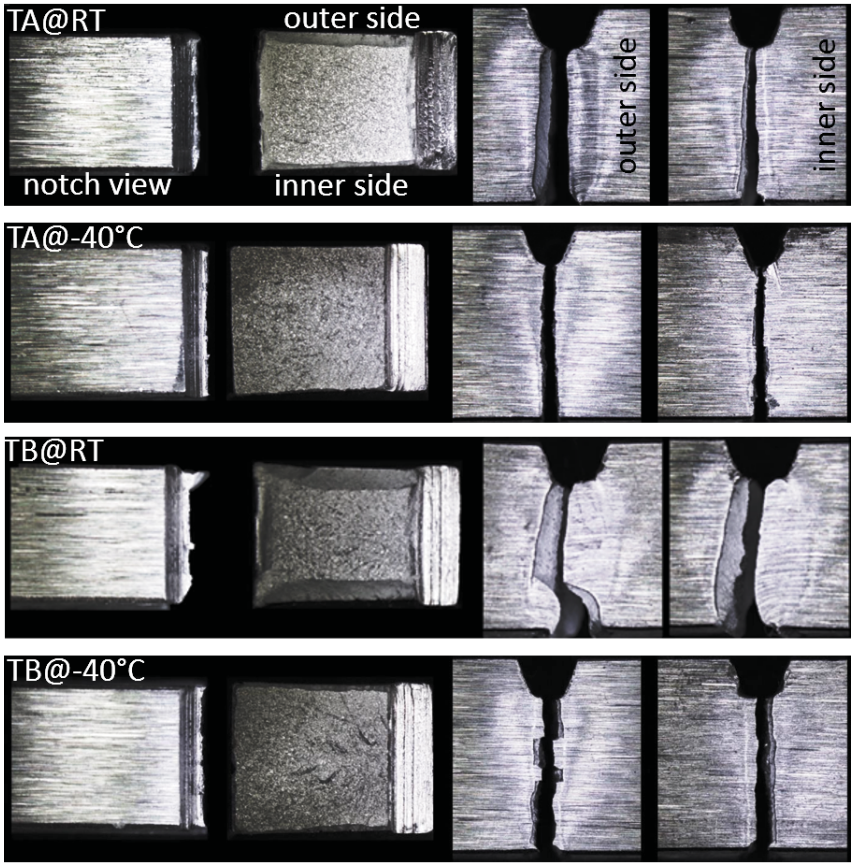

Figure E.9.: Fracture surfaces after Charpy V - notch tests of TA and TB macro samples at RT and -40 °C.

E.3.6. Microscopic Charpy Tests

Charpy tests on microscopic samples (Fig. E.1) were performed at -40 °C in order to evaluate the influence of a low-temperature environment as well as the gradient microstructure on the tube position-dependent impact properties. Though the absorbed energy obtained from impact tests on macro samples (Fig. E.9) was ∽ 12 and 21 J in TA and TB, the results from outer tube wall sides in Fig. E.10 indicate a significantly larger increase from 0.9 to 2.6 J. A similar increase was also observed for the sample positions 5 and 6 (Fig. E.10) and documents that the intensive cooling modified the Charpy impact response very effectively in about one third of the tube wall cross-section. The increase in the absorbed energy correlates well also with the increase of the yield stresses visible in Fig. E.7.

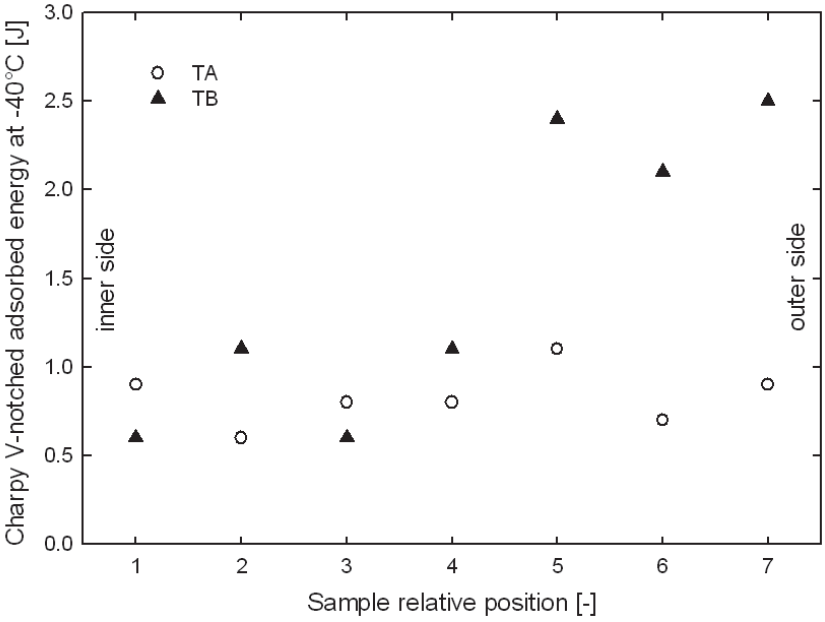

Figure E.10.: Results from Charpy V - notch tests on TA and TB micro samples performed at -40 °C document the development of the absorber fracture energy as a function of the sample position at the tube cross-section (cf. Fig. E.1) whereby positions 1 and 7 indicate inner and outer tube wall side. The intensive water cooling modified the impact behavior of the regions 5 - 7 significantly.

In Fig. E.11, fracture surfaces of micro samples after Charpy V - notch tests at -40 °C are presented.

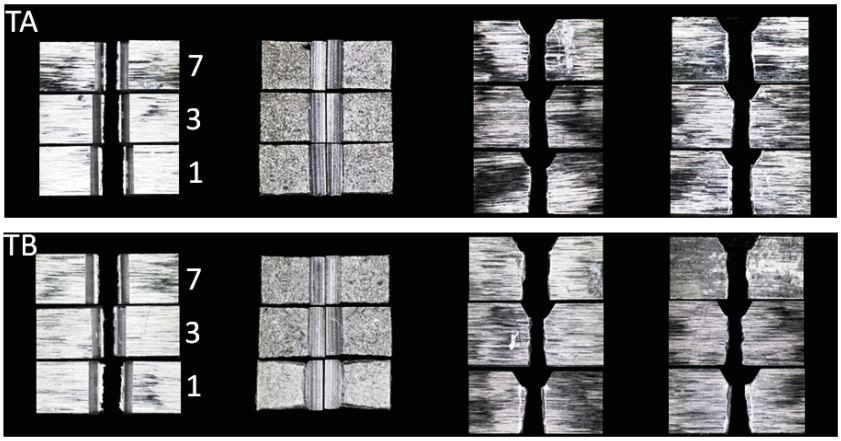

Figure E.11.: Fracture surfaces after from Charpy V - notch tests on micro samples performed at -40 °C.

The results document that the fractures surfaces from the tube TB exhibit the presence of shear lips which are most pronounced for the sample 1. The size of the lips gradually decreased towards the tube outer wall side. In the case of the samples produced from the tube TA, there are no signs of ductile behaviour with shear lips visible.

E.4. Conclusions

The combination of Charpy tests on macro and micro samples, tensile tests on miniaturized specimens and hardness characterization allowed to evaluate the influence of water spray cooling on the gradient mechanical properties of seamless steel tubes. The results document that the intensive cooling resulted in the improvement of hardness, impact resistance, UTS and yield stresses. The mechanical properties change gradually across the tube wall as a result of temperature gradients. Most pronounced influence of the cooling was observed in one third of the outer tube wall region. The mechanical data correspond well also with the gradual microstructure which was characterized using optical microscopy and XRD.

E.5. Acknowledgement

Financial support by the Austrian Federal Government (in particular from the Bundesministerium für Verkehr, Innovation und Technologie and the Bundesministerium für Wirtschaft, Familie und Jugend) and the Styrian Provincial Government represented by Österreichische Forschungsförderungsgesellschaft mbH and by Steirische Wirtschaftsförderungsgesellschaft mbH, is gratefully acknowledged. This project was supported by “Die Österreichische Forschungsförderungsgesellschaft” FFG Basisprogram and project “2655990 UHSTMRT”.

[138] Igor BARENYI, Ondrej HIRES, and Peter LIPTAK. Changes in mechanical properties of armoured uhsla steel armox 500 after over tempering. *Scientific Aspects of Armament and Saftey Technology*, pages 7–13, 2013.

[139] Emin Bayraktar, Dominique Kaplan, and Marc Grumbach. Application of impact tensile testing to spot welded sheets. *Journal of Materials Processing Technology*, 153(0):80 – 86, 2004. Proceedings of the International Conference in Advances in Materials and Processing Technologies.

[140] Wolfgang Bleck, Dietmar Haemberg, Ulrich Prahl, Piyada Suwanpinij, and Nataliya Togobytska. Optimal control of a cooling line for production of hot rolled dual phase steel. *steel research international*, 85(9):1328–1333, 2014.

[141] Marion Calcagnotto, Yoshitaka Adachi, Dirk Ponge, and Dierk Raabe. Deformation and fracture mechanisms in fine- and ultrafine-grained ferrite/martensite dual-phase steels and the effect of aging. *Acta Materialia*, 59(2):658–670, 2011.

[142] J Klarner, B Buchmayr, and W Rainer. Toughtubes, extrem feinkoernige nahtlose stahlrohre. *BHM*, 156(5):168–174, 2011.

[143] R. Song, D. Ponge, D. Raabe, J.G. Speer, and D.K. Matlock. Overview of processing, microstructure and mechanical properties of ultrafine grained bcc steels. *Materials Science and Engineering: A*, 441(12):1–17, 2006.

[144] Gerald Winter, Juergen Klarner, Bruno Buchmayr, and Jozef Keckes. Macro- and microscopic properties of gradient ultra-high-strength seamless steel tubes produced by dedicated thermo-mechanical treatments. *IFHTSE*, 2015.

[145] Gerald Winter, Juergen Klarner, Jozef Keckes, and Bruno Buchmayr. Multi-scale and multi-method characterization of mechanical and microstructural. *XXXIV Verformungskundliches Kolloquium: ISBN 987-3-902078-20-9; pp. 203-209*, 2015.

[146] Gerald Winter, Mario Stefenelli, Juergen Klarner, Peter Staron, Torben Fischer, Jozef Keckes, and Bruno Buchmayr. Triaxial residual stresses in thermo-mechanically rolled seamless tubes characterized by high-energy synchrotron x-ray diffraction. *ASME PVP*, pages V003T03A020–V003T03A020, 2013.